

DIELECTRIC CONE FEED REFLECTOR ANTENNAS

A Thesis Submitted to  
the Faculty of Graduate Studies  
The University of Manitoba

In Partial Fulfillment  
of the Requirements for the Degree of  
Doctor of Philosophy

by  
Rajinder Kumar Chugh

October 1977

DIELECTRIC CONE FEED REFLECTOR ANTENNAS

BY

RAJINDER KUMAR CHUGH

A dissertation submitted to the Faculty of Graduate Studies of the University of Manitoba in partial fulfillment of the requirements of the degree of

DOCTOR OF PHILOSOPHY

© 1978

Permission has been granted to the LIBRARY OF THE UNIVERSITY OF MANITOBA to lend or sell copies of this dissertation, to the NATIONAL LIBRARY OF CANADA to microfilm this dissertation and to lend or sell copies of the film, and UNIVERSITY MICROFILMS to publish an abstract of this dissertation.

The author reserves other publication rights, and neither the dissertation nor extensive extracts from it may be printed or otherwise reproduced without the author's written permission.



TO MY PARENTS

AND

TO MY FAMILY

## ABSTRACT

The reflector antennas with a dielectric cone supported subreflector are gradually becoming popular for satellite communication. Present work describes an analytical design procedure, based on the principles of geometrical optics, for antennas employing dielectric cone feeds. This design can be used to obtain any arbitrary aperture amplitude and uniform phase distributions, as compared to the design developed by Salema (1972) which provided only uniform phase distribution in the aperture plane. The procedure presented in this thesis can be used for dual reflector antennas, reflector antennas with a dielectric cone supported subreflector and reflector antennas using dielectric cone feeds with a shaped reflecting surface of the cone material. Theoretically, any set of parameters can be used for the main reflector, the subreflector and the dielectric cone. However, it is analytically shown that the excitation efficiency of the dominant mode in the dielectric cone decreases with an increase in the dielectric constant of the cone material. On the other hand, the reflection loss at the cone surface increases with the dielectric constant and results in a reduction of the overall system efficiency. Therefore, for highly efficient systems a choice of low relative permittivity for the cone material is recommended.

The shaped dual reflector system with a dielectric cone of low relative permittivity has been shown to have better theoretical performance than the shaped dual reflector system without a dielectric cone. However, an experimental investigation of these theoretical results is recommended.

## ACKNOWLEDGEMENTS

It seems unfair to single out a few individuals for mentioning when many have contributed directly and indirectly to the preparation of this manuscript. Yet, it would be inexcusable to overlook those who have helped most during the work on this thesis. Special thanks are due to Dr. L. Shafai for his guidance, constant encouragement and patience during the research and writing of this dissertation.

Thanks are also due to Dr. W. M. Boerner for helping me in every possible way at certain stages. Particular appreciation must be expressed for the critical discussions with Dr. T. C. K. Rao, Dr. O. Aboul-Atta and the help from the staff as well as the graduate students of the Department of Electrical Engineering. Thanks are also due to Mrs. Shirley Clubine for an excellent typing job.

The financial support by the National Research Council of Canada and the University of Manitoba is deeply appreciated.

## TABLE OF CONTENTS

		PAGE
ABSTRACT		i
ACKNOWLEDGEMENTS		ii
TABLE OF CONTENTS		iii
LIST OF FIGURES		vi
LIST OF TABLES		x
LIST OF SYMBOLS		xi
CHAPTER I	INTRODUCTION	1
CHAPTER II	REFLECTOR ANTENNAS	12
	2.1 INTRODUCTION	13
	2.2 CLASSICAL DUAL REFLECTOR SYSTEMS	17
	2.2.1 Types of Classical Systems	17
	2.2.2 Aperture Blockage in Cassegrain Antenna	20
	2.3 SHAPED DUAL REFLECTOR SYSTEMS	33
	2.4 SUMMARY AND DISCUSSION	35
CHAPTER III	FEEDS FOR REFLECTOR ANTENNAS	39
	3.1 INTRODUCTION	40
	3.2 CONICAL HORN ANTENNA	42
	3.2.1 Characteristic Equation and Aperture Fields	43
	3.2.2 Theoretical and Experimental Radiation Patterns	51
	3.3 DIELECTRIC CONE ANTENNA	56
	3.3.1 Characteristic Equation for a Dielectric Cone Antenna	59
	3.3.2 Aperture Field Distribution	68
	3.3.3 Mode Excitation Efficiencies	72
	3.3.4 Theoretical and Experimental Radiation Patterns	82
	3.4 SUMMARY AND DISCUSSION	90

	Page
CHAPTER IV	ANTENNAS WITH MODIFIED DIELECTRIC CONE FEED 91
4.1	INTRODUCTION 92
4.2	DESIGN OF THE SHAPED REFLECTING SURFACE 94
4.3	ANALYSIS OF CONICAL REFLECTOR WITH MODIFIED DIELECTRIC CONE FEED 102
4.3.1	Aperture Field Distribution for a Conical Reflector 105
4.3.2	Theoretical Radiation Patterns of a Conical Reflector with Modified Dielectric Cone Feed 114
4.4	SUMMARY AND DISCUSSION 127
CHAPTER V	DESIGN OF DIELECTRIC CONE FEED ANTENNAS FOR ARBITRARY APERTURE DISTRIBUTION 129
5.1	INTRODUCTION 130
5.2	DESIGN PROCEDURE 131
5.2.1	General Considerations 131
5.2.2	Formulation of Differential Equations 134
5.2.3	Choice of System Parameters 143
5.2.4	Solution of Differential Equations 145
5.3	CONE EDGE REFLECTION LOSS CALCULATION 152
5.4	COMPARISON OF THE DIELECTRIC CONE FEED ANTENNAS AND THE SHAPED CASSEGRAIN ANTENNAS 156
5.5	SUMMARY AND CONCLUSIONS 159
CHAPTER VI	CONCLUSIONS 161
6.1	SUMMARY OF THE RESULTS 162
6.2	SUGGESTIONS FOR FURTHER WORK 163

		Page
APPENDIX A	GAIN AND BLOCKAGE EFFICIENCY IN DUAL REFLECTOR SYSTEMS	164
APPENDIX B	REFLECTION COEFFICIENTS FOR THE INCIDENT FIELDS FROM THE DIELECTRIC CONE APERTURE PLANE	172
REFERENCES		180

## LIST OF FIGURES

	<u>PAGE</u>
Fig. 1.1 External noise sources in an antenna system	3
Fig. 1.2 Front-fed parabolic reflector antenna	5
Fig. 1.3 Classical Cassegrain antenna	6
Fig. 1.4 Off-set reflector antenna systems	8
Fig. 1.5 Dielectric cone feed reflector antenna	9
Fig. 2.1 Classical Gregorian antenna	19
Fig. 2.2 Complex $IFR_E$ and $IFR_H$ for a circular cylinder	23
Fig. 2.3 Optical shadowing by plane and spherical waves in the Cassegrain antenna system with four struts	25
Fig. 2.4 Variation of blockage efficiencies in the Cassegrain antenna with subreflector diameter for $D = 48\lambda$ , $W = 1.5\lambda$ and $r_0 = 20\lambda$	28
Fig. 2.5 Variation of blockage efficiencies in the Cassegrain antenna with the width of the supporting structure for $D = 48\lambda$ , $D_s = 8\lambda$ and $r_0 = 20\lambda$	29
Fig. 2.6 Variation of blockage efficiencies in the Cassegrain antenna with support point movement for $D = 48\lambda$ , $D_s = 8\lambda$ and $W = 1.5\lambda$	30
Fig. 2.7 Variation of blockage efficiencies in the Cassegrain antenna with the edge illumination of the main reflector for $D = 48\lambda$ , $D_s = 8\lambda$ , $r_0 = 20\lambda$ and $W = 1.5\lambda$	31
Fig. 3.1 Coordinate system for the conical horn antenna analysis	44
Fig. 3.2 Roots of the characteristic equations of a conical horn for $m = 0$	48
Fig. 3.3 Roots of the characteristic equations of a conical horn for $m = 1$	49
Fig. 3.4 E-plane aperture amplitude distributions for various modes in a conical horn antenna with $\theta_e = 9.5^\circ$	52
Fig. 3.5 H-plane aperture amplitude distributions for various modes in a conical horn antenna with $\theta_e = 9.5^\circ$	53

<u>List of Figures</u> Cont.	<u>Page</u>
Fig. 3.6 Measured and theoretical radiation patterns of a conical horn at 8.5 GHz. $\theta_e = 9.5^\circ$ , $ka = 35.0551$	57
Fig. 3.7 Measured and theoretical radiation patterns of a conical horn at 11 GHz. $\theta_e = 9.5^\circ$ , $ka = 45.3655$	58
Fig. 3.8 Coordinate system for the dielectric cone antenna	60
Fig. 3.9 Roots of the characteristic equation of the dielectric cone versus cone flare angle for $\epsilon_r = 1.1$	69
Fig. 3.10 Dominant roots of the characteristic equation of the dielectric cone versus cone flare angle for $\epsilon_r = 2.5$	70
Fig. 3.11 Theoretical E-plane aperture amplitude distributions for first five modes of a dielectric cone with $\theta_e = 9.5^\circ$ , $k_2 \ell = 97.2447$ , $\epsilon_r = 2.28$ and $m = 1$	73
Fig. 3.12 Theoretical H-plane aperture amplitude distributions for first five modes of a dielectric cone with $\theta_e = 9.5^\circ$ , $k_2 \ell = 97.2447$ , $\epsilon_r = 2.28$ and $m = 1$	74
Fig. 3.13 Variation of mode excitation efficiencies with relative permittivity of the cone material. $k_2 \ell = 100.0$ , $k_2 a = 35.0$ and $\theta_e = 10^\circ$	78
Fig. 3.14 Variation of mode excitation efficiencies with the cone length $k_2 \ell$ of the dielectric material for $k_2 a = 35.0$ and $\theta_e = 10^\circ$	79
Fig. 3.15 Variation of mode excitation efficiencies with conical horn length for $k_2 \ell = 100.0$ and $\theta_e = 10^\circ$	80
Fig. 3.16 Variation of mode excitation efficiencies with cone flare angle for $k_2 \ell = 100.0$ and $k_2 a = 40.0$	81
Fig. 3.17 Dimensions of the dielectric cone and the conical horn made for the experiment	85
Fig. 3.18 Measured and theoretical radiation patterns of a dielectric cone antenna at 8.5 GHz	86
Fig. 3.19 Measured E-plane radiation patterns of the dielectric cone with and without absorbing material at 8.5 GHz	87
Fig. 3.20 Measured radiation patterns of a dielectric cone antenna at 10.2 GHz	89

<u>List of Figures</u> Cont.	<u>Page</u>
Fig. 4.1 Dielectric cone feed reflector antenna	93
Fig. 4.2 Shaped surface geometry for the dielectric cone feed	95
Fig. 4.3 Variation of surface curvature with K	100
Fig. 4.4 Variation of surface curvature as a function of relative permittivity for $K = 1$	101
Fig. 4.5 Variation of surface curvature as a function of relative permittivity for $K = 0.002$	103
Fig. 4.6 Geometry of an antenna using dielectric cone feed with a shaped reflecting surface	108
Fig. 4.7 Theoretical E-plane aperture distributions as a function of cone flare angle $\theta_e$ for conical reflector antennas with a modified dielectric cone feed	115
Fig. 4.8 Theoretical H-plane aperture distributions as a function of cone flare angle $\theta_e$ for conical reflector antennas with a modified dielectric cone feed	116
Fig. 4.9 Theoretical E-plane aperture distributions as a function of relative permittivity for conical reflector antennas with modified dielectric cone feed for $\theta_e = 10^\circ$	117
Fig. 4.10 Theoretical H-plane aperture distributions as a function of relative permittivity for conical reflector antennas with modified dielectric cone feed for $\theta_e = 10^\circ$	118
Fig. 4.11 E-plane theoretical radiation patterns of conical reflector antennas with a modified dielectric cone feed as a function of cone flare angle $\theta_e$	122
Fig. 4.12 H-plane theoretical radiation patterns of conical reflector antennas with a modified dielectric cone feed as a function of cone flare angle $\theta_e$	123
Fig. 4.13 E-plane theoretical radiation patterns for conical reflector antennas with modified dielectric cone feed as a function of relative permittivity of the cone material	124

<u>List of Figures</u>	<u>Cont.</u>	<u>Page</u>
Fig. 4.14	H-plane theoretical radiation patterns for conical reflector antennas with modified dielectric cone feed as a function of relative permittivity of the cone material	125
Fig. 5.1	Geometry of antenna using dielectric cone feed	132
Fig. 5.2	Variation of surface curvatures for both reflectors as a function of relative permittivity of the cone material for $D = 48\lambda$ , $D_s = 8\lambda$ and $z_2 = 12\lambda$ .	149
Fig. 5.3	Variation of surface curvatures for both reflectors as a function of cone flare angle of the dielectric cone for $D = 48\lambda$ , $\epsilon_r = 2.0$ , $k_2 \ell = 144.374$ and $z_2 = 12\lambda$ .	150
Fig. 5.4	Variation of surface curvatures for both reflectors as a function of cone length of the dielectric cone	151
Fig. 5.5	Differential areas of the incident rays at the surface S and the cone edge	154
Fig. A.1	Support structure blockage in the Cassegrain antenna	168
Fig. B.1	Refraction and reflection of a plane wave from the aperture plane of the dielectric cone antenna	175

LIST OF TABLES

		<u>PAGE</u>
Table 4.1	Maximum and Minimum Permissible Values of Relative Permittivity	99
Table 4.2	Permissible Values of K for Cone Flare Angle = 5°	99
Table 5.1	Loss Calculation for the Dielectric Cone Feed Antenna	158
Table 5.2	Loss Calculation for the Shaped Cassegrain System	158

## LIST OF SYMBOLS

Unless otherwise stated, the symbols most commonly used in this thesis have the following meaning.

### Greek Alphabet:

$\alpha'$	polarization angle.
$\alpha''$	tilt angle of the strut.
$\beta$	angle of the reflected ray from the subreflector or the shaped surface.
$\gamma$	angle of the transmitted ray from the dielectric cone surface with the axis of symmetry.
$\Gamma$	voltage reflection coefficient.
$\delta_{\parallel}, \delta_{\perp}$	phase shifts due to the total internal reflection for the components parallel and perpendicular to the plane of incidence.
$\epsilon$	permittivity.
$\theta_c = \sin^{-1}(1.0/\sqrt{\epsilon_1})$	critical angle.
$\theta_e$	cone flare angle.
$\eta$	efficiency.
$\lambda$	wavelength.
$\mu$	permeability.
$(\rho, \phi, z)$	cylindrical coordinate system.
$\omega$	angular frequency.

### Latin Alphabet:

$\bar{A}$	magnetic vector potential.
$A_r$	component of magnetic vector potential along the r - direction.
$\bar{a}_x$	unit vector along the x - direction.
$\text{Cos}(\theta)$	cosine of angle $\theta$ .
D	main reflector diameter.

dB	decibel.
$D_s$	subreflector diameter.
$\vec{E}$	electric field vector.
e	base of natural logarithms.
$\vec{E}^*$	complex conjugate of the electric field vector.
$\vec{E}_s$	radiated electric field vector.
$\vec{F}$	electric vector potential.
$F(x,y), F(\rho,\phi)$	aperture field distribution.
f	focal length of the parabolic reflector.
$f_1, f_2$	foci of the subreflector.
$g(\theta', \phi')$	directive gain pattern of an aperture at observation angles $\theta'$ and $\phi'$ .
$\vec{H}$	magnetic field vector.
$H_m^{(2)}(x)$	Hankel function of second kind of order m and argument x.
$h_s(x)$	spherical Riccati - Hankel function of second kind of order s and argument x.
$IFR_E, IFR_H$	induced field ratios for the circular cylinder for $E_z$ and $H_z$ polarizations.
j	$\sqrt{-1}$
$J_m(x)$	Bessel function of order m and argument x.
K	constant for the shaped surface design.
$k = \frac{2\pi}{\lambda}$	propagation constant.
$K_m(x)$	modified Bessel function of second kind of order m and argument x.
$\ell$	path length of any ray.
$\vec{n}$	unit normal vector.
$P_v^m(\cos\theta)$	associated Legendre polynomial of first kind of order m and degree v.
$r_0$	distance of the supporting point for the supporting structure from the axis of symmetry.

$(r, \theta, \phi)$	spherical coordinate system.
$R_{11}, R_{\perp}$	reflection coefficients for the components parallel and perpendicular to the plane of incidence.
S	shaped dielectric surface or the metallic subreflector.
$\text{Sin}(\theta)$	sine of angle $\theta$ .
$T_{11}, T_{\perp}$	transmission coefficients for the components parallel and perpendicular to the plane of incidence.
W	width of the supporting structure.
$(x, y, z)$	rectangular coordinate system.

INTRODUCTION

CHAPTER I

An extensive amount of research has been devoted to focusing reflector antennas, particularly during the last quarter century. The main reason for this is the requirement of a system with high gain, low side lobe level and low cross-polarization component for point-to-point communication. In addition to these the need for low noise is also essential. Noise is introduced in the communication systems from the receiver itself, and additional contributions arise from a combination of man-made and sky noises (Fig.1.1).

The above mentioned system requirements can be met either by using phased arrays of the broad beam antennas or by using reflecting systems. The phased array is not universally useful because it is a complicated and costly system [Steinberg, 1976]. The reflecting system, on the other hand, is conceptually simple and is usually a relatively simple structure. It can be serviced mechanically with far less sophistication than is required for a phased array. As a single, monolithic unit on a mechanical scanning assembly, it is relatively inexpensive to scan. The phased array, on the other hand, requires a phase shifter for each element or at least for each subarray. Therefore, reflecting systems are the appropriate choice for most point-to-point communication systems unless the system is required to have certain particular characteristics, such as a wide and continuous scanning, where the phased array is a better choice.

In the reflecting systems, reflectors are mainly used to modify the radiation from a radiating element or feed. The reflectors in the reflecting systems can have a variety of contours like a parabola,

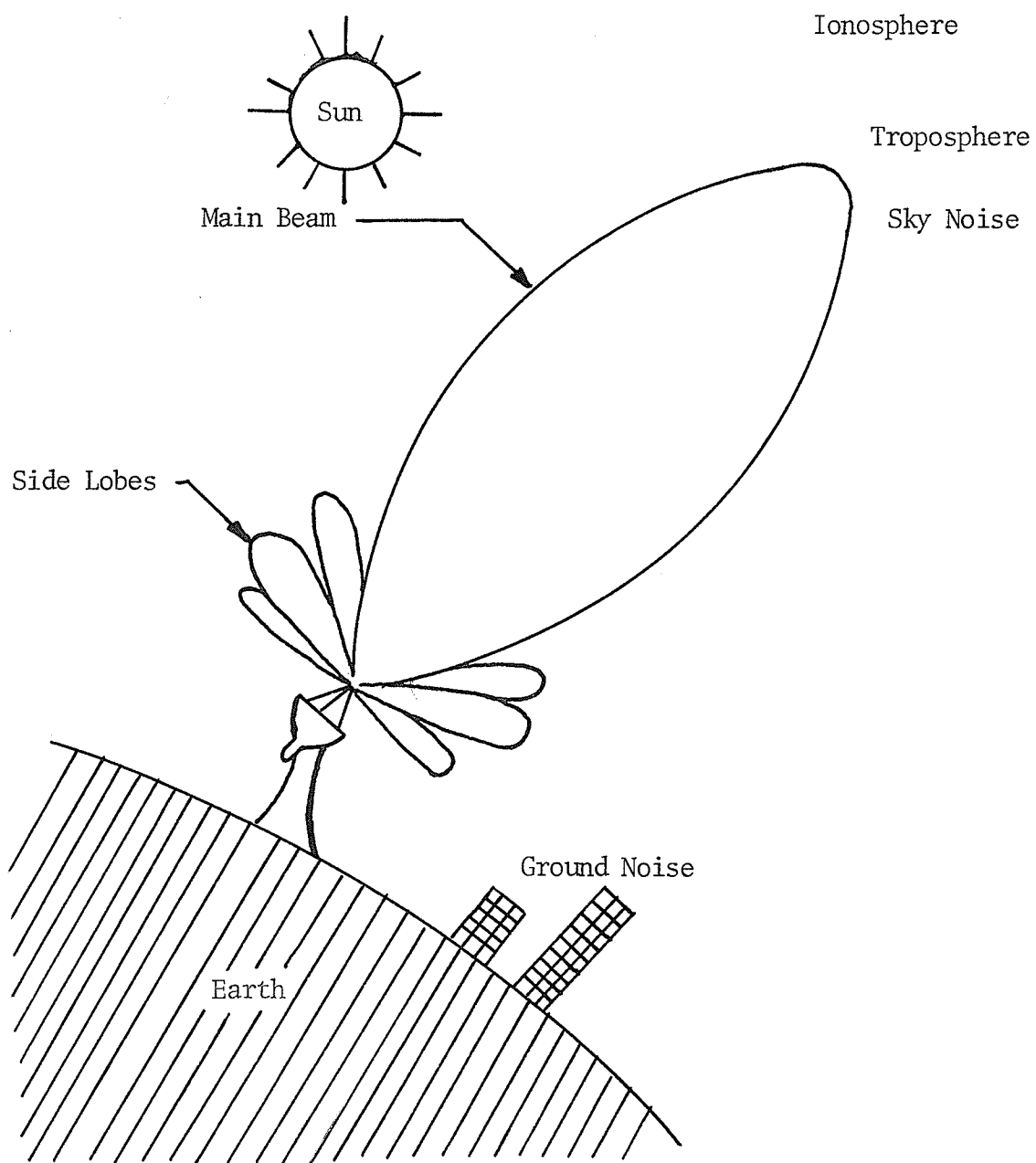


Fig. 1.1 External noise sources in an antenna system

circle, ellipse, etc. or can have the shaped contour designed for some specific purpose [Hansen, 1964]. The feeds for the reflecting systems can either be one of the broad beam antennas such as dipoles, slots, helices, loops, spirals, horns, etc. [Jasik, 1961; Wolff, 1966] or a feed consisting of one of these broad beam antennas along with one or more secondary reflectors [Hannan, 1961; Hansen, 1964; Visocekas, 1964; Clarricoats and Lim, 1969; Collin and Zucker, 1969; Phillips and Clarricoats, 1970].

The simplest reflecting system for generating a pencil beam has a parabolic reflector. This is the only reflector that has the property of giving a collimated beam from a point source located at the focus. Other types of reflectors that can also be used to generate pencil beams are spherical, stepped, polarized and lensed reflectors [Hansen, 1964]. However, these systems are more complex, usually for improving the scanning capability of the system. The front location of the feed and supporting structure (Fig. 1,2) in the single reflecting systems has the disadvantages of aperture blockage due to the feed, high noise temperature and the inconvenience of servicing the feed or the receiver in large systems.

In recent years, multi-reflector systems are becoming more common in use than ordinary single reflector systems due to high magnification with a short focal length, a convenient rear location of the feed or the receiver and the potential of higher efficiency through shaping. The most common among the multi-reflector systems is the system based on the Cassegrain telescope (Fig.1,3). This consists of a main parabolic reflector and a secondary hyperbolic subreflector. One of the foci of the subreflector coincides with the focus of the para-

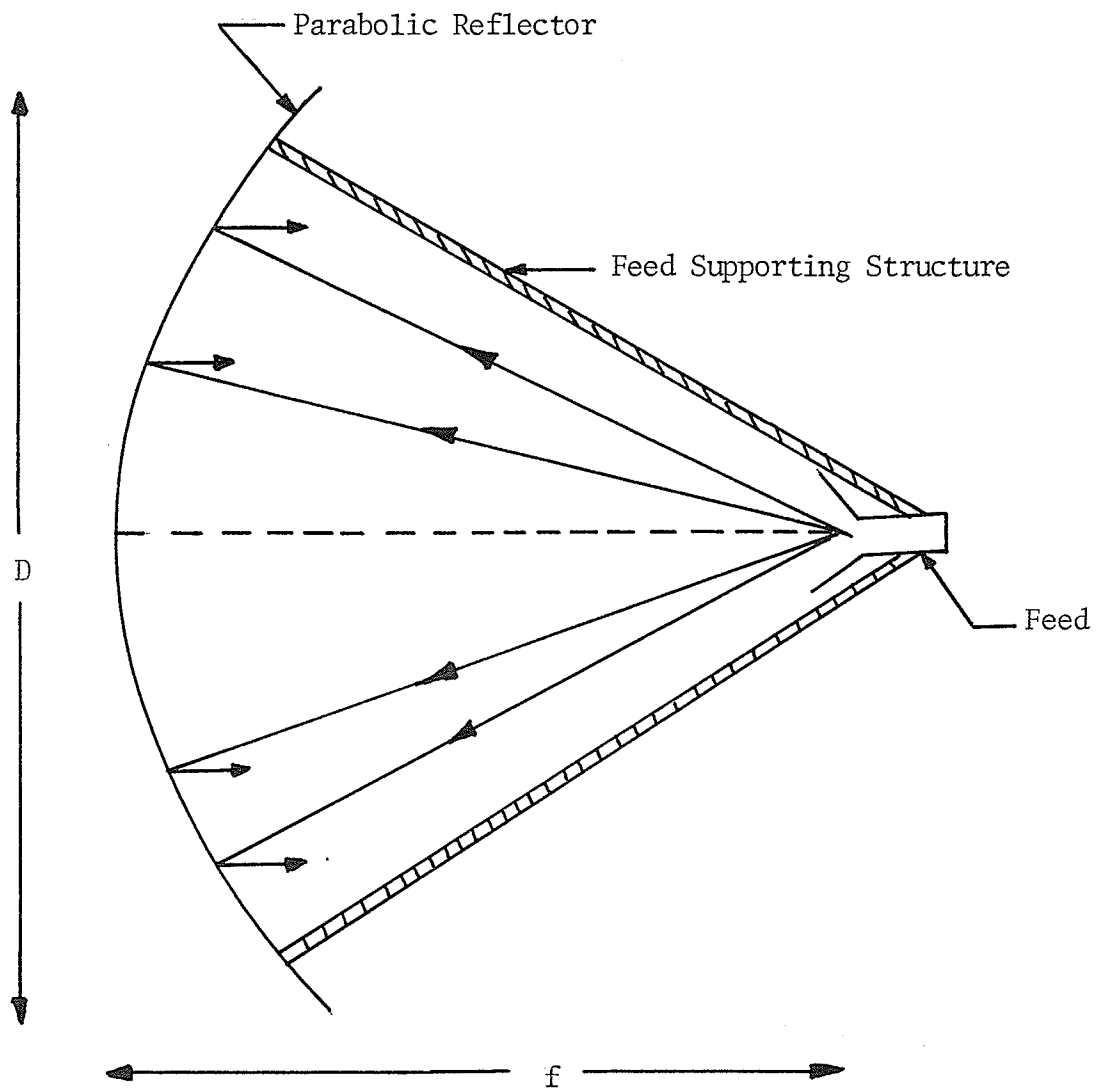


Fig. 1.2 Front-fed parabolic reflector antenna

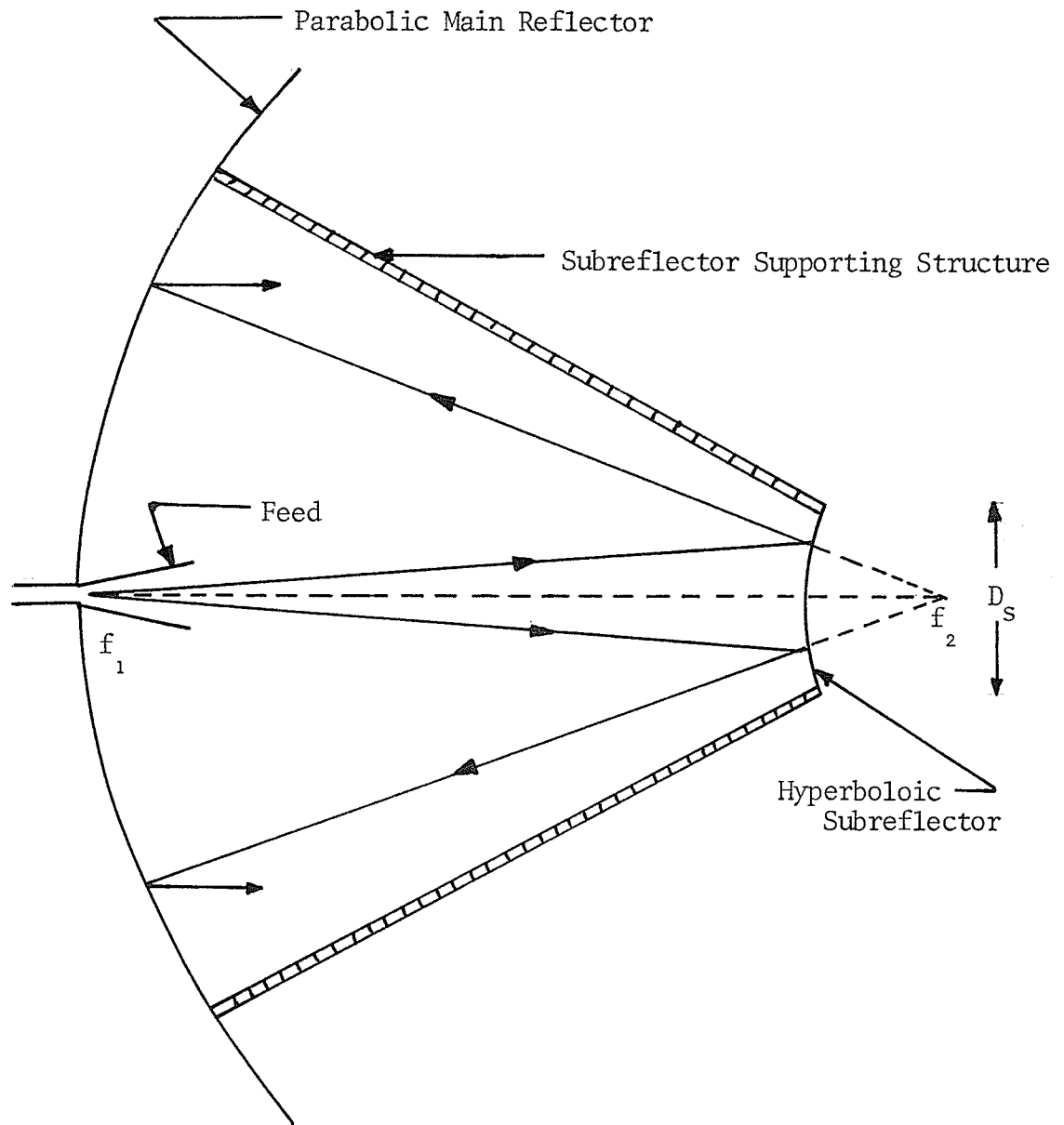
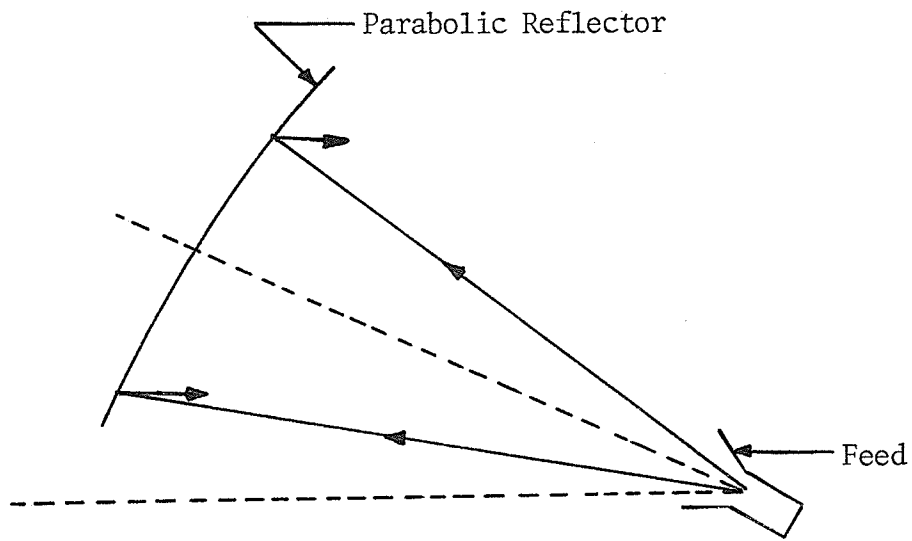


Fig. 1.3 Classical Cassegrain antenna

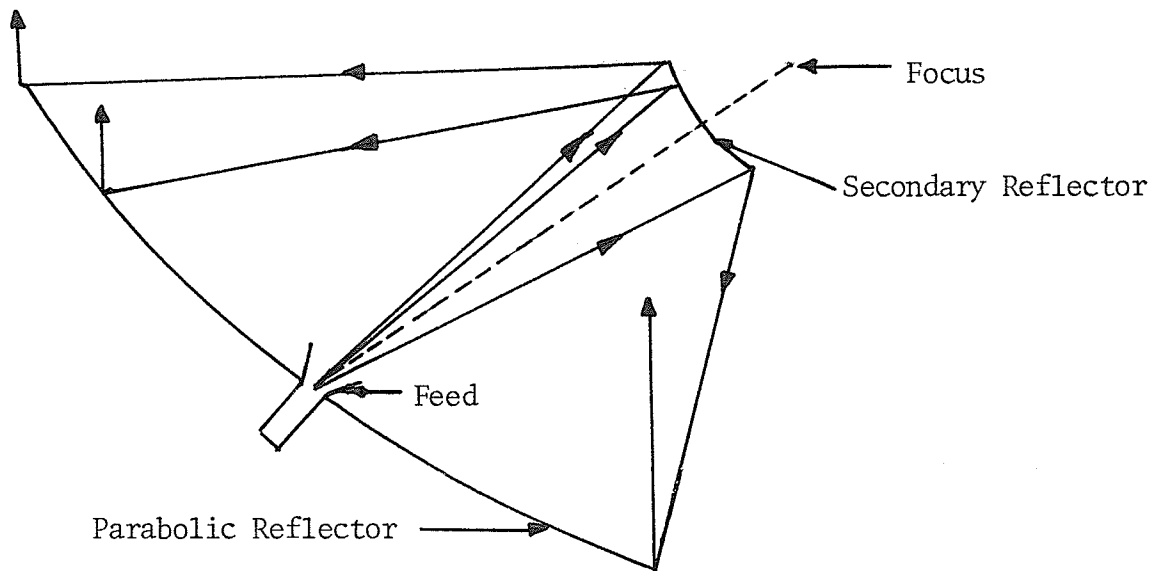
bolic reflector and the other focus is the point for the feed or the receiver. Some of the factors affecting the performance of the Cassegrain system in the microwave range of electromagnetic spectrum are the blocking of main aperture by subreflector as well as supporting structure, the diffraction from the supporting structure and reflector edges, spillover loss from the feed and a non-uniform aperture distribution.

The aperture efficiency and aperture blockage of the Cassegrain system depend upon the amplitude and phase distribution in the aperture plane [Silver, 1949; Sciambi, 1965]. Therefore, many attempts have been made to obtain an a priori distribution in the aperture plane from the known feed patterns [Galindo, 1964; Morgan, 1964; Williams, 1965; Wood, 1972; Collins, 1973]. Some of these design techniques take into consideration the influence of diffraction at the edges as well. The diffraction from the supporting structure has also been studied using simplified models [Rusch and Sørensen, 1974; Rusch et. al., 1976; Shafai et.al, 1977, Rusch et.al., 1977]. However, the exact analysis of the diffraction and its effect on gain, side lobe level and depolarization is still too complex to handle with the present day knowledge.

The alternative solution to the supporting structure problem is to use a system without supporting arms in the main beam path. The two possible alternatives to the ordinary Cassegrain system are the offset systems (Fig.1.4) and the use of dielectric cone to support the subreflector (Fig.1.5). During recent years, the offset systems or open systems are being studied in great detail to evaluate their advantages and disadvantages [Cook et.al., 1965; Chu and Turrin, 1973; Maanders, 1975]. However,



(a) Off-set parabolic reflector antenna



(b) Off-set Cassegrain antenna

Fig. 1.4 Off-set reflector antenna systems

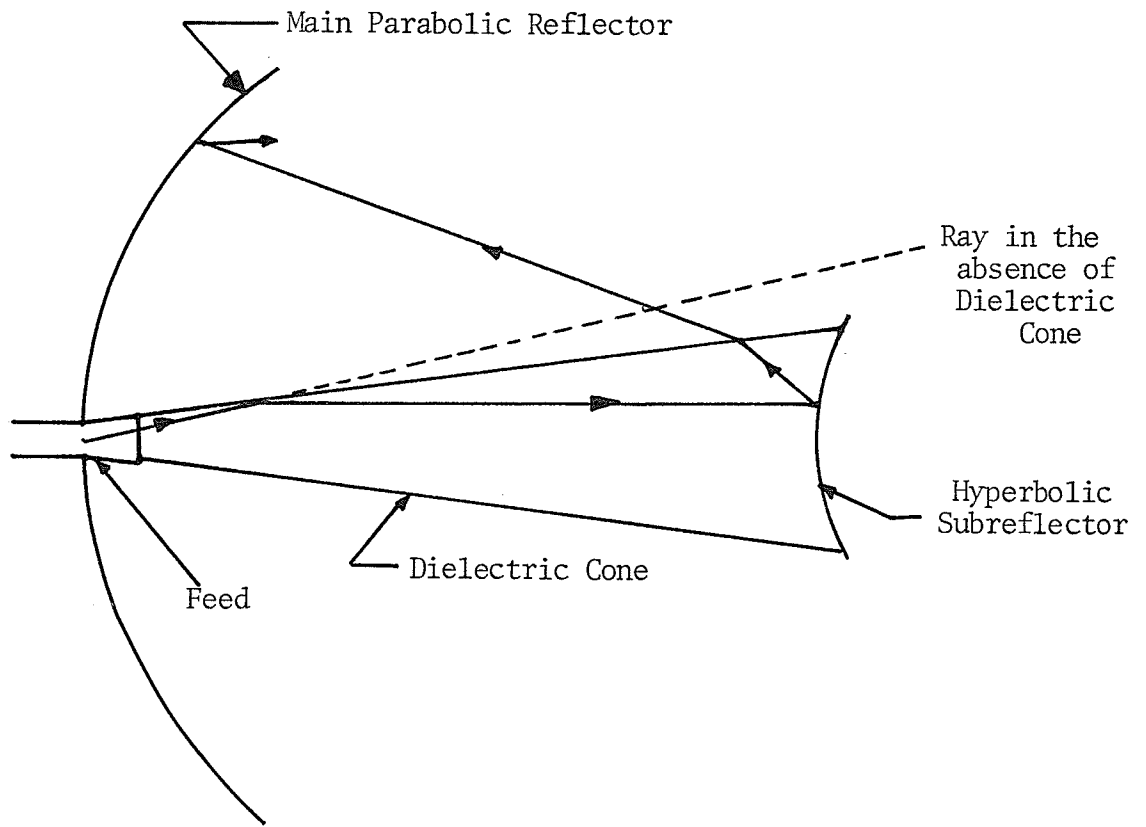


Fig. 1.5 Dielectric cone feed reflector antenna

there is not much work available [ Salema, 1972; Clarricoats and Salema, 1973 ] on the performance of the "dielectric guides" or the Cassegrain system using dielectric cone to support the subreflector.

The reflector antennas with a dielectric cone supported subreflector are gradually becoming popular for satellite communication [ Petrick and Abrahamson, 1974; Ince et al., 1974; Buchmeyer, 1977 ]. The present study involves the design and analysis of the reflector antennas with dielectric cone feeds.

The main contribution of the present work is the design of the two-reflector system with a dielectric cone for any arbitrary aperture amplitude and uniform phase distributions from a given power pattern of the incident field at the dielectric cone aperture. This design, based on the principles of geometrical optics, is also extended to include a main reflector fed by a dielectric cone with a shaped dielectric reflecting surface instead of a metallic subreflector. The design is general enough to handle any value of dielectric constant for the cone material and any set of parameters for the cone angle, main reflector diameter and subreflector diameter. However, an arbitrary aperture amplitude and uniform phase distributions can be usefully obtained only when the subreflector is metallized.

The power pattern of the incident field at the subreflector can be determined by the approximate solution [ Salema, 1972 ] for the modes in the dielectric cone. Although some of the assumptions in that work seem difficult to justify theoretically, Salema has indicated a good comparison with the experimental work. This procedure for determining the mode representation in the dielectric cone is utilized to obtain the surface shapes

for the various cases in Chapters IV and V. However, it should be noted that the design is not restricted in any way to this particular mode representation in the dielectric cone.

For a comparison of the performance of the designed system with the Cassegrain system, the second chapter presents a brief description of different microwave reflector antennas followed by an analysis of the blockage in the Cassegrain antenna. The power pattern of the feed fields using conical horns with and without dielectric cone can be determined from the analysis presented in Chapter III. The power patterns of the conical horn with a dielectric cone are utilized in Chapter IV to give the design and analysis of the antennas in which the subreflector is replaced by a shaped dielectric reflecting surface. The antennas obtained by using the procedure of Chapter IV do not provide any control on the main aperture distribution.

The generalized design, based on geometrical optics, of the dual reflector antennas with a dielectric cone feed is presented in Chapter V, followed by an analysis and comparison of this system with an ordinary Cassegrain system. Finally, Chapter VI deals with the conclusions drawn from the present study and some suggestions for further work.

Numerical computations played an important part in the present research. Almost every result is a consequence of one or more computer programs. The procedures used for preparing these programs are referred wherever necessary and a listing of the programs is available upon request [ Chugh,1978 ].

REFLECTOR ANTENNAS

CHAPTER II

## 2.1 INTRODUCTION

The basic reflector antenna consists of a relatively small feed and a large reflecting surface. The large reflecting surface provides an increase in the gain, the value of which depends upon the geometrical characteristics of the reflector and the feed pattern. The geometrical characteristics of the reflector are the surface curvature and the boundary profile [Hansen, 1964]. The surface curvature can either be generated by one of the arcs like circular, parabolic, hyperbolic etc., or a shaped surface. The boundary profile is often either a rectangle containing a cylinder of the single curvature or a circle made by the revolution of some arc. Thus, many types of reflectors can be obtained by choosing any of the combinations for surface curvatures and the boundary profiles.

The plane reflector, because of simplicity, was one of the first reflectors to be used in practice. A plane reflector when placed near the radiating element reduces the backward radiation and also provides a gain in the forward direction. The gain improvement can be increased by a combination of two or more reflectors. The corner reflector antenna made up of two plane reflectors intersecting at an angle can produce gains as high as 14 dB with a single feed element [Jasik, 1961, pp. 12-2].

The antennas for communication or for radar purposes require a larger value of gain than that usually obtainable with the plane reflectors. The most common type of reflector used for high gain antennas is the parabolic reflector. The parabolic reflector has the property of transforming the waves originating from a source at the focus into a pencil beam. The

parabolic arc can either be used to form a parabolic cylinder or a paraboloid of revolution. A cylindrical parabola converts a cylindrical wave from an inphase line source at the focus into a plane wave at the aperture [Wolff, 1966]. A paraboloid of revolution converts a spherical wave from an isotropic source at the focus into a uniform plane wave at the aperture. The reflector antennas with paraboloidal reflector have been used for several decades in microwave relay systems and in radio astronomy. With this reflector, a pencil beam is generated by using a point source feed. The shaped or multiple beams can be generated by using different feed arrangements [Hansen, 1964].

Another antenna used for communication purpose is the spherical reflector. This antenna obtained by the rotation of a circular arc about an axis containing the center is well adapted for use as a wide angle scanning antenna [Li, 1959]. However, a source located at the focus of this sphere does not provide a perfect plane wave since a paraboloidal surface is necessary to create a plane wave. The departure of the wavefront from a plane wave is known as spherical aberration. The amount of aberration depends on the diameter of the sphere and the focal length [Wolff, 1966]. The on-axis aberrations can be compensated by the methods including the use of phased line source feeds, multiple source feeds, auxiliary reflectors or correcting lenses [Hansen, 1964]. With these methods a large aperture can be effectively used at the expense of some complexity in design.

Other types of reflector systems such as stepped reflectors, polarized reflectors, and lensed reflectors can also be used to generate pencil beams [Hansen, 1964]. However, these systems are more complex,

usually for reasons of improving the scanning capability of the system, and therefore are not commonly used for communication purpose [Hansen, 1964].

The feed in the above mentioned single reflector systems is usually placed in the path of the main beam, thus blocking the main aperture and making it difficult to be reached for servicing purposes. The aperture blocking due to the feed and its supporting structure results in the decrease of the antenna gain and an increase in side lobe level [Ruze, 1968]. In recent years, two reflector systems are becoming more common mainly due to the mechanical attractiveness of having a complex feed system and its associated electronic equipment at the rear of the main reflector [Hannan, 1961]. Some of the commonly used classical two reflector systems will be described in the second section.

The blockage in dual reflector systems, due to the subreflector and its supporting structure, is more predominant than in the single reflector systems. This is due to the size of the subreflector, which is usually larger than the feed systems for the single reflector antennas. The heavier subreflector in the dual reflector systems also requires a thicker supporting structure. Some calculations for the aperture blockage in the classical Cassegrain system will also be presented in the second section to determine their relative contributions.

The aperture blockage in the above mentioned rotationally symmetric single and dual reflecting systems can be removed by either using offset systems [Cook et.al., 1965; Pagones, 1968; Maanders, 1975] or supporting the main reflector or the subreflector with a dielectric

cone [Bartlett and Moseley, 1966]. The offset systems have the feed or the subreflector located outside the path of the ray trajectories for the main beams. The offset systems thus lose the symmetry of the front fed systems or the Cassegrain system and have a higher level of cross-polarization component [Maanders, 1975]. The Cassegrain antenna with a dielectric cone to support the subreflector is being studied in the present work. The basic principle of its operation can be found in the paper by Bartlett and Moseley (1966). The use of the dielectric cone is gradually becoming popular in practice [Petrick and Abrahamson, 1974; Buchmeyer, 1977] due to its obvious advantages of low aperture blockage and low spillover loss.

In many applications such as search and ground mapping radars it is desirable to have a shaped beam in one or both planes. A method for obtaining a shaped beam of an arbitrary shape in one plane and uniformly narrow in the perpendicular planes has been described by Dunbar (1948). This method based upon the principle of conservation of energy and simple laws of geometrical optics is valid for obtaining the surface curvatures of a single reflecting system. Some of the procedures used these days for shaping the dual reflector systems will be described in the third section. Finally, the last section will present a summary of the developments in reflector antennas.

## 2.2 CLASSICAL DUAL REFLECTOR SYSTEMS

### 2.2.1 Types of Classical Systems

The general dual reflector system consists of a subreflector to reflect the waves incident from the feed element to the main reflector and a main reflector to transform the energy incident on it from the secondary reflector into the main beam. Each of these two reflectors can have any of the classical shapes like parabola, hyperbola, ellipse or circle. Some of the common combinations are described below.

The most common of the two reflector systems is the Cassegrain system. This consists of a parabolic main reflector and a hyperbolic subreflector. The secondary reflector is situated between the focal point and the vertex of the main or primary reflector, with one of the two foci being coincident with the focal point of the main reflector. The position of the remaining focal point determines the system focal point and thus the position of the feed system. The performance of the Cassegrain system is sometimes evaluated by means of the equivalent parabola [Hansen, 1964]. The equivalent parabola concept can be used to evaluate the performance of the Cassegrain system with the exception of the effects of aperture blocking and diffraction due to subreflector and supporting structure.

The classical Cassegrain system may easily be extended to include a variety of forms [Hannan, 1961] by varying the curvatures of the two reflectors. The common variation of the Cassegrain system is the Gregorian

system (Fig. 2.1). The Gregorian system is similar to the Cassegrain system in that a parabolic reflector is used, however, the subreflector in this configuration is elliptic in shape rather than hyperbolic. Since the location of the two foci of an ellipse are on the same side of the surface, the subreflector is situated further out than the focal point of the main reflector. The Gregorian system is commonly used in radio astronomy for use of simultaneous multiple frequency feeds,

The non-Cassegrain system [Visocekas, 1964], although superficially similar to the Cassegrain system, is fundamentally different. This system uses a parabolic subreflector whose focus is set exactly at the focus of the main parabolic reflector. In this system, similar to the Gregorian system, the subreflector is situated further out than the focal point of the main parabolic reflector.

The spherical reflector with a Gregorian subreflector is also being considered for satellite communication earth stations [Phillips and Clarricoats, 1970]. The main advantage of this dual reflector system is the scanning capability over a small angle. However, this system has not found much application due to the higher side lobe level as compared to the Cassegrain system.

The other dual reflector system being considered in literature is the conical-Gregorian antenna [Ludwig, 1972]. In this system the conical main reflector is fed from a subreflector in conjunction with a conventional horn feed. This system when compared to front fed paraboloid or Cassegrain systems has much lower cost and the mechanical advantage of single curved surface.

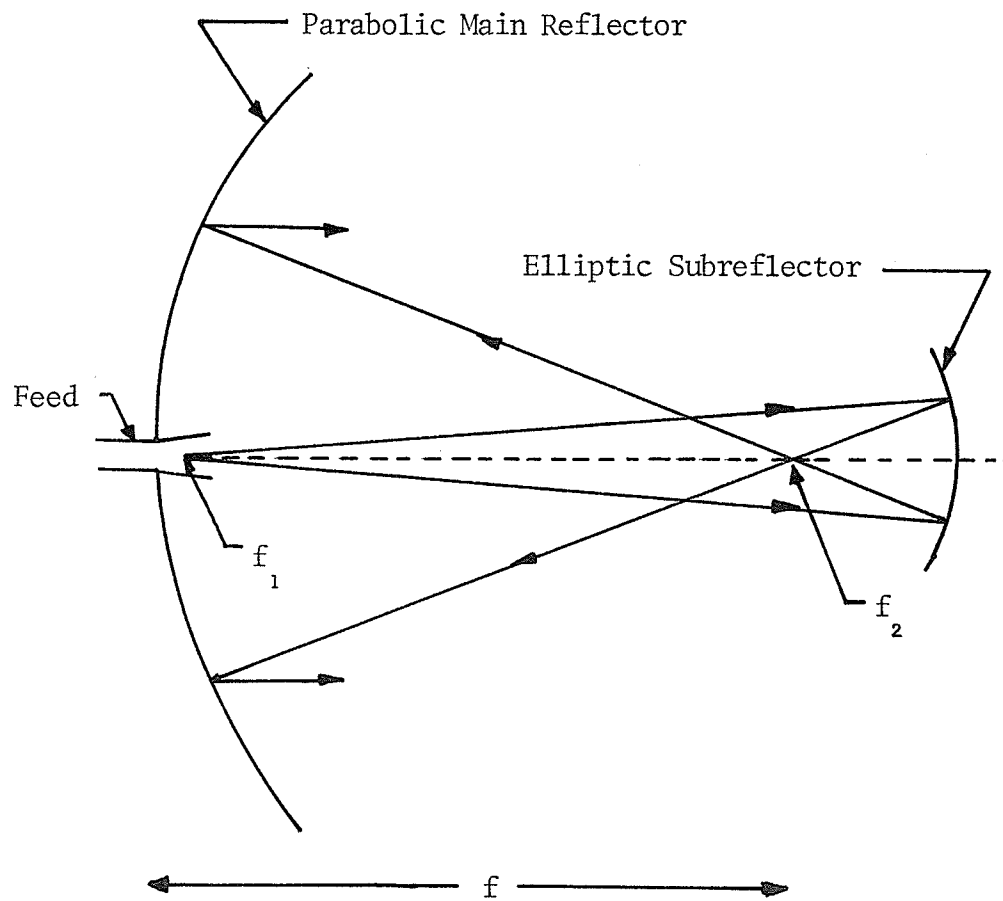


Fig. 2.1 Classical Gregorian antenna

All the above mentioned dual reflector systems have the advantage of convenient feed location between the two reflectors or closer to the main reflector. This reduces the feed line losses and can be reached more conveniently for servicing purposes. The disadvantages of the dual reflector systems include the diffraction, spillover loss from two reflectors and the aperture blockage. Although the aperture blockage appears in front fed paraboloids as well, the consequences are less severe, as the feed is typically smaller than the subreflector and the support legs much thinner [Dijk et.al., 1971]. The effect of the aperture blockage on the gain of classical Cassegrain system will be considered in the next section.

#### 2.2.2 Aperture Blockage in Cassegrain Antenna

A basic limitation of most dual reflector antennas, such as Cassegrain antennas, is the blockage of the aperture by the subreflector and its supporting structure. The first order approximation of the aperture blockage was based upon the ray optics shadow of the blocking component and the zero-field concept [Ruze, 1968; Rusch and Potter, 1970; Dijk et.al., 1971]. However, the zero-field in these shadows does not give adequate prediction of the gain, side lobe level and antenna efficiency [Breithaupt, 1966]. It was determined by Breithaupt (1966) that an opaqueness factor of 0.6 gives the antenna parameters which agree very well with the measured values. These investigations, however, did not provide any information on the effects of changes in operating frequency and polarization.

A more accurate description of the blockage requires an investigation of this at microwave frequencies. The operating frequencies in the microwave region result in the shadows which are wider than

the optical shadows [Rusch and Sørensen, 1974]. In principle, this effect can be described by adding the edge diffracted rays to the reflected rays from the subreflector. However, when the subreflector size is large compared to a wavelength, the geometrical shadow approximation provides the results with reasonable accuracy, provided that the angles of observation are not far from bore sight [Silver, 1949; Collin and Zucker, 1969; Rusch and Potter, 1970].

The first order approximation to the analysis of the support structure blockage, due to its presence in the main beam path of the Cassegrain antenna, was based on zero-field concept and optical shadow [Dijk et.al., 1971]. This analysis, however, does not take into account the depth, cross-section, or the tilt of the struts, nor does it provide any differences for frequency or polarization effects [Rusch and Sørensen, 1974; Shafai et.al., 1977]. To account for these effects, Rusch and Sørensen (1974) introduced a concept named IFR (induced field ratio). This is based on the assumption that the struts in the Cassegrain antenna act like infinitely long cylindrical structures in the path of plane waves. The assumption of the incident field being a plane wave is not exactly true in the actual case. However, it is a useful first step in "coming to grips" with the problem of strut blocking [Rusch and Sørensen, 1974].

The induced field ratio is defined to be a measure of the forward scattered field of an infinitely long cylindrical scatterer when it is immersed in an incident plane wave. These ratios, corresponding to  $E_z$  and  $H_z$  polarizations of the incident plane wave, for a right circular cylinder of radius  $b$  are given by

$$\text{IFR}_E = - \frac{1}{kb \cos\alpha''} \sum_{n=-\infty}^{\infty} [J_n(kb \cos\alpha'') / H_n^{(2)}(kb \cos\alpha'')] \quad (2.1)$$

$$\text{IFR}_H = - \frac{1}{kb \cos\alpha''} \sum_{n=-\infty}^{\infty} [J'_n(kb \cos\alpha'') / H_n^{(2)'}(kb \cos\alpha'')] \quad (2.2)$$

respectively. In the above equations

$\alpha''$  = tilt angle of the strut relative to the incident plane wave,

$k$  = propagation constant,

$J_n(X)$  = Bessel function of order  $n$  and argument  $X$ ,

$H_n^{(2)}(X)$  = Hankel function of second kind of order  $n$  and argument  $X$ ,

and the primes denote the derivatives with respect to the arguments. The IFR's for a right circular cylinder are plotted in Fig. 2.2. As indicated in Fig. 2.2, both the IFR's approach the value  $-1.0 + j 0.0$  as the radius increases, one from the second quadrant of the complex plane and the other from the third quadrant. Therefore, as the radius of the cylinder becomes much larger than wavelength, the results obtained by using IFR hypothesis approach the results using zero-field concept.

The blockage of the support structure due to its presence in the feed path was approximated in the earlier investigations by using trapezoids [Maanders, 1975]. More recently, this procedure has been replaced by an analysis using exact optical shadow [Shafai et.al., 1977]. However, this approach does not provide any information of the effects of polarization and frequency, since it is based on the principle of optical shadowing.

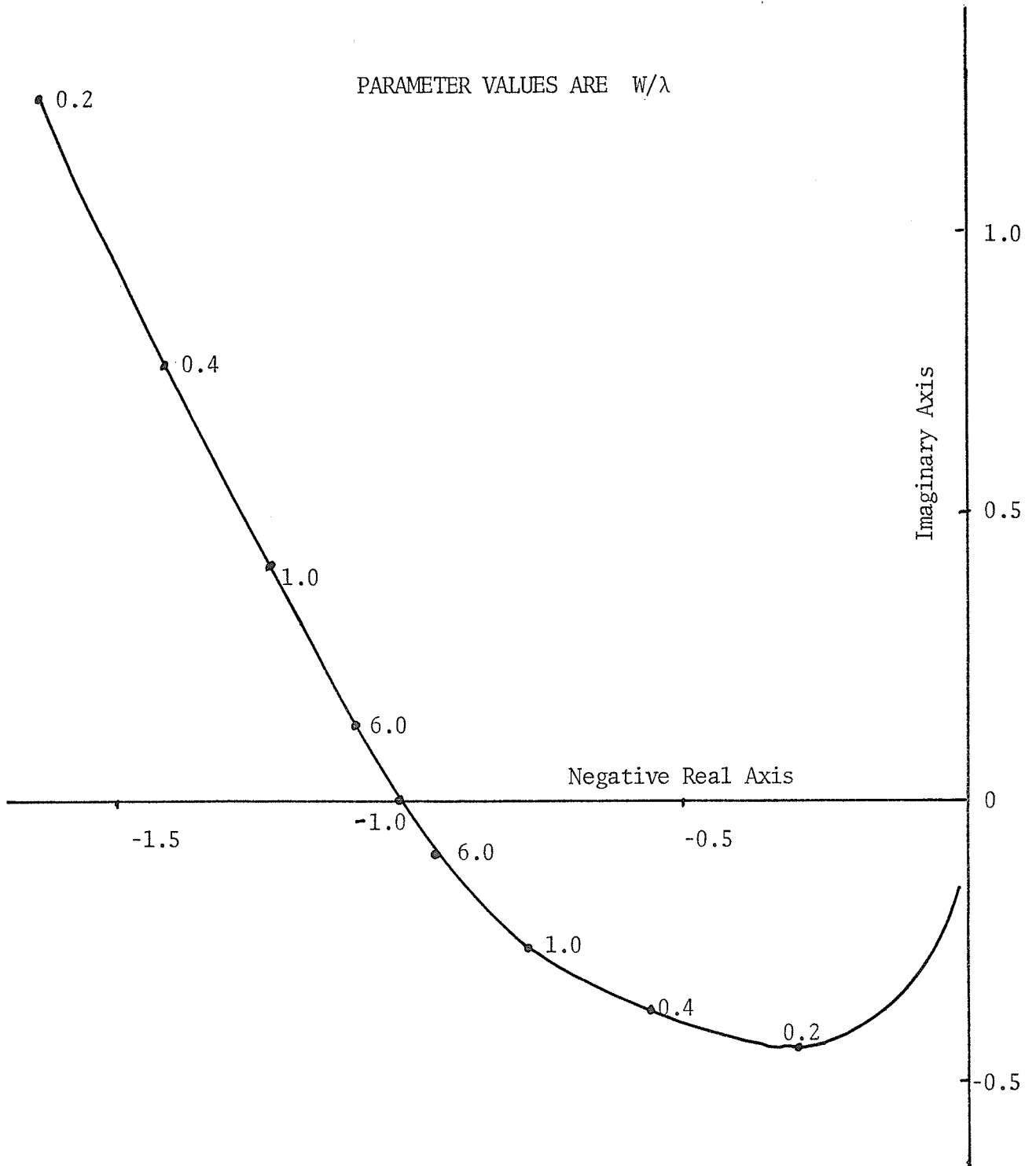


Fig. 2.2 Complex  $IFR_E$  and  $IFR_H$  for a circular cylinder [Rusch and Sørensen, 1974].

The above paragraphs provide a brief summary of the procedures used these days to analyse the effects of the blockage in the Cassegrain antennas due to the subreflector and its supporting structure. These procedures, with some added complexity, have led to a better understanding of the blockage contribution on the gain, side lobe level and polarization of the main radiation pattern. However, the simpler procedure based on the zero-field concept and optical shadowing are used in the following paragraphs to obtain the qualitative results of the blockage contribution.

The optical shadows in the aperture due to the subreflector and its support structure are indicated in Fig. 2.3. The total blockage can be divided into three major areas as follows:

- (1) The central obstacle or the subreflector shows a shadow on the aperture obtained by projecting the subreflector by a plane wave (Fig. 2.3a).

- (2) The portion of the plane wave obstructed by struts is found by projecting the struts on the main reflector aperture by a plane wave (Fig. 2.3b).

- (3) The third shadow is formed by projecting the support legs on the aperture by a spherical wave with its phase centre in the focus (Fig. 2.3c).

The effects of these shadow regions on the gain and antenna efficiency can be calculated by using the current distribution or aperture field methods [Silver, 1949]. A calculation of the current distribution over the main reflector is difficult because of the interaction between the

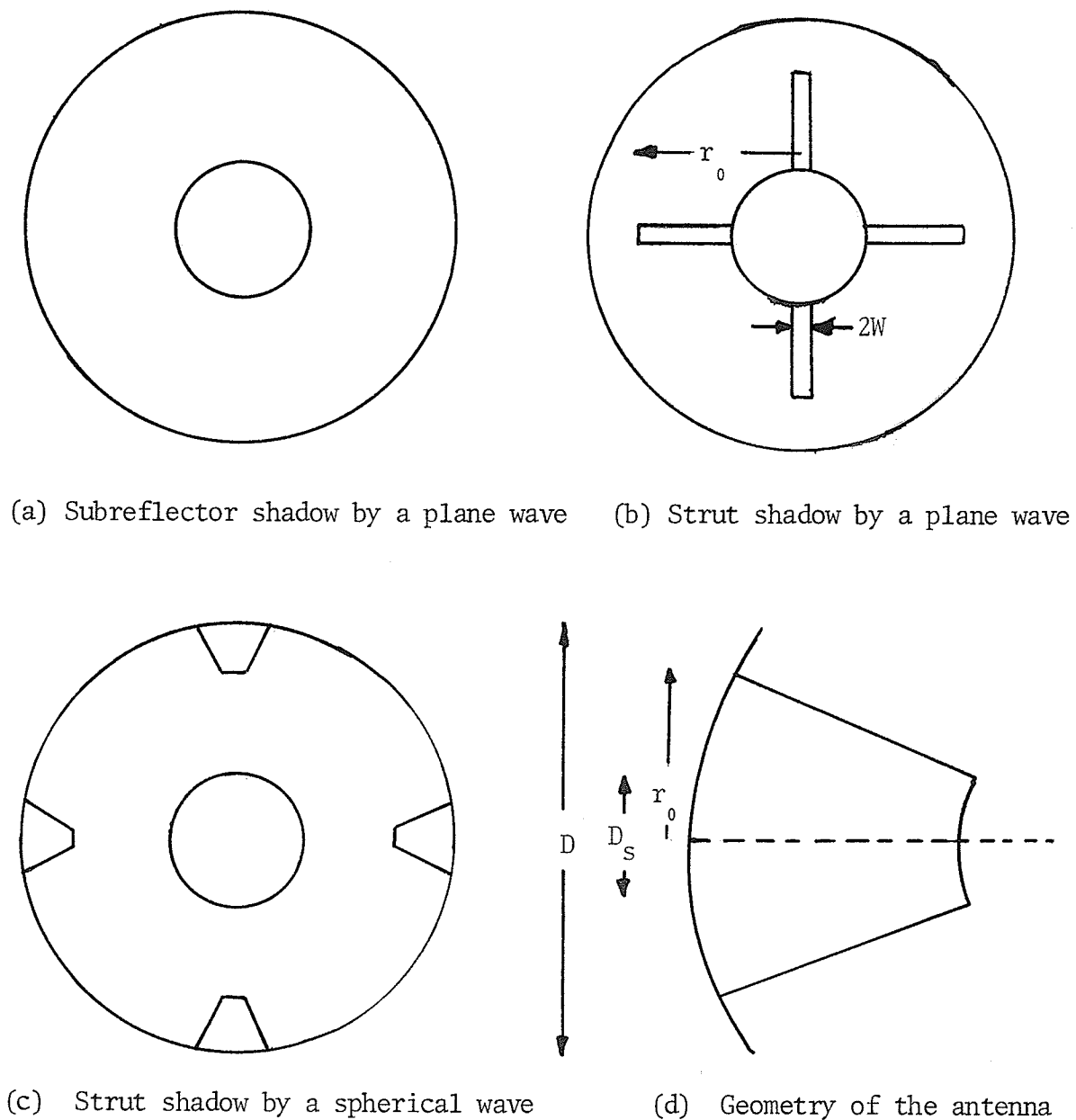


Fig. 2.3 Optical shadowing by plane and spherical waves in the Cassegrain antenna with four struts

obstacle and the source system [Maanders, 1975]. An approach may be found in the geometrical theory of diffraction [Keller, 1962], however both geometrical theory of diffraction and aperture field methods provide only an approximate solution. Hence, only approximate methods or the experiments give an answer for the influence of blockage on the gain and radiation pattern.

Using the aperture field method [Silver, 1949], the relative far field directive gain pattern of a rectangular aperture near main axis may be represented by the scalar equation

$$g(\theta', \phi') = \int_A F(x, y) \exp[jk \text{Sin}\theta'(x \text{Cos}\phi' + y \text{Sin}\phi')] dx dy \quad (2.3)$$

and that of a circular aperture by

$$g(\theta', \phi') = \int_A F(\rho, \phi) \exp[jk\rho \text{Sin}\theta' \text{Cos}(\phi - \phi')] \rho d\rho d\phi \quad (2.4)$$

where  $g$  is the gain at observation angles  $\theta'$  and  $\phi'$ ;  $F$  is the aperture amplitude distribution; and  $k$  is the propagation constant. These equations along with "zero-field concept" [Rusch and Potter, 1970] are used in Appendix A to find the total gain pattern.

The zero-field concept involves the subtraction of the blocked aperture gain from the unblocked one to obtain the true gain. If  $g_0$ ,  $g_1$ ,  $g_2$  and  $g_3$  are the gains of the unblocked aperture, subreflector, plane wave strut contribution, and spherical wave strut contribution, respectively, then the total gain pattern  $g_t$  is given by [Maanders, 1975]

$$g_t(\theta', \phi') = g_0(\theta', \phi') - g_1(\theta', \phi') - g_2(\theta', \phi') - g_3(\theta', \phi') \quad (2.5)$$

The blockage efficiency as derived in App. A as eq. (A.24) is given by

$$\frac{\eta_B}{\eta_0} = \left| 1 - \frac{g_B(0,0)}{g_0(0,0)} \right|^2 \quad (2.6)$$

where  $\eta_B$ ,  $\eta_0$  are the efficiencies and  $g_B$ ,  $g_0$  are the gains of the blocked and unblocked apertures, respectively. It should be noted that  $g_B$  has the values  $g_1$ ,  $g_2 + g_3$ , or  $g_1 + g_2 + g_3$  for the blockage efficiencies of the subreflector, support structure, or the total blockage, respectively.

The four parameters which influence the aperture blockage are the subreflector diameter  $D_s$ , support structure width  $W$ , the end point of the support structure on the main reflector  $r_0$ , and the aperture amplitude distribution. The results of variations of these parameters are plotted in Figures 2.4 - 2.7, where the contributions of the subreflector and support structure are plotted along with the total blockage efficiency.

The contribution of the subreflector to the blockage increases with an increase in subreflector diameter, thus reducing the blockage efficiency, as shown in Fig. 2.4. An increase in subreflector diameter reduces the plane wave as well as the spherical wave contribution of the support structure resulting in increased blockage efficiency. The total blockage efficiency has a maximum around  $D_s/D = 0.22$  where an efficiency of 0.62 is obtained for uniform aperture amplitude distribution.

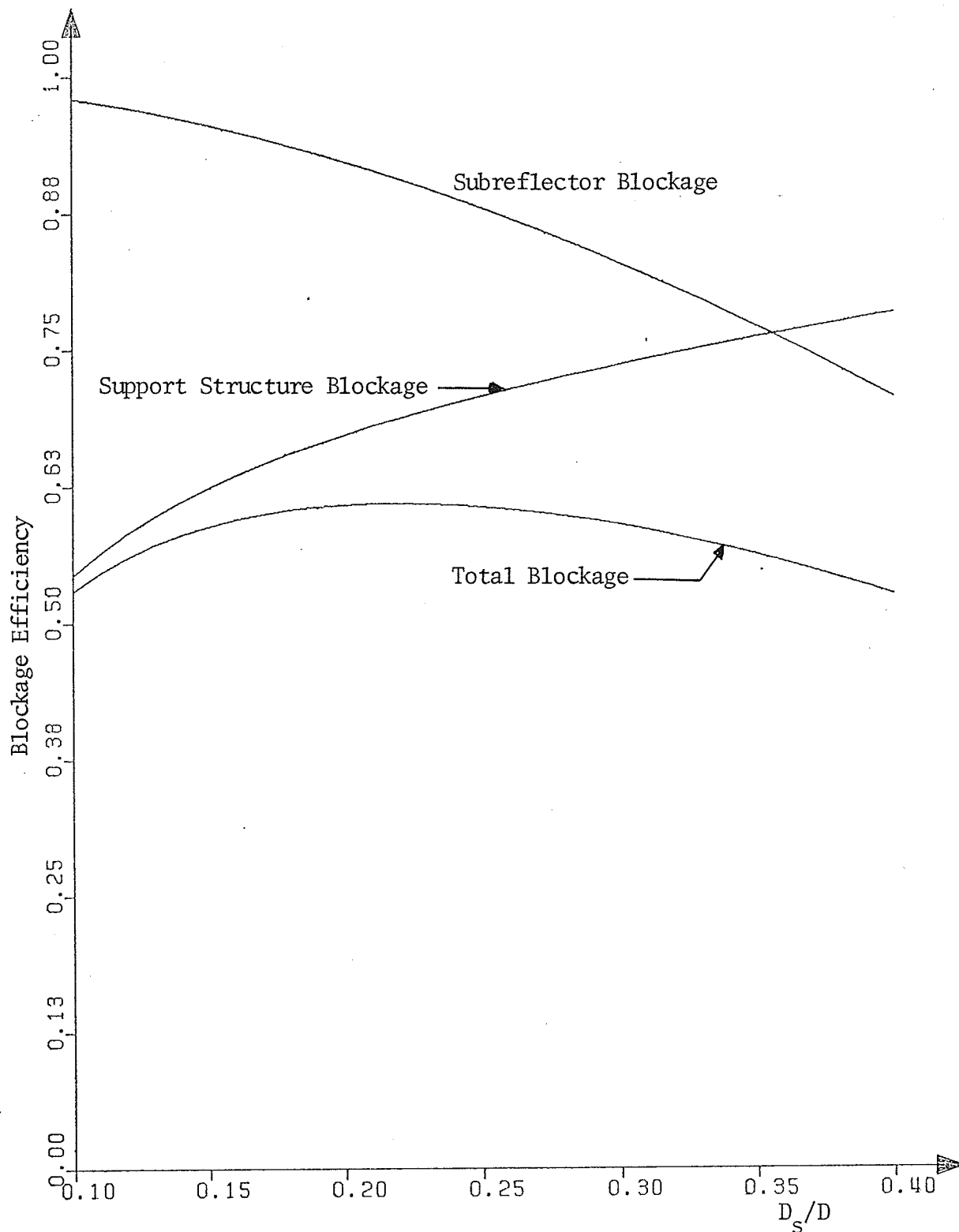


Fig. 2.4 Variation of blockage efficiencies in the Cassegrain antenna with subreflector diameter for  $D = 48\lambda$ ,  $W = 1.5\lambda$  and  $r_0 = 20\lambda$

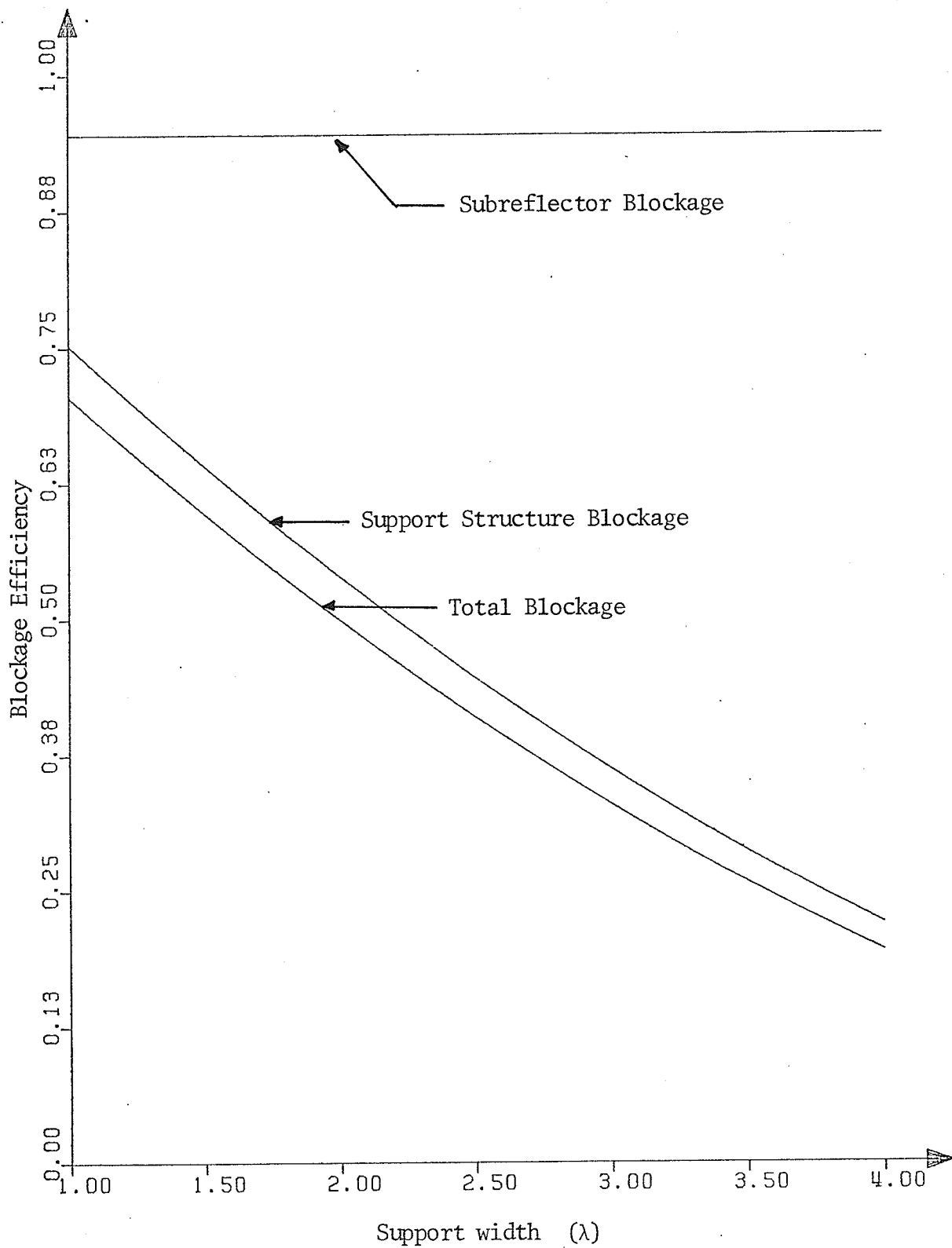


Fig. 2.5 Variation of blockage efficiencies in the Cassegrain antenna with the width of the supporting structure for  $D = 48\lambda$ ,  $D_s = 8\lambda$  and  $r_0 = 20\lambda$

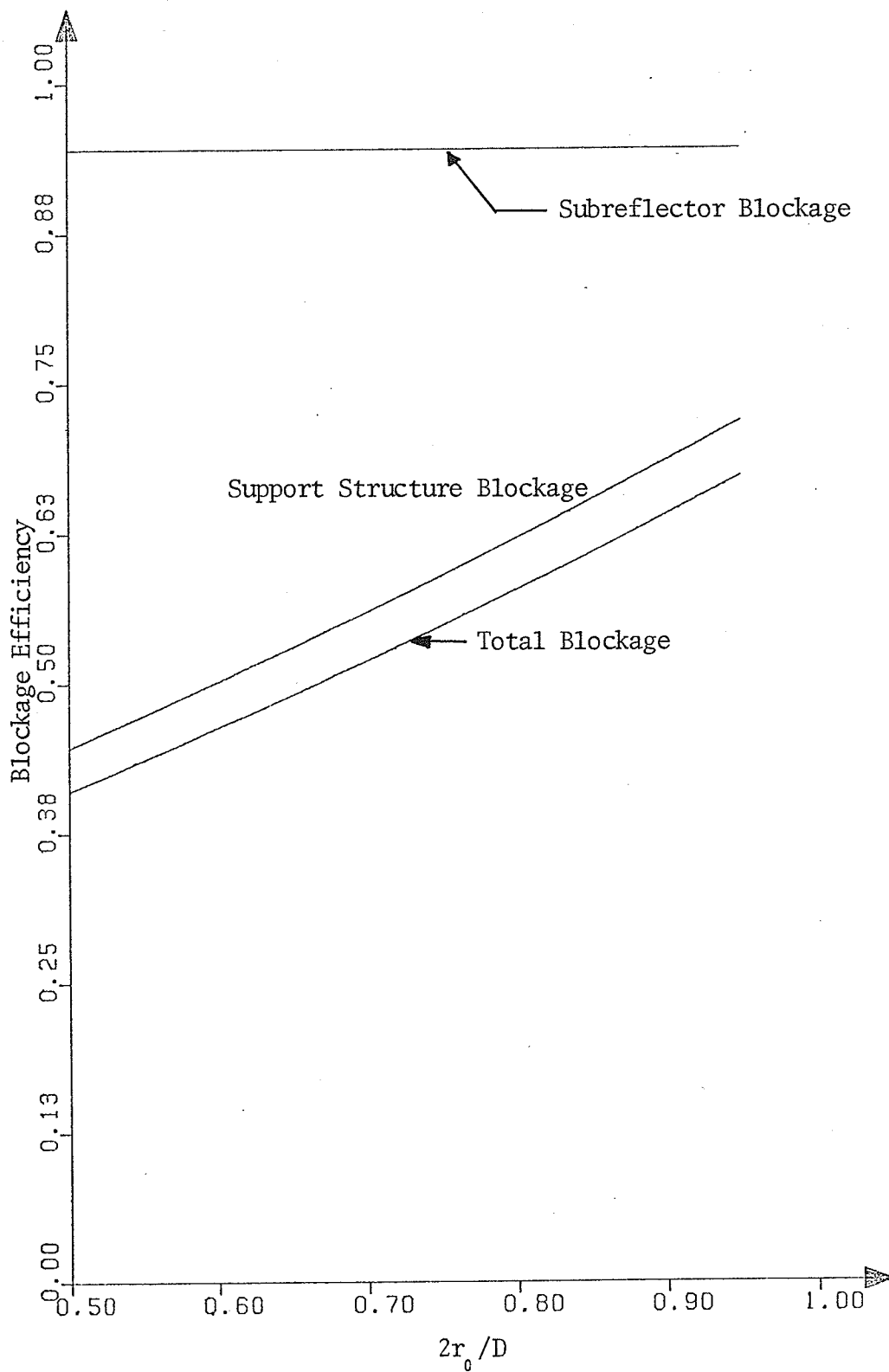


Fig. 2.6 Variation of blockage efficiencies in the Cassegrain antenna with support point movement for  $D = 48\lambda$ ,  $D_s = 8\lambda$  and  $W = 1.5\lambda$

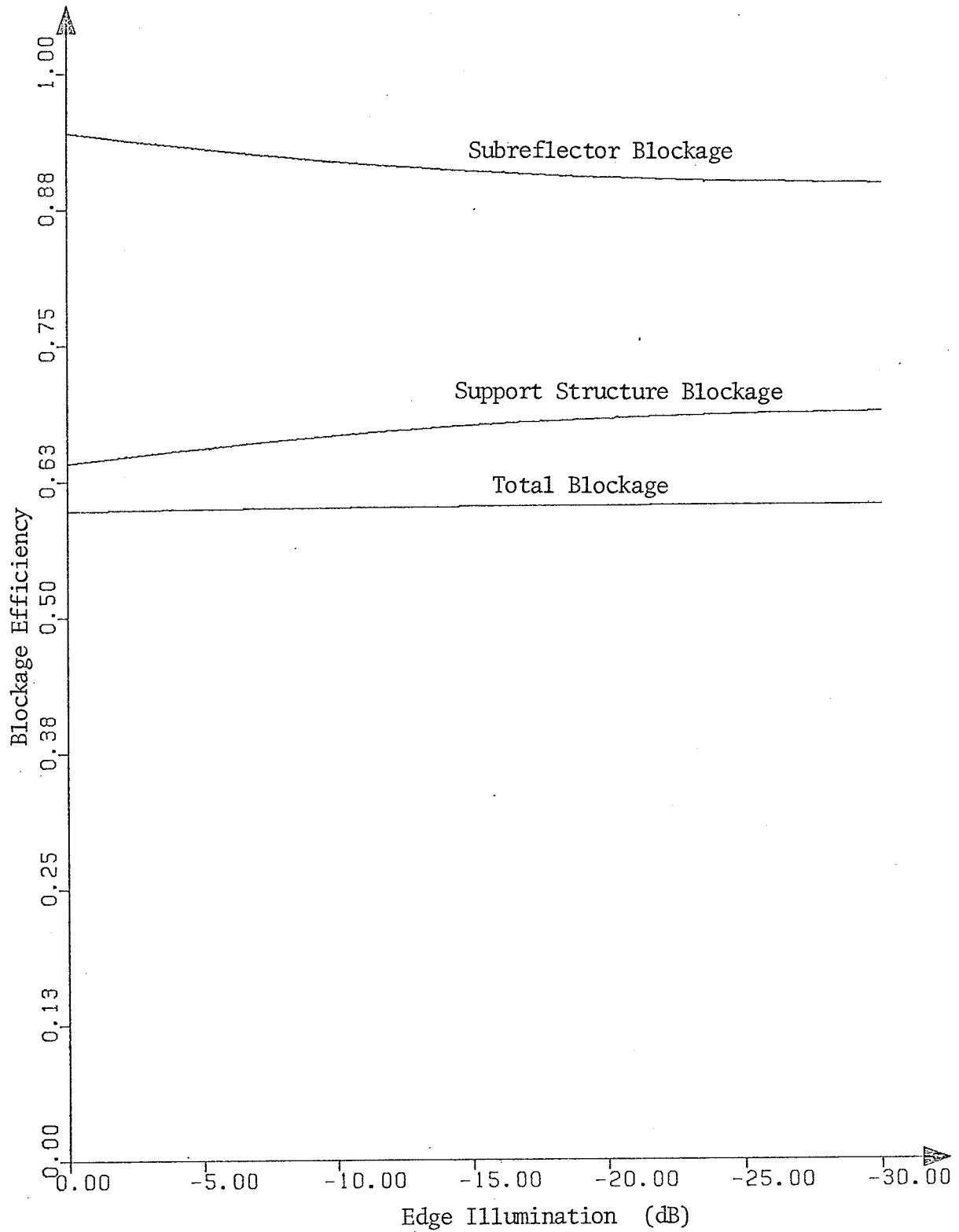


Fig. 2.7 Variation of blockage efficiencies in the Cassegrain antenna with the edge illumination of the main reflector  $D = 48\lambda$ ,  $D_s = 8\lambda$ ,  $r_0 = 20\lambda$  and  $W = 1.5\lambda$

The increase in support structure width does not change the blockage due to subreflector, as shown in Fig. 2.5. As expected the support structure contribution increases very rapidly with an increase in the width. For minimum blockage loss due to support structure the width should be as small as possible.

The movement of the support end point on the main reflector does not affect the contribution of the subreflector blockage, as shown in Fig. 2.6. The movement of the end point towards the edge results in an increased contribution due to plane wave shadow and decreased contribution of the spherical wave shadow. The overall effect of these two is a decrease in support structure contribution. For improving the efficiency, the end point should be as close to the edge as possible.

The change in aperture amplitude distribution reduces the overall efficiency of the system, although there is zero change in total blockage efficiency (Fig. 2.7). This is due to a decrease in aperture efficiency with an increase in edge illumination. The subreflector contribution increases due to an increases percentage power being blocked by the subreflector. On the other hand, the support structure contribution decreases due to the reduced weightage of spherical shadow.

In the above paragraphs the obstacle contributions to the blockage efficiency for various parameters are presented based on zero-field concept. One common feature in all these curves is that the support structure contribution is much more important than the subreflector contribution in all cases except when  $D_s/D$  is larger than 0.36.

### 2.3 SHAPED DUAL REFLECTOR SYSTEMS

The effect of aperture blockage in the dual reflector systems, such as Cassegrain system, on the antenna efficiency can be calculated by appropriately weighting the optical shadow and the aperture illumination. The amplitude and phase distribution in the aperture plane of main reflector has an important bearing on antenna efficiency [SciamFi, 1965]. In order to achieve an optimum amplitude and phase distribution in the aperture of main reflector, the only degree of freedom for design is in the feed. When the feed achieves a "best" design no further improvements of antenna performance can be realized [Rusch and Potter, 1970]. Recently, however, machine computation has enabled the two parameters which had previously been considered constraints, i.e., the two reflector shapes, to be modified.

The first general treatment for the problem of passing from an initial field with an arbitrary amplitude and phase to a final field with arbitrary distribution is based on the principles of geometrical optics [Kinber, 1962]. It is shown that a primary field with an arbitrary amplitude and phase distribution cannot, in general, for a three-dimensional case, be transformed into an arbitrary secondary field with the aid of two reflectors. However, it is possible to achieve this transformation by using rotationally symmetric dual reflectors [Galindo, 1964].

The design procedure uses two linear equations, for aperture amplitude and phase distributions, and two differential equations, for the Snell's laws at the two reflectors, to develop a pair of nonlinear

differential equations [Galindo, 1964]. These nonlinear differential equations are solved by a digital computer to obtain the surface curvatures of the two reflectors. The procedure is sufficiently general to allow useful variations of the design objectives.

The above mentioned design procedure has been used to obtain overall high efficiency antenna reflector [Williams, 1965]. A higher efficiency is obtained by selecting, from a given feed pattern, a taper level to give high spillover efficiency from the subreflector and then designing the reflectors to obtain uniform illumination. Using this method a gain improvement of 1 dB has been indicated [Williams, 1965].

Another reflector synthesis technique [Potter, 1962] proceeds along different lines from the geometrical technique described above. The feed system, consisting of a primary feed and subreflector combination, is required to produce a spherical wave front at "infinity" within a specified angular region. The spherical wave expansion technique, in conjunction with machine computation, then yields a subreflector contour and primary feed radiation pattern which produces the desired feed system radiation pattern. The contour of the synthesized subreflector has a flange at the end to reduce spillover losses. However, the subsequent work [Potter, 1966] gives the impression that the solution is not found ideal.

The research on shaped dual reflector systems is still going on to obtain even more improvements. The geometrical considerations have been applied to shape the reflectors with a plane wave feed [Morgan, 1964].

This study indicated that the antennas which image the feed aperture on to the main reflector along with efficient illumination efficiency are not of practical importance. A technique has been proposed for raising the efficiency of spherical reflector antennas with the Gregorian method of phase correction [Clarricoats and Lim, 1969]. In this way the efficiency of the spherical reflector may be improved considerably.

The above techniques help to reduce the losses due to the aperture amplitude and phase distribution. However, the aperture blockage and diffraction due to supporting structure still require further investigation.

#### 2.4 SUMMARY AND DISCUSSION

The antennas for radar or communication purposes require a large value of gain which can be produced either by building up space arrays of dipoles, slots, horns, helices, loops, and spiral antennas [Kraus, 1950] or by the use of reflectors and lenses with these antennas acting as a feed. However, the array type antennas become very complex to design and operate for gains greater than 30 dB [Jasik, 1961] thus leaving reflector antennas as the alternative.

The most common type of reflector used for high gain antennas is the parabolic reflector. This type of reflector is very convenient in microwave frequency range, where apertures of many wavelengths are practicable. The paraboloidal reflector, obtained by rotating a parabola about its axis, generates a pencil beam by using a point source feed at focus.

The shaped or multiple beams can be generated by using different feed arrangements.

The aperture blocking by the feed and its supporting structure results in a reduced gain and increased side lobe level [Ruze, 1968]. Also, the front location of the feed makes it difficult to be reached for servicing purposes. In relatively recent years, a number of microwave antennas have been developed which employ dual reflectors similar to Cassegrain telescope [Hannan, 1961]. The general double reflector system, when compared with the single reflector type, achieves a high magnification with a short focal length and allows a convenient rear location of the feed or the observer.

The most common dual reflector system, Cassegrain antenna, consists of a parabolic main reflector and hyperbolic subreflector. One of the foci is the real focal point of the system and is located near the main dish. The other focus is a virtual focal point located at the focus of the paraboloid. The primary feed located at the real focal point results in a plane wave front after reflection from the two reflectors.

A disadvantage of the Cassegrain system is the decrease in antenna efficiency due to blockage and diffraction introduced by the subreflector and its supporting structure. Diffraction occurs since the dimensions of the subreflector are not large compared with wavelength. Some approximations have been made for the effect of diffractions on antenna performance, but still it requires further study [Maanders, 1975]. The effects of aperture blockage have been calculated by using the aperture

field method. As is evident from the results presented in Section 2.2.2, the contribution of supporting structure is much larger than that of the subreflector. The supporting structure contribution can be reduced by increasing the subreflector diameter, reducing the supporting arm width, moving the arm towards the edge of the main reflector, and reducing the edge illumination. An increase in subreflector diameter reduces the blockage efficiency, thus not providing a good solution. The support arm cannot be made thinner and moved to the outer edge beyond a certain limit due to mechanical limitations. Reducing the edge illumination reduces the overall efficiency of the system because of reduced aperture efficiency. Therefore, a compromise has to be made to obtain the best efficiency.

A further limitation of the classical Cassegrain antenna lies in the fact that the aperture illumination is mostly so selected that the antenna gain reaches a maximum. By doing this, the aperture illumination is fixed and no means of controlling the efficiency and side lobes are available [Rusch and Potter, 1970]. The possibility of obtaining a specified aperture distribution has been demonstrated for circularly symmetrical reflectors [Galindo, 1964]. In this way the efficiency of the dual reflector system may be considerably improved and also the reflectors can be designed to remove the subreflector blockage. Also, it is possible to illuminate the edge of the subreflector at values as low as -20 dB to provide higher spillover efficiency and low noise figures [Maanders, 1975].

The design technique based on geometrical considerations does not, however, reduce the aperture blockage due to supporting structure.

The best alternative to remove this blockage will be to support the sub-reflector by some other means. Recently, the efficiency of microwave antennas has been improved with the use of a dielectric cone to support the subreflector [Bartlett and Moseley, 1966]. However, in this technique the reflectors used had the classical shapes. In the present work an attempt has been made to shape the dielectric cone fed reflector antennas for an arbitrary field distribution.

CHAPTER III

FEEDS FOR REFLECTOR ANTENNAS

### 3.1 INTRODUCTION

The design requirements and specifications of an antenna feed are usually governed by the purpose of the antenna and the operating frequency. Some of the requirements imposed on the feeds which illuminate microwave reflectors are as follows:

- (a) minimum spillover loss,
  - (b) independence of phase centre on operating frequency,
  - (c) perfect matching to the transmission line, source or detector,
  - (d) low cross-polarization components
- and
- (e) ideal edge taper.

One of the first microwave antenna feeds, adapted from the practice at longer wavelengths was the dipole feed [Silver, 1949]. Due to the pattern properties of a dipole, a reflector plate is required to obtain the directivity. These days dipole feeds are being used as a feed for backfire antennas [Ehrenspeck, 1974].

The other feeding configurations used for reflector antennas include helical, planar spiral, conical spiral and log-periodic antennas. The design and analysis of these feeds are available in many texts on microwave antennas [Jasik, 1961; Wolff, 1966; Collin and Zucker, 1969]. The radiation from these feeds has much larger bandwidth than the dipole feed and also these feeds do not require any special feeding arrangements to give polarization properties. However, the frequency dependence of the phase centre and the power handling capability limit their applications to

reflector antennas.

In the case of a reflector antenna that requires a line source feed, dipole and horn arrays as well as slotted waveguide arrays can be used [Silver, 1949; Cumming, 1963]. Pill box or cheese antennas have also been used as line source feeds.

The most common feeds for microwave reflector antennas are the horn feeds. The simplicity of design along with their excellent impedance, polarization and power handling capabilities have led to a wide usage of horn feeds since their advent.

Horns are constructed in a variety of shapes in order to control one or more of the four major electrical properties: gain, polarization, radiation pattern and impedance. Some of the basic shapes are the sectoral horns (either E- or H-plane sectoral horns), pyramidal horns, and conical horns. For circularly symmetric reflector antennas such as front-fed paraboloids and the Cassegrain system, the conical horn is the most appropriate choice due to circular symmetry.

A number of improvements have been made in the conical horn to achieve better performance for use as a feed in reflector antennas. The extension of conical horn to dual-mode horn antenna [Potter, 1963] provides the beamwidth equalization in all planes with at least 30dB side lobe suppression in the electric field plane. A conical horn antenna with grooves perpendicular to the wall of the horn has shown excellent properties for use as a feed for reflector antennas [Jansen et.al., 1969]. The attractive

properties of the scalar feed or corrugated horn feed led to a considerable research in this area [Clarricoats, 1969; Clarricoats and Saha, 1971]. The second reference also refers to the work in different countries up to 1971.

The use of a corrugated conical horn as a feed for Cassegrain antenna reduces the spillover but does not provide much improvement in supporting structure blockage. The characteristics of the corrugated conical horn feed and "dielguides" have shown to be similar to each other [Clarricoats, 1970]. In the present work, the dielguide is being used as a feed for the Cassegrain antenna. To understand the radiation pattern of reflector antennas with a dielectric cone feed (Chapters IV and V) it is necessary to predict accurately the radiation pattern of the horn with and without dielectric cone.

In this chapter a comparison will be made of the theoretical and experimental radiation patterns of the conical horns with and without dielectric cone. The radiation patterns are calculated using vector Kirchhoff integral formulation [Silver, 1949].

### 3.2 CONICAL HORN ANTENNA

The conical horn antenna is formed by flaring the walls of a circular waveguide as shown in Fig. 3.1. The usual method of exciting this antenna is through a rectangular waveguide with a transition from rectangular to circular waveguide. By virtue of its axial symmetry, the conical horn can handle any polarization of the dominant mode.



Schorr and Beck (1950) reported a modal representation for the modes in a semi-infinite perfectly conducting conical horn. A similar formulation was later used by Bailin and Silver (1956) to determine the radiation from the slots on a conical horn. Design data for conical horns is given by King (1950),

The radiation pattern of the conical horn can be calculated using either the aperture field integration technique [Silver, 1949] or the edge diffraction theory [Hamid, 1968]. The aperture field integration technique provided good results for cones with flare angles up to  $20^\circ$  [Schorr and Beck, 1950]. This was due to certain approximations made to ensure fast convergence of the integrals. Recently, a good agreement with the experimental data has been reported for cones with flare angles up to  $45^\circ$  using numerical methods [Narasimhan and Rao, 1971]. A similar approach will be used in the following sections to calculate the radiation patterns for the conical horn.

### 3.2.1 Characteristic Equation and Aperture Fields

Consider a perfectly conducting conical waveguide of flare angle  $\theta_e$  and slant length  $a$  with apex at the origin (Fig. 3.1). The fields inside the conical waveguide are assumed to be those for an infinitely long waveguide. The hybrid modes in the conical waveguide can be conveniently represented as super-positions of the fields TE to  $r$  and TM to  $r$  [Harrington, 1961]. Making an appropriate choice of the electric and magnetic vector potentials for the TE to  $r$  and TM to  $r$  fields, the field components can be evaluated from the following set of equations [Harrington, 1961].

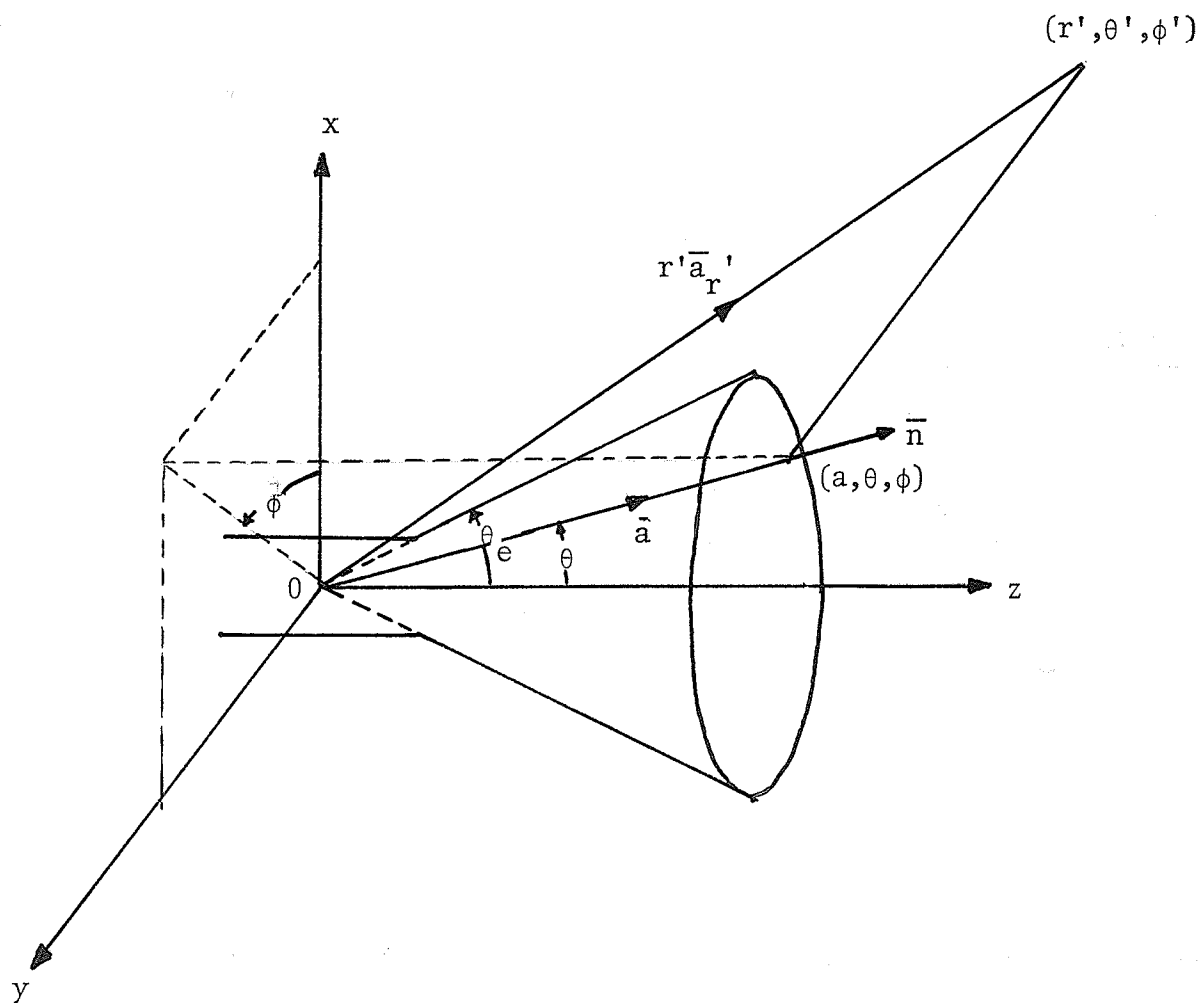


Fig. 3.1 Coordinate system for the conical horn antenna analysis

$$E_r = \frac{1}{j\omega\epsilon} \left( \frac{\partial^2}{\partial r^2} + k^2 \right) A_r \quad (3.1)$$

$$E_\theta = \frac{1}{j\omega\epsilon r} \frac{\partial^2 A_r}{\partial r \partial \theta} - \frac{1}{r \sin \theta} \frac{\partial F_r}{\partial \phi} \quad (3.2)$$

$$E_\phi = \frac{1}{j\omega\epsilon r \sin \theta} \frac{\partial^2 A_r}{\partial r \partial \phi} + \frac{1}{r} \frac{\partial F_r}{\partial \theta} \quad (3.3)$$

$$H_r = \frac{1}{j\omega\mu} \left( \frac{\partial^2}{\partial r^2} + k^2 \right) F_r \quad (3.4)$$

$$H_\theta = \frac{1}{r \sin \theta} \frac{\partial A_r}{\partial \phi} + \frac{1}{j\omega\mu r} \frac{\partial^2 F_r}{\partial r \partial \theta} \quad (3.5)$$

$$H_\phi = -\frac{1}{r} \frac{\partial A_r}{\partial \theta} + \frac{1}{j\omega\mu r \sin \theta} \frac{\partial^2 F_r}{\partial r \partial \phi} \quad (3.6)$$

In the conical waveguide the fields should have the periodicity in  $2\pi$  on  $\phi$ , finiteness at  $\theta = 0$  and also satisfy the radiation condition at infinity. Hence, the appropriate choice for TM to r mode functions with a time dependence  $e^{j\omega t}$  is as follows:

$$A_r = A_{mv} P_v^m(\cos \theta) h_\nu(kr) \cos(m\phi) \quad (3.7)$$

where  $m = 0, 1, 2, \dots$ ,  $P_v^m(\cos \theta)$  and  $h_\nu(kr)$  are the associated Legendre function and the spherical Riccati-Hankel function of second kind, respectively. For this choice of vector potential, the field components for TM to r modes calculated by using equations (3.1) - (3.6) are as follows:

$$E_r = \frac{A_{mv}}{j\omega\epsilon} \frac{\nu(\nu+1)}{r^2} P_v^m(\cos \theta) h_\nu(kr) \cos(m\phi) \quad (3.8)$$

$$E_{\theta} = \frac{A_{mv}}{j\omega\epsilon} \frac{k}{r} \frac{dP_{\nu}^m(\cos\theta)}{d\theta} h'_{\nu}(kr) \cos(m\phi) \quad (3.9)$$

$$E_{\phi} = - \frac{A_{mv} km}{j\omega\epsilon r} \frac{P_{\nu}^m(\cos\theta)}{\sin\theta} h'_{\nu}(kr) \sin(m\phi) \quad (3.10)$$

$$H_r = 0 \quad (3.11)$$

$$H_{\theta} = - \frac{mA_{mv}}{r} \frac{P_{\nu}^m(\cos\theta)}{\sin\theta} h_{\nu}(kr) \sin(m\phi) \quad (3.12)$$

$$H_{\phi} = - \frac{A_{mv}}{r} \frac{dP_{\nu}^m(\cos\theta)}{d\theta} h_{\nu}(kr) \cos(m\phi) \quad (3.13)$$

In the above equations the prime denotes the derivative of the Ricatti-Hankel function with respect to its argument. To satisfy the boundary conditions  $E_r = E_{\phi} = 0$  at  $\theta = \theta_e$ , the parameter  $\nu$  must satisfy the characteristic equation

$$P_{\nu}^m(\cos\theta_e) = 0 \quad (3.14)$$

The appropriate choice of the vector potential for TE to  $r$  mode functions is as follows:

$$F_r = B_{mv} P_{\nu}^m(\cos\theta) h_{\nu}(kr) \sin(m\phi) \quad (3.15)$$

With this choice, the field components are then given by the following set of equations for TE modes,

$$E_r = 0 \quad (3.16)$$

$$E_{\theta} = - \frac{mB_{mv}}{r} \frac{P_{\nu}^m(\cos\theta)}{\sin\theta} h_{\nu}(kr) \cos(m\phi) \quad (3.17)$$

$$E_{\phi} = \frac{B_{mv}}{r} \frac{dP_{\nu}^m(\cos\theta)}{d\theta} h_{\nu}(kr) \sin(m\phi) \quad (3.18)$$

$$H_r = \frac{B_{mv}}{j\omega\mu} \frac{\nu(\nu+1)}{r^2} P_{\nu}^m(\cos\theta) h_{\nu}(kr) \sin(m\phi) \quad (3.19)$$

$$H_{\theta} = \frac{B_{mv}}{j\omega\mu} \frac{k}{r} \frac{dP_{\nu}^m(\cos\theta)}{d\theta} h'_{\nu}(kr) \sin(m\phi) \quad (3.20)$$

$$H_{\phi} = \frac{B_{mv}}{j\omega\mu} \frac{mk}{r} \frac{P_{\nu}^m(\cos\theta)}{\sin\theta} h'_{\nu}(kr) \cos(m\phi) \quad (3.21)$$

The boundary condition  $E_{\phi} = 0$  at  $\theta = \theta_e$  requires that the parameter  $\nu$  must be a solution of the characteristic equation

$$[d P_{\nu}^m(\cos\theta)/d\theta]_{\theta=\theta_e} = 0 \quad (3.22)$$

The solutions for the characteristic equations (3.14) and (3.22) can be obtained by using the bisection method [Pennington, 1970] along with the hypergeometric expansion of the associated Legendre polynomial [Gradshteyn and Ryzhik, 1965, pp.1007]. Recently, the integral representation of the associated Legendre polynomials has been used to obtain the solutions of the characteristic equations [Narasimhan and Balasubramanya, 1974]. This technique provides good results for the eigenvalues with zero and unity azimuthal dependence. However, the computer program written to evaluate the eigenvalues using an integral representation can not be generalized for any value of  $m$  due to different integrands.

The first four roots of the characteristic equations are plotted in Figures 3.2 and 3.3 as a function of the cone flare angle for  $m = 0$  and  $m = 1$ , respectively. The subscript  $m$  and  $n$ , used to identify the

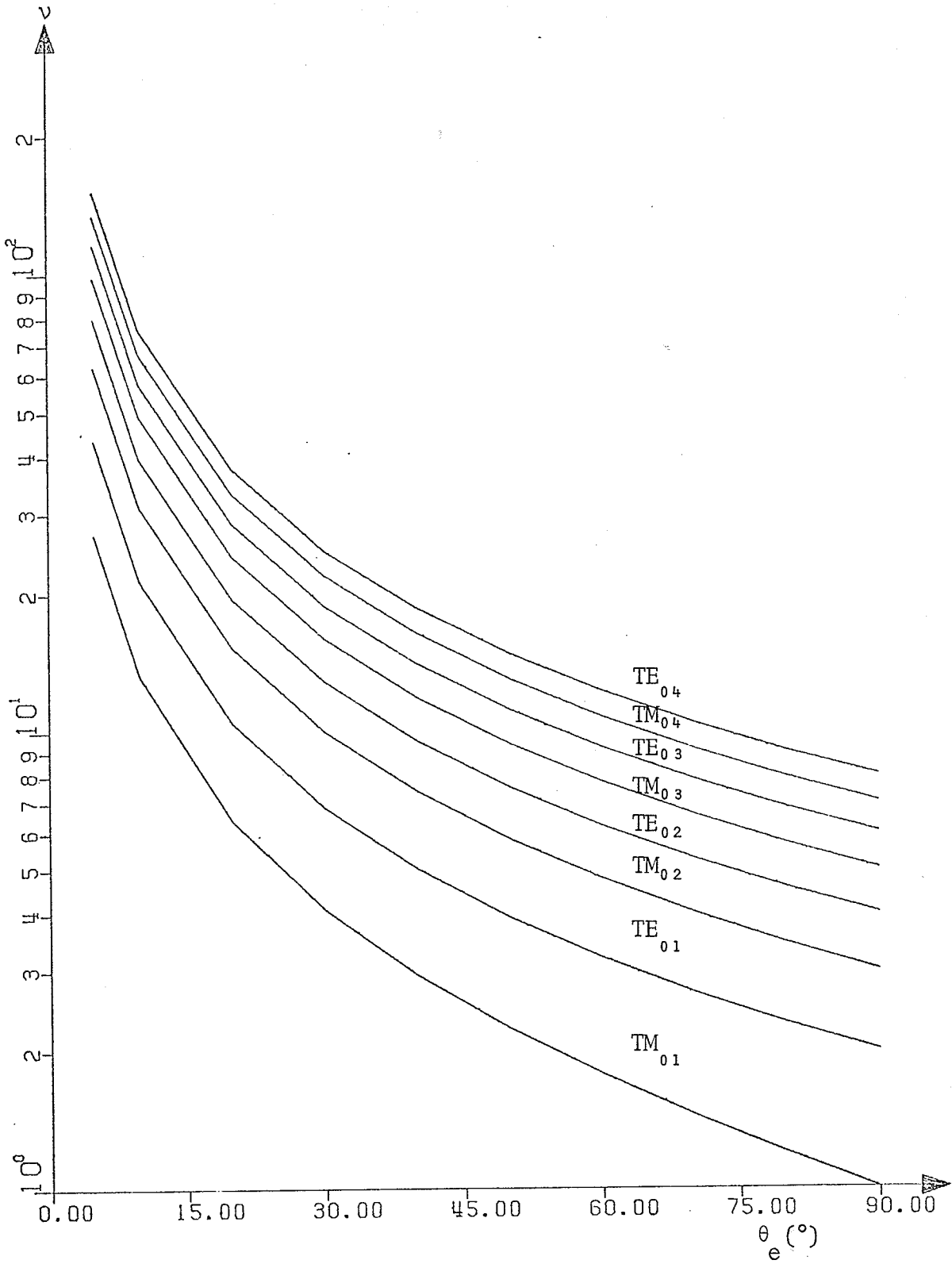


Fig. 3.2 Roots of the characteristic equation of a conical horn for  $m = 0$

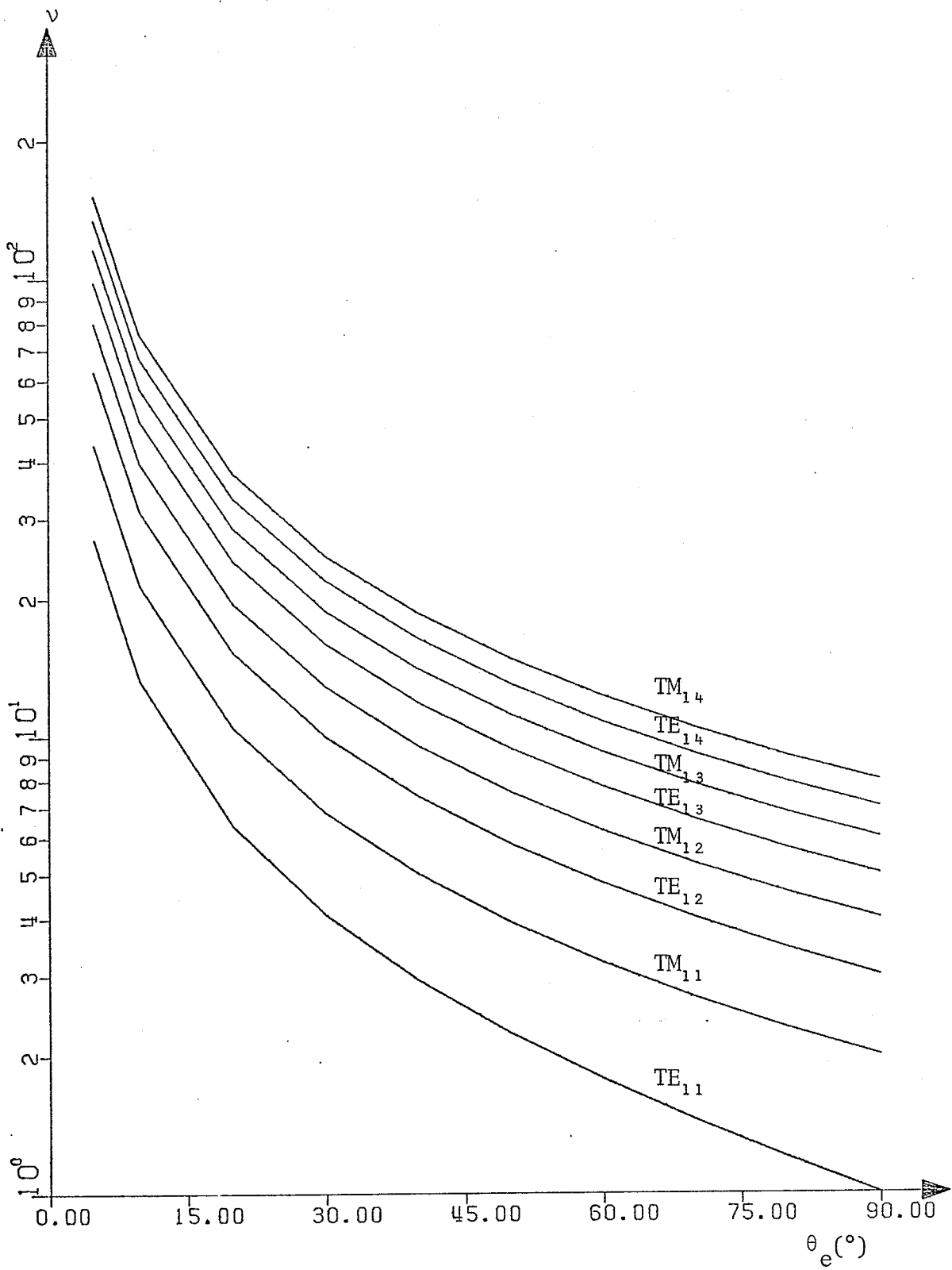


Fig. 3.3 Roots of the characteristic equation of a conical horn for  $m = 1$

modes, are respectively the azimuthal dependence and the order of the root of the characteristic equations for increasing values of  $\nu$ ,

For the purpose of computation, it is convenient to use a slightly modified form of the transverse aperture fields over a spherical cap of  $r = a$ . Dropping the amplitude constant, the time dependence  $e^{j\omega t}$  and considering only the outgoing wave, the transverse aperture fields for TM to  $r$  modes are given at  $r = a$  as:

$$E_{\theta} = \frac{dP_{\nu}^m(\text{Cos}\theta)}{d\theta} \text{Cos}(m\phi) \quad (3.23)$$

$$E_{\phi} = -m \frac{P_{\nu}^m(\text{Cos}\theta)}{\text{Sin}\theta} \text{Sin}(m\phi) \quad (3.24)$$

$$H_{\theta} = -\frac{j\omega\epsilon}{R_{\nu}(ka)} m \frac{P_{\nu}^m(\text{Cos}\theta)}{\text{Sin}\theta} \text{Sin}(m\phi) \quad (3.25)$$

$$H_{\phi} = -\frac{j\omega\epsilon}{R_{\nu}(ka)} m \frac{dP_{\nu}^m(\text{Cos}\theta)}{d\theta} \text{Cos}(m\phi) \quad (3.26)$$

where

$$R_{\nu}(ka) = k h'_{\nu}(ka)/h_{\nu}(ka) \quad (3.27)$$

Similarly, the transverse aperture fields for TE to  $r$  modes are given at  $r = a$  as:

$$E_{\theta} = -m \frac{P_{\nu}^m(\text{Cos}\theta)}{\text{Sin}\theta} \text{Cos}(m\phi) \quad (3.28)$$

$$E_{\phi} = \frac{dP_{\nu}^m(\text{Cos}\theta)}{d\theta} \text{Sin}(m\phi) \quad (3.29)$$

$$H_{\theta} = \frac{R_{\nu}(ka)}{j\omega\mu} \frac{dP_{\nu}^m(\cos\theta)}{d\theta} \sin(m\phi) \quad (3.30)$$

$$H_{\phi} = \frac{R_{\nu}(ka)}{j\omega\mu} m \frac{P_{\nu}^m(\cos\theta)}{\sin\theta} \cos(m\phi) \quad (3.31)$$

The amplitudes of the  $TE_{11}$ ,  $TM_{11}$ ,  $TE_{12}$  and  $TM_{12}$  transversal fields in the E- and H- plane of a fabricated horn with flare angle  $9.5^{\circ}$  are shown in Figures 3.4 and 3.5. These amplitudes are normalized to provide the same gain of the far field radiation pattern. The actual amplitudes of these modes depend upon the throat design and the cone length [Schorr and Beck, 1950].

### 3.2.2 Theoretical and Experimental Radiation Patterns

Now that the aperture fields of the conical horn are known, the radiation field  $\bar{E}_s$  may be determined by Kirchhoff-Huygen's integration over the aperture area. The radiation field  $\bar{E}_s$  at the observation point with coordinates  $(r', \theta', \phi')$  is given by [Silver, 1949, pp.161].

$$\bar{E}_s(\theta', \phi') = - \frac{jk \exp(-jkr')}{4\pi r'} \bar{a}_{r'} \times \int_A [\bar{n} \times \bar{E}_i - (\mu/\epsilon)^{1/2} \bar{a}_{r'} \times (\bar{n} \times \bar{H}_i)] \exp(jk\bar{r} \cdot \bar{a}_{r'}) dA \quad (3.32)$$

where as indicated in Fig. 3.1,

$\bar{r}$  is the vector from the origin to the element of the aperture;

$\bar{a}_{r'}$  is the unit vector from the origin to the observation point;

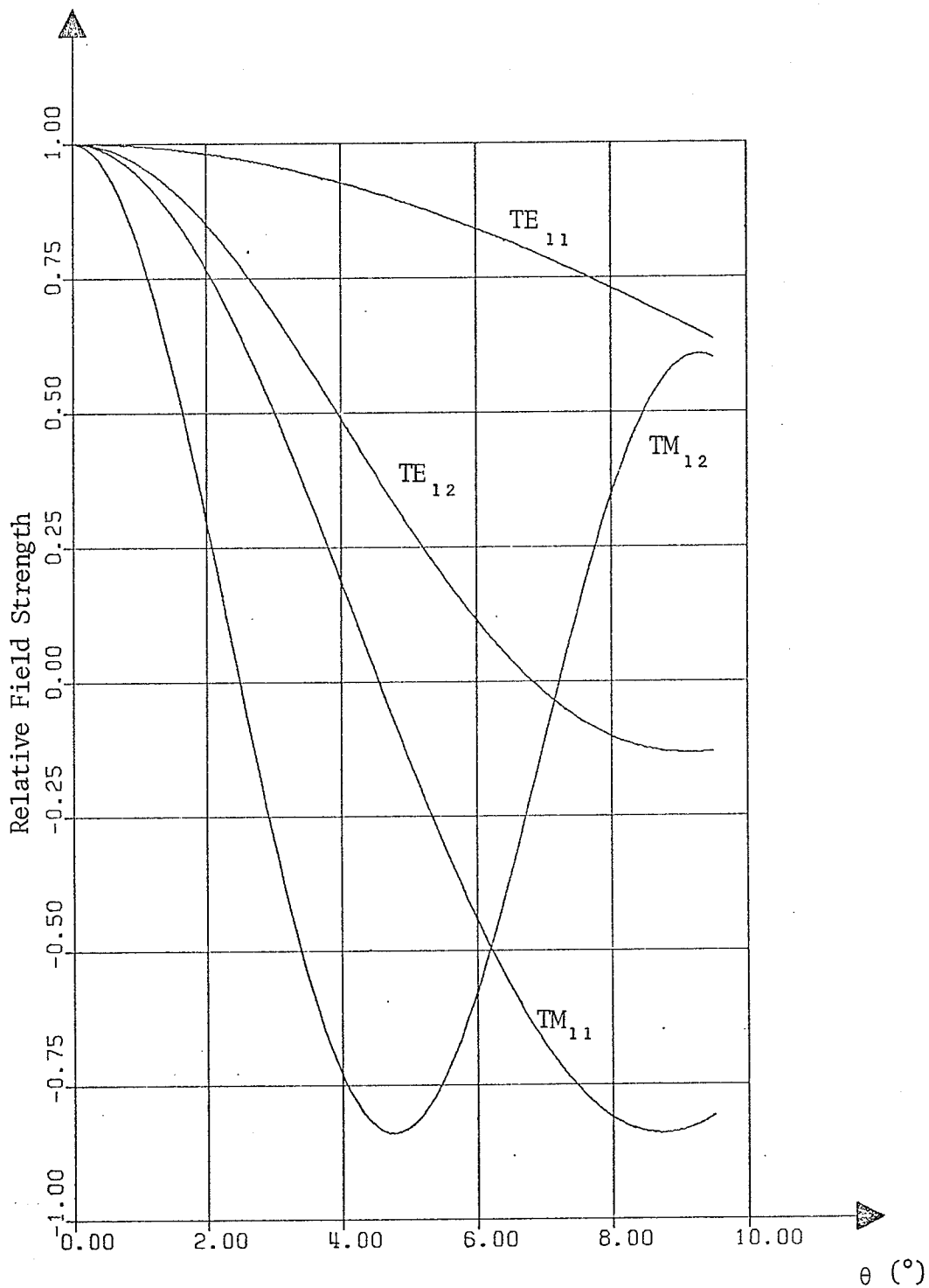


Fig. 3.4 E-plane aperture amplitude distributions for various modes in a conical horn antenna with  $\theta_e = 9.5^\circ$ . The different distributions are normalized to yield the same fields on boresight. E-plane refers to  $E_\theta$  pattern for  $\phi = 0$ .

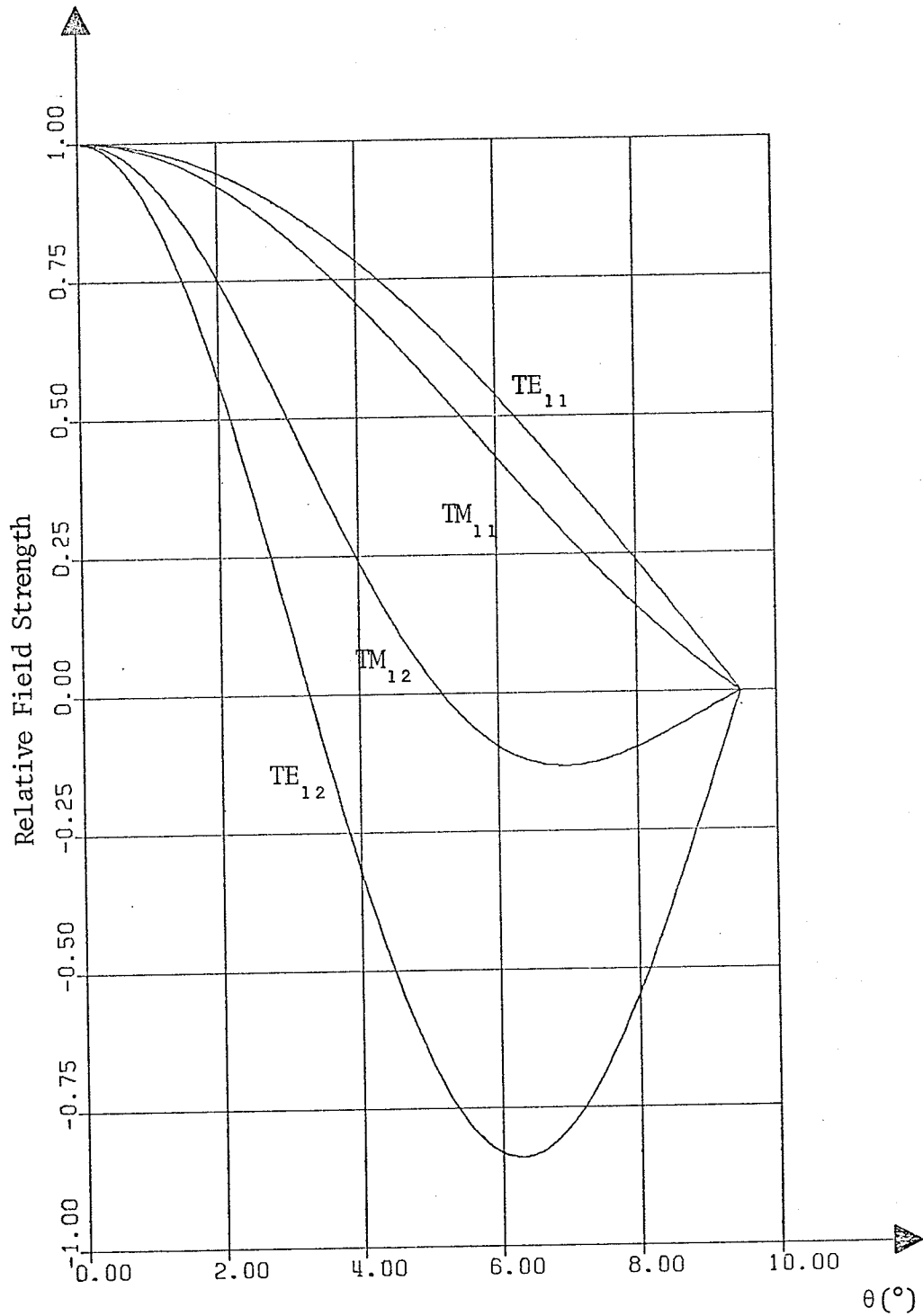


Fig. 3.5 H-plane aperture amplitude distributions for various modes in a conical horn antenna with  $\theta_e = 9.5^\circ$ . The different distributions are normalized to yield the same fields on boresight. H-plane refers to  $E_\phi$  pattern for  $\phi = 90^\circ$ .

$\bar{n}$  is the unit vector normal to the aperture;  
and  $\bar{E}_i, \bar{H}_i$  are the aperture fields.

Substituting for the different vectors and after some simple algebraic manipulations, the radiation field components are found to be

$$\begin{aligned}
 E_{S\theta}, (\theta', \phi') = & - \frac{jk \exp(-jkr')}{4\pi r'} \int_0^{\theta} e^{\int_0^{2\pi}} [-E_{\theta} \cos(\phi - \phi') + E_{\phi} \cos\theta \\
 & \sin(\phi - \phi') - (\mu/\epsilon)^{1/2} H_{\theta} \cos\theta' \sin(\phi - \phi') \\
 & - (\mu/\epsilon)^{1/2} H_{\phi} \{\cos\theta \cos\theta' \cos(\phi - \phi') + \sin\theta \sin\theta'\}] \\
 & \exp[j\alpha + j\psi \cos(\phi - \phi')] a^2 \sin\theta \, d\theta \, d\phi \quad (3.33)
 \end{aligned}$$

and

$$\begin{aligned}
 E_{S\phi}, (\theta', \phi') = & - \frac{jk \exp(-jkr')}{4\pi r'} \int_0^{\theta} e^{\int_0^{2\pi}} [-E_{\theta} \cos\theta' \sin(\phi - \phi') \\
 & - E_{\phi} \{\cos\theta \cos\theta' \cos(\phi - \phi') + \sin\theta \sin\theta'\}] \\
 & + (\mu/\epsilon)^{1/2} H_{\theta} \cos(\phi - \phi') - (\mu/\epsilon)^{1/2} H_{\phi} \cos\theta \sin(\phi - \phi')] \\
 & \exp [j\alpha + j\psi \cos(\phi - \phi')] a^2 \sin\theta \, d\theta \, d\phi \quad (3.34)
 \end{aligned}$$

where

$$\alpha = ka \cos\theta \cos\theta' \quad (3.35)$$

$$\text{and } \psi = ka \sin\theta \sin\theta' \quad (3.36)$$

The numerical evaluation of the above integrals can be considerably simplified by substituting the closed form expression for the  $\phi$  integration. This is due to the representation of  $\exp[j\psi \cos(\phi - \phi')]$  in terms of Bessel functions [Harrington, 1961, pp.230]. Performing the  $\phi$  integration with the aperture field components from equations (3.23) -

(3.31), the radiation field components are reduced to the following equations.

$$\begin{aligned}
 E_{S\theta'}^{TE}(\theta', \phi') = & -C \cos(m\phi') \int_0^\theta e^{j\alpha \cos\theta} [m\xi \frac{P_v^m(\cos\theta)}{\sin\theta} \{1 - \frac{R_v(ka)}{jk}\} \\
 & \cos\theta \cos\theta'\} + \delta \frac{dP_v^m(\cos\theta)}{d\theta} \{\cos\theta - \frac{R_v(ka)}{jk} \cos\theta'\} \\
 & - 2 \frac{R_v(ka)}{k} m P_v^m(\cos\theta) \sin\theta' J_m(\psi)] \exp(j\alpha) \sin\theta \, d\theta \quad (3.37)
 \end{aligned}$$

$$\begin{aligned}
 E_{S\phi'}^{TE}(\theta', \phi') = & -C \sin(m\phi') \int_0^\theta e^{j\alpha \cos\theta} [-m\delta \frac{P_v^m(\cos\theta)}{\sin\theta} \{\cos\theta' \\
 & - \frac{R_v(ka)}{jk} \cos\theta\} - \xi \frac{dP_v^m(\cos\theta)}{d\theta} \{\cos\theta \cos\theta' - \frac{R_v(ka)}{jk}\} \\
 & - 2j \sin\theta \sin\theta' J_m(\psi) \frac{dP_v^m(\cos\theta)}{d\theta}] \exp(j\alpha) \sin\theta \, d\theta \quad (3.38)
 \end{aligned}$$

$$\begin{aligned}
 E_{S\theta'}^{TM}(\theta', \phi') = & -C' \cos(m\phi') \int_0^\theta e^{j\alpha \cos\theta} [\xi \frac{dP_v^m(\cos\theta)}{d\theta} \{\cos\theta \cos\theta' \\
 & - \frac{R_v(ka)}{jk}\} + m\delta \frac{P_v^m(\cos\theta)}{\sin\theta} \{\cos\theta' - \frac{R_v(ka)}{jk} \cos\theta\} \\
 & + 2j \sin\theta \sin\theta' J_m(\psi) \frac{dP_v^m(\cos\theta)}{d\theta}] \exp(j\alpha) \sin\theta \, d\theta \quad (3.39)
 \end{aligned}$$

$$\begin{aligned}
 E_{S\phi'}^{TM}(\theta', \phi') = & -C' \sin(m\phi') \int_0^\theta e^{j\alpha \cos\theta} [\delta \frac{dP_v^m(\cos\theta)}{d\theta} \{ \frac{R_v(ka)}{jk} \cos\theta' \\
 & - \cos\theta\} + m\xi \frac{P_v^m(\cos\theta)}{\sin\theta} \{ \frac{R_v(ka)}{jk} \cos\theta \cos\theta' - 1\} \\
 & + 2jm P_v^m(\cos\theta) \sin\theta' J_m(\psi)] \exp(j\alpha) \sin\theta \, d\theta \quad (3.40)
 \end{aligned}$$

where

$$C = j^m \frac{ka}{4r}, B_{mv} h_v(ka) \exp(-jkr') \quad (3.41)$$

$$C' = j^m \frac{ka}{4r}, A_{mv} h_v(ka) \exp(-jkr') \quad (3.42)$$

$$\xi = J_{m-1}(\psi) - J_{m+1}(\psi) \quad (3.43)$$

$$\delta = J_{m-1}(\psi) + J_{m+1}(\psi) \quad (3.44)$$

and  $J_m(\psi)$  is the cylindrical Bessel function of order  $m$  and argument  $\psi$ .

The above equations are utilized to obtain the radiation patterns of the fabricated conical horn of flare angle  $9.5^\circ$  at two frequencies of 8.5 and 11 GHz. These radiation patterns along with the observed radiation patterns are plotted in Figures 3.6 and 3.7. In the theoretical pattern calculations, attention has been restricted to the dominant mode ( $TE_{11}$ ) in the conical horn. A good agreement of the observed and calculated radiation patterns is clearly indicated.

### 3.3 DIELECTRIC CONE ANTENNA

A dielectric cone antenna consists of a dielectric cone fed by a horn antenna. For the circularly symmetric case, the launcher could either be a conical horn or a corrugated conical horn. Due to the expensive manufacturing of corrugated conical horn antenna [Clarricoats and Saha, 1971], the attention in the present work is restricted to a conical horn launcher.

The analysis of the dielectric cone antenna requires a knowledge of the appropriate modes in the dielectric cone. Very little theoretical and experimental work is available for determining the mode propagation [Salema, 1972] or scattering from a dielectric cone [Ruck et.al., 1970]. This, as shown in the following sections, is due to the excessive time

involved in the evaluation of the associated Legendre polynomials and the simultaneous solution of two transcendental characteristic equations obtained by matching the boundary conditions. Any attempt to obtain the solution involves an approximation to reduce the two characteristic equations into one and approximating the associated Legendre polynomials by an asymptotic expansion.

A similarity between the corrugated feed and optical waveguide as shown by Clarricoats (1970) has been used by Salema (1972) to develop an approximate solution for the dielectric cone antenna. Since a better solution is not available the same approximations will be used in the following sections. The eigenvalues thus determined are used to calculate the radiation patterns using vector Kirchhoff's integral formulation. The effect of adding higher order mode contributions to the radiated field and some experimental results are also discussed.

### 3.3.1 Characteristic Equation for a Dielectric Cone Antenna

Consider an infinite lossless cone of dielectric constant  $\epsilon_1$  immersed in a material of dielectric constant  $\epsilon_2$  (Fig. 3.8). The spherical coordinate system is chosen in such a way that the axis of the cone lies along the positive z-axis. The hybrid modes propagating inside the dielectric cone can be represented as a combination of TE to r and TM to r modes. The appropriate vector potentials for these modes are given as [Harrington, 1961]

$$A_r^{(1)} = A_{ms} h_s(k_1 r) P_s^m(\cos\theta) \cos(m\phi) \quad (3.45)$$

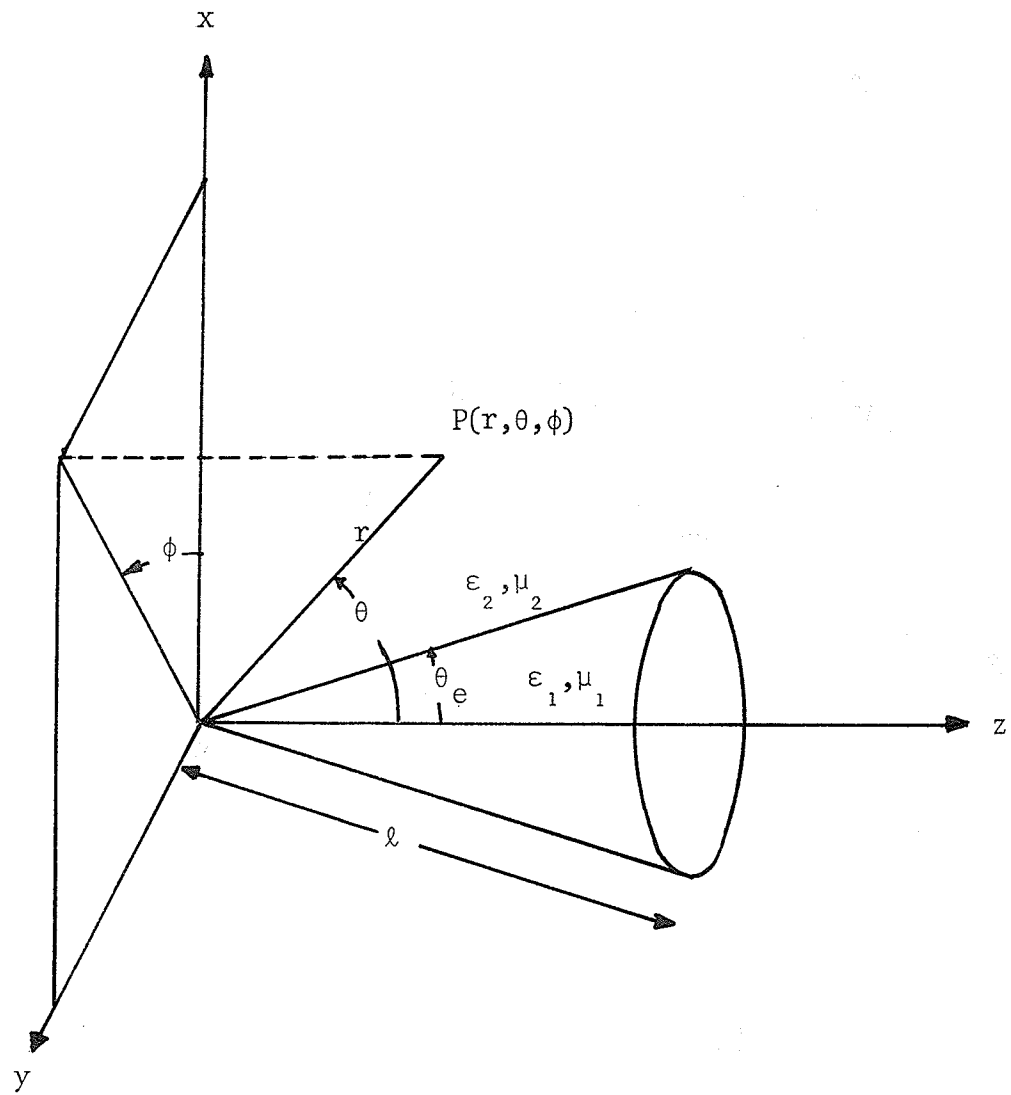


Fig. 3.8 Coordinate system for the dielectric cone antenna

$$F_r^{(1)} = B_{ms} h_s(k_1 r) P_s^m(\cos\theta) \sin(m\phi) \quad (3.46)$$

for modes inside the dielectric cone and

$$A_r^{(2)} = C_{mt} h_t(k_2 r) P_t^m(-\cos\theta) \cos(m\phi) \quad (3.47)$$

$$F_r^{(2)} = D_{mt} h_t(k_2 r) P_t^m(-\cos\theta) \sin(m\phi) \quad (3.48)$$

for modes in the region outside the dielectric cone. In the above equations

$$k_1^2 = \omega^2 \epsilon_1 \mu_1 \quad (3.49)$$

$$k_2^2 = \omega^2 \epsilon_2 \mu_2 \quad (3.50)$$

and

$P_s^m(\cos\theta)$ ,  $P_t^m(-\cos\theta)$  are the associated Legendre functions of first kind;

$h_s(k_1 r)$ ,  $h_t(k_2 r)$  are the spherical Riccati-Hankel functions of second kind for a time dependence of  $e^{j\omega t}$ , and satisfy the differential equations

$$\left( \frac{d^2}{dr^2} + k_1^2 - \frac{s(s+1)}{r^2} \right) h_s(k_1 r) = 0 \quad (3.51)$$

and

$$\left( \frac{d^2}{dr^2} + k_2^2 - \frac{t(t+1)}{r^2} \right) h_t(k_2 r) = 0 \quad (3.52)$$

It should be noted that  $P_s^m(\cos\theta)$  and  $P_t^m(-\cos\theta)$  are two linearly independent solutions of the differential equations for the associated Legendre polynomials [Gradshteyn and Ryzhik, 1965] and for the fields to be decaying outside the cone,  $t$  should be taken as  $-1/2 + jt'$ .

Substituting the electric and magnetic vector potentials of equations (3.45) - (3.48) in equations (3.1) - (3.6) gives the field components in the two regions as

$$E_r^{(1)} = A_{ms} \frac{s(s+1)}{j\omega\epsilon_1 r^2} h_s(k_1 r) P_s^m(\cos\theta) \cos(m\phi) \quad (3.53)$$

$$E_\theta^{(1)} = A_{ms} \frac{h_s(k_1 r)}{r} \left[ \frac{R_s(k_1 r)}{j\omega\epsilon_1} \frac{dP_s^m(\cos\theta)}{d\theta} - \frac{m B_{ms}}{A_{ms}} \frac{P_s^m(\cos\theta)}{\sin\theta} \right] \sin(m\phi) \quad (3.54)$$

$$E_\phi^{(1)} = A_{ms} \frac{h_s(k_1 r)}{r} \left[ - \frac{R_s(k_1 r)}{j\omega\epsilon_1} \frac{P_s^m(\cos\theta)}{\sin\theta} + \frac{B_{ms}}{A_{ms}} \frac{dP_s^m(\cos\theta)}{d\theta} \right] \sin(m\phi) \quad (3.55)$$

$$H_r^{(1)} = B_{ms} \frac{s(s+1)}{j\omega\mu_1 r^2} h_s(k_1 r) P_s^m(\cos\theta) \sin(m\phi) \quad (3.56)$$

$$H_\theta^{(1)} = A_{ms} \frac{h_s(k_1 r)}{r} \left[ - m \frac{P_s^m(\cos\theta)}{\sin\theta} + \frac{B_{ms}}{A_{ms}} \frac{R_s(k_1 r)}{j\omega\mu_1} \frac{dP_s^m(\cos\theta)}{d\theta} \right] \sin(m\phi) \quad (3.57)$$

$$H_\phi^{(1)} = A_{ms} \frac{h_s(k_1 r)}{r} \left[ - \frac{dP_s^m(\cos\theta)}{d\theta} + m \frac{B_{ms}}{A_{ms}} \frac{R_s(k_1 r)}{j\omega\mu_1} \frac{P_s^m(\cos\theta)}{\sin\theta} \right] \cos(m\phi) \quad (3.58)$$

$$E_r^{(2)} = C_{mt} \frac{t(t+1)}{j\omega\epsilon_2 r^2} h_t(k_2 r) P_t^m(-\cos\theta) \cos(m\phi) \quad (3.59)$$

$$E_{\theta}^{(2)} = C_{mt} \frac{h_t(k_2 r)}{r} \left[ \frac{R_t(k_2 r)}{j\omega\epsilon_2} \frac{dP_t^m(-\cos\theta)}{d\theta} - m \frac{D_{mt}}{C_{mt}} \frac{P_t^m(-\cos\theta)}{\sin\theta} \right] \cos(m\phi) \quad (3.60)$$

$$E_{\phi}^{(2)} = C_{mt} \frac{h_t(k_2 r)}{r} \left[ -m \frac{R_t(k_2 r)}{j\omega\epsilon_2} \frac{P_t^m(-\cos\theta)}{\sin\theta} + \frac{D_{mt}}{C_{mt}} \frac{dP_t^m(-\cos\theta)}{d\theta} \right] \sin(m\phi) \quad (3.61)$$

$$H_r^{(2)} = D_{mt} \frac{t(t+1)}{j\omega\mu_2 r^2} h_t(k_2 r) P_t^m(-\cos\theta) \sin(m\phi) \quad (3.62)$$

$$H_{\theta}^{(2)} = C_{mt} \frac{h_t(k_2 r)}{r} \left[ -m \frac{P_t^m(-\cos\theta)}{\sin\theta} + \frac{D_{mt}}{C_{mt}} \frac{R_t(k_2 r)}{j\omega\mu_2} \frac{dP_t^m(-\cos\theta)}{d\theta} \right] \sin(m\phi) \quad (3.63)$$

$$H_{\phi}^{(2)} = C_{mt} \frac{h_t(k_2 r)}{r} \left[ -\frac{dP_t^m(-\cos\theta)}{d\theta} + m \frac{D_{mt}}{C_{mt}} \frac{R_t(k_2 r)}{j\omega\mu_2} \frac{P_t^m(-\cos\theta)}{\sin\theta} \right] \cos(m\phi) \quad (3.64)$$

where

$$R_s(k_1 r) = k_1 h'_s(k_1 r)/h_s(k_1 r) \quad (3.65)$$

and

$$R_t(k_2 r) = k_2 h'_t(k_2 r)/h_t(k_2 r) \quad (3.66)$$

The continuity of tangential  $E_r$  and  $H_r$  at  $\theta = \theta_e$  gives, respectively

$$A_{ms} = C_{mt} \frac{\epsilon_1}{\epsilon_2} \frac{t(t+1)}{s(s+1)} \frac{P_t^m(-\cos\theta_e)}{P_s^m(\cos\theta_e)} \frac{h_t(k_2 r)}{h_s(k_1 r)} \quad (3.67)$$

$$B_{ms} = D_{mt} \frac{\mu_1}{\mu_2} \frac{t(t+1)}{s(s+1)} \frac{P_t^m(-\cos\theta_e)}{P_s^m(\cos\theta_e)} \frac{h_t(k_2 r)}{h_s(k_1 r)} \quad (3.68)$$

The continuity of tangential  $E_\phi$  and  $H_\phi$  along with equations (3.67) and (3.68) leads to

$$\frac{C_{mt}}{D_{mt}} = \frac{j\omega\epsilon_2}{m} \frac{\frac{\mu_1}{\mu_2} \frac{t(t+1)}{s(s+1)} P_{sm}(\theta_e) - P_{tm}(\theta_e)}{[R_s(k_1 r) \frac{t(t+1)}{s(s+1)} - R_t(k_2 r)]} \quad (3.69)$$

and

$$\frac{C_{mt}}{D_{mt}} = \frac{m}{j\omega\mu_2} \frac{R_s(k_1 r) \frac{t(t+1)}{s(s+1)} - R_t(k_2 r)}{\frac{\epsilon_1}{\epsilon_2} \frac{t(t+1)}{s(s+1)} P_{sm}(\theta_e) - P_{tm}(\theta_e)} \quad (3.70)$$

respectively, where

$$P_{sm}(\theta_e) = \frac{\sin\theta_e}{P_s^m(\cos\theta_e)} \left( \frac{dP_s^m(\cos\theta)}{d\theta} \right)_{\theta=\theta_e} \quad (3.71)$$

$$P_{tm}(\theta_e) = \frac{\sin\theta_e}{P_t^m(-\cos\theta_e)} \left( \frac{dP_t^m(-\cos\theta)}{d\theta} \right)_{\theta=\theta_e} \quad (3.72)$$

Equating equations (3.69) and (3.70) gives the first characteristic equation, namely

$$\left[ \frac{\epsilon_1}{\epsilon_2} \frac{t(t+1)}{s(s+1)} P_{sm}(\theta_e) - P_{tm}(\theta_e) \right] \left[ \frac{\mu_1}{\mu_2} \frac{t(t+1)}{s(s+1)} P_{sm}(\theta_e) - P_{tm}(\theta_e) \right] + \frac{m^2}{\omega^2 \epsilon_2 \mu_2} [R_s(k_1 r) \frac{t(t+1)}{s(s+1)} - R_t(k_2 r)]^2 = 0 \quad (3.73)$$

and similarly the continuity of  $\epsilon E_\theta$  and  $\mu H_\theta$  leads to the second characteristic equation

$$\left[ R_s(k_1 r) \frac{\epsilon_1}{\epsilon_2} \frac{t(t+1)}{s(s+1)} P_{sm}(\theta_e) - R_t(k_2 r) P_{tm}(\theta_e) \right] \left[ R_s(k_1 r) \frac{\mu_1}{\mu_2} \frac{t(t+1)}{s(s+1)} P_{sm}(\theta_e) - R_t(k_2 r) P_{tm}(\theta_e) \right] + m^2 \omega^2 \epsilon_2 \mu_2 \left[ 1 - \frac{\epsilon_1 \mu_1}{\epsilon_2 \mu_2} \frac{t(t+1)}{s(s+1)} \right] = 0 \quad (3.74)$$

Equations (3.73) and (3.74) need to be solved simultaneously, for any large  $r$ , to obtain the values of  $s$  and  $t$  and no exact method is known in the literature to accomplish this task. Most of the available methods [Zaguskin, 1961] either fail to converge or have very slow convergence. The selection of proper roots becomes more complicated due to the involvement of the functions  $P_s^m(\cos \theta)$  and  $P_t^m(-\cos \theta)$ , both of which have infinite zeros.

The above two characteristic equations can be reduced to one equation by enforcing a solution such that

$$k_C^2 = \omega^2 \epsilon_1 \mu_1 - \frac{s(s+1)}{r^2} \quad (3.75)$$

and

$$k_C^2 = \omega^2 \epsilon_2 \mu_2 - \frac{t(t+1)}{r^2} \quad (3.76)$$

The above assumption of making one propagation constant ( $k_c$ ) to be valid inside and outside the cone provides a satisfactory agreement, as shown below, with the experimentally observed patterns. This assumption appears to hold good for cone lengths with  $k_2 r \gg 1$ . For small cone lengths, the dielectric cone has to be divided into an infinite set of sheets of infinitesimal thickness  $dr$ , for which the solution is exact, and one would have to derive a general expression for the coupling between the adjacent sections [Salema, 1972]. This approach is not attempted here since the cone lengths considered satisfy the condition  $k_2 r \gg 1$ .

It can be easily shown that equations (3.75) and (3.76) after some manipulations give

$$1 - \frac{\epsilon_1 \mu_1}{\epsilon_2 \mu_2} \frac{s(s+1)}{t(t+1)} = \frac{k_c^2}{\omega^2 \epsilon_2 \mu_2} \left[ 1 - \frac{t(t+1)}{s(s+1)} \right] \quad (3.77)$$

The approximations given by equations (3.75) and (3.76) when substituted in equations (3.65) and (3.66) give

$$R_s(k_1 r) \rightarrow -j k_c \quad (3.78)$$

$$R_t(k_2 r) \rightarrow -j k_c \quad (3.79)$$

Using equations (3.77) - (3.79) in equation (3.74) gives the characteristic equation for the dielectric cone as

$$\begin{aligned}
& \left[ \frac{\epsilon_1}{\epsilon_2} \frac{t(t+1)}{s(s+1)} P_{sm}(\theta_e) - P_{tm}(\theta_e) \right] \left[ \frac{\mu_1}{\mu_2} \frac{t(t+1)}{s(s+1)} P_{sm}(\theta_e) - P_{tm}(\theta_e) \right] \\
& = \frac{m^2 k_C^2}{\omega^2 \epsilon_2 \mu_2} \left[ 1 - \frac{t(t+1)}{s(s+1)} \right] \quad (3.80)
\end{aligned}$$

The solution of the above equation to obtain the eigenvalues,  $s$ , requires the computation of associated Legendre functions. The numerical evaluation of the associated Legendre function with negative argument, to calculate  $P_{tm}(\theta_e)$ , has very slow convergence particularly for small cone angles due to the logarithmic singularity at  $\theta_e = 0^\circ$ . This difficulty can be circumvented by using the asymptotic expansion [Salema, 1972]

$$\lim_{\theta_e \rightarrow 0} P_t^m(-\cos\theta_e) \cong A K_m(\sqrt{-t(t+1)} \tan\theta_e) \quad (3.81)$$

where  $K_m$  is the modified Bessel function of the second kind. With this approximation the parameter  $P_{tm}(\theta_e)$  is given by

$$P_{tm}(\theta_e) \cong \sqrt{-t(t+1)} \frac{\tan\theta_e K'_m(\sqrt{-t(t+1)} \tan\theta_e)}{\cos\theta_e K_m(\sqrt{-t(t+1)} \tan\theta_e)} \quad (3.82)$$

It should be noted that the difference in eigenvalues due to this approximation was found to be in the fourth significant digit from the exact value. Therefore, this approximation should not result in any significant change of either the aperture field distribution or the radiation pattern.

It is interesting to note that the approximations given by equations (3.75) and (3.76) make the eigenvalues of the dielectric cone as a function of the cone length. The eigenvalues  $s$  are now functions of dielectric constant, relative permeability, cone angle and cone length. However, as shown in Figures 3.9 and 3.10 the variation in the eigenvalues with the change in cone lengths is not very significant. Therefore, the error in making these approximations is probably small particularly for large dielectric constants of the cone material (Fig.3.10).

### 3.3.2 Aperture Field Distribution

The characteristic equation, derived in the preceding section, is used to find the eigenvalue  $s$  for a particular mode inside the dielectric cone. The value of  $s$  is a function of the material parameters i.e. dielectric constant and permeability as well as the cone angle and the cone length. Assuming that truncating the cone does not result in any change of mode behaviour, the aperture field components for a large cone, satisfying the condition  $k_c \ell \approx k_c \ell$ , can be written as

$$E_r^{(1)} = A_{ms} \frac{s(s+1)}{j\omega\epsilon_1 \ell^2} h_s(k_c \ell) P_s^m(\cos\theta) \cos(m\phi) \quad (3.83)$$

$$E_\theta^{(1)} = A_{ms} \frac{h_s(k_c \ell)}{\ell} \left[ -\frac{k_c}{\omega\epsilon_1} \frac{dP_s^m(\cos\theta)}{d\theta} - \frac{m^2 k_c}{\omega\epsilon_1} \times \frac{P_s^m(\cos\theta)}{\sin\theta} \right] \cos(m\phi) \quad (3.84)$$

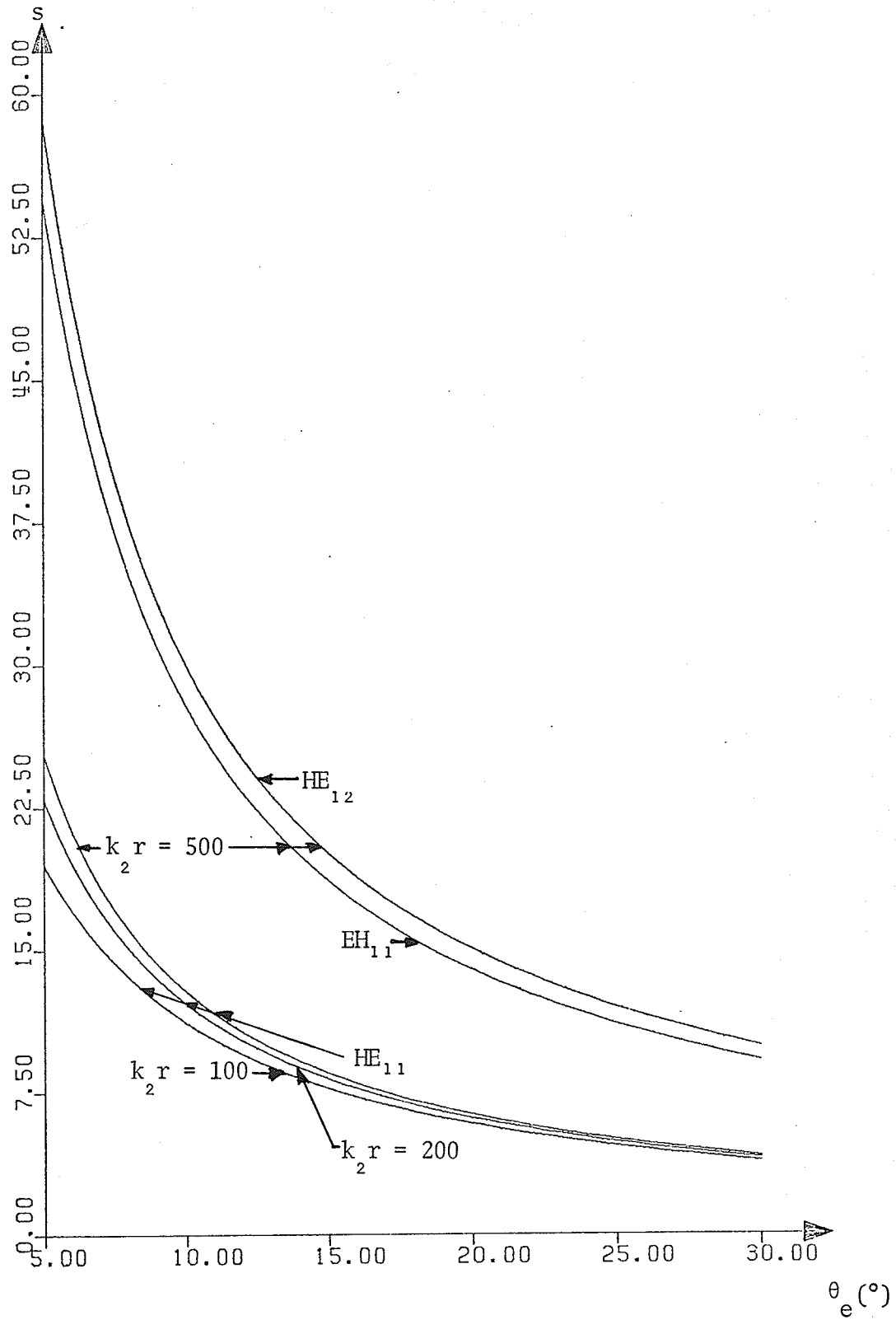


Fig. 3.9 Roots of the characteristic equation of the dielectric cone versus cone flare angle for  $\epsilon_r = 1.1$ .

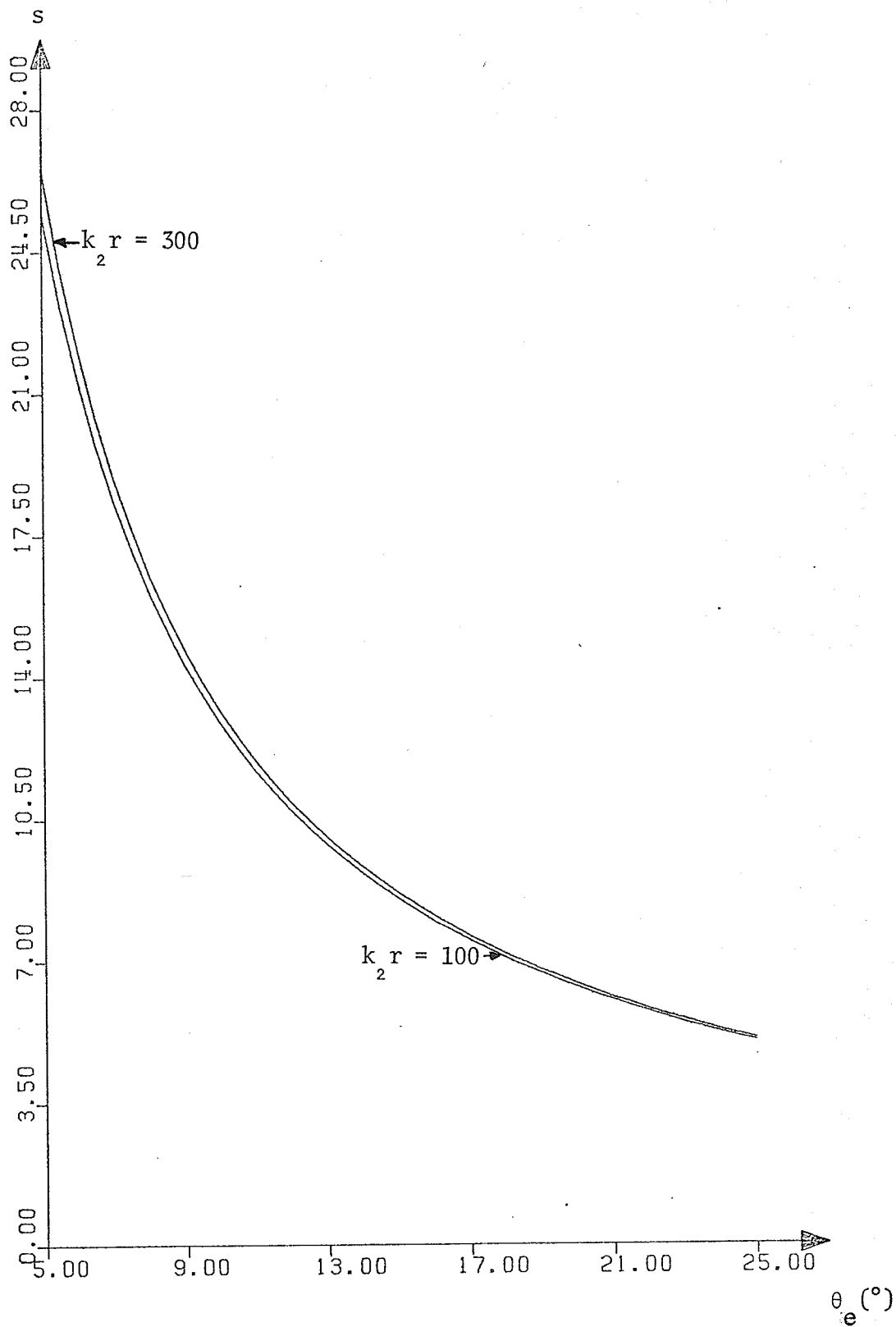


Fig. 3.10 Dominant roots of the characteristic equation of the dielectric cone versus cone flare angle for  $\epsilon_r = 2.5$ .

$$E_{\phi}^{(1)} = A_{ms} \frac{h_s(k_c \ell)}{\ell} \left[ \frac{m k_c}{\omega \epsilon_1} \frac{P_s^m(\cos \theta)}{\sin \theta} + \frac{m k_c}{\omega \epsilon_1} \chi \frac{dP_s^m(\cos \theta)}{d\theta} \right] \sin(m\phi) \quad (3.85)$$

$$H_r^{(1)} = A_{ms} \frac{m s(s+1) k_c}{\omega^2 \epsilon_1 \mu_1 \ell^2} \chi h_s(k_c \ell) P_s^m(\cos \theta) \sin(m\phi) \quad (3.86)$$

$$H_{\theta}^{(1)} = A_{ms} \frac{h_s(k_c \ell)}{\ell} \left[ -m \frac{P_s^m(\cos \theta)}{\sin \theta} - \frac{m k_c^2}{\omega^2 \epsilon_1 \mu_1} \chi \frac{dP_s^m(\cos \theta)}{d\theta} \right] \cos(m\phi) \quad (3.87)$$

$$H_{\phi}^{(1)} = A_{ms} \frac{h_s(k_c \ell)}{\ell} \left[ -\frac{dP_s^m(\cos \theta)}{d\theta} - \frac{m^2 k_c^2}{\omega^2 \epsilon_1 \mu_1} \chi \frac{P_s^m(\cos \theta)}{\sin \theta} \right] \sin(m\phi) \quad (3.88)$$

where

$$\chi = \frac{\mu_1}{\mu_2} \frac{1 - \frac{t(t+1)}{s(s+1)}}{\frac{\mu_1}{\mu_2} \frac{t(t+1)}{s(s+1)} P_{sm}(\theta_e) - P_{tm}(\theta_e)} \quad (3.89)$$

In writing the above equations, the constant  $B_{ms}$  has been substituted in terms of  $A_{ms}$  for which use has been made of equations (3.67) - (3.69), (3.78) and (3.79). For the purpose of computation, it is convenient to use a slightly modified form of the transverse aperture fields as

$$E_{\theta}^{(1)} = A_{ms} \frac{h_s(k_c \ell)}{\ell} E_{\theta c} \cos(m\phi) \quad (3.90)$$

$$E_{\phi}^{(1)} = A_{ms} \frac{h_s(k_c \ell)}{\ell} E_{\phi c} \sin(m\phi) \quad (3.91)$$

$$H_{\theta}^{(1)} = A_{ms} \frac{h_s(k_c \ell)}{\ell} H_{\theta c} \sin(m\phi) \quad (3.92)$$

$$H_{\phi}^{(1)} = A_{ms} \frac{h_s(k_c \ell)}{\ell} H_{\phi c} \cos(m\phi) \quad (3.93)$$

where

$$E_{\theta c} = -\frac{k_c}{\omega \epsilon_1} \frac{dP_s^m(\cos\theta)}{d\theta} - \frac{m^2 k_c}{\omega \epsilon_1} \chi \frac{P_s^m(\cos\theta)}{\sin\theta} \quad (3.94)$$

$$E_{\phi c} = \frac{m k_c}{\omega \epsilon_1} \frac{P_s^m(\cos\theta)}{\sin\theta} + \frac{m k_c}{\omega \epsilon_1} \chi \frac{dP_s^m(\cos\theta)}{d\theta} \quad (3.95)$$

$$H_{\theta c} = -m \frac{P_s^m(\cos\theta)}{\sin\theta} - m \frac{k_c^2}{\omega^2 \epsilon_1 \mu_1} \chi \frac{dP_s^m(\cos\theta)}{d\theta} \quad (3.96)$$

$$H_{\phi c} = -\frac{dP_s^m(\cos\theta)}{d\theta} - \frac{m^2 k_c^2}{\omega^2 \epsilon_1 \mu_1} \chi \frac{P_s^m(\cos\theta)}{\sin\theta} \quad (3.97)$$

The aperture fields for a dielectric cone with flare angle  $9.5^\circ$  and cone length  $\ell = 54.6246$  cms. are plotted in Figures 3.11 and 3.12. The dielectric constant used in these computations is 2.28. All amplitudes are normalized to provide the same gain of the far field radiation pattern. The actual amplitude of the individual modes depends upon the excitation efficiency of the mode under consideration.

### 3.3.3 Mode Excitation Efficiencies

A number of higher order cone modes, in addition to the dominant mode, are generated at the junction of the dielectric cone with the launcher. The excitation efficiencies of these modes depend upon the modes in the launcher, electrical lengths of the launcher and the dielectric cone, cone angles of the launcher and the dielectric cone as well as the dielectric constant of the cone material.

The excitation efficiency, defined as the ratio of the power

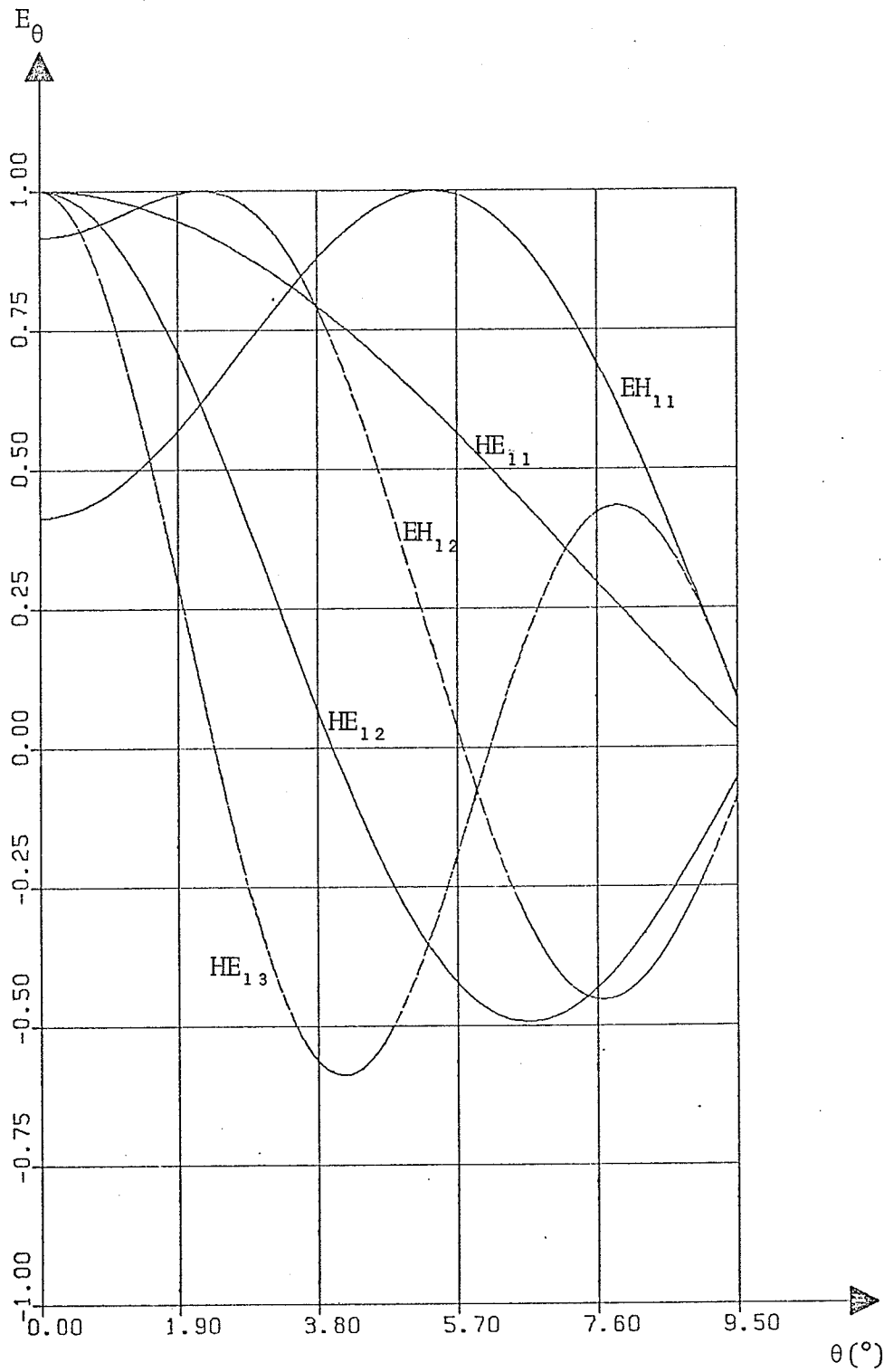


Fig. 3.11 Theoretical E-plane aperture amplitude distributions for first five modes of a dielectric cone with  $\theta_e = 9.5^\circ$ ,  $k_2 l = 97.2447$ ,  $\epsilon_r = 2.28$  and  $m = 1$ .

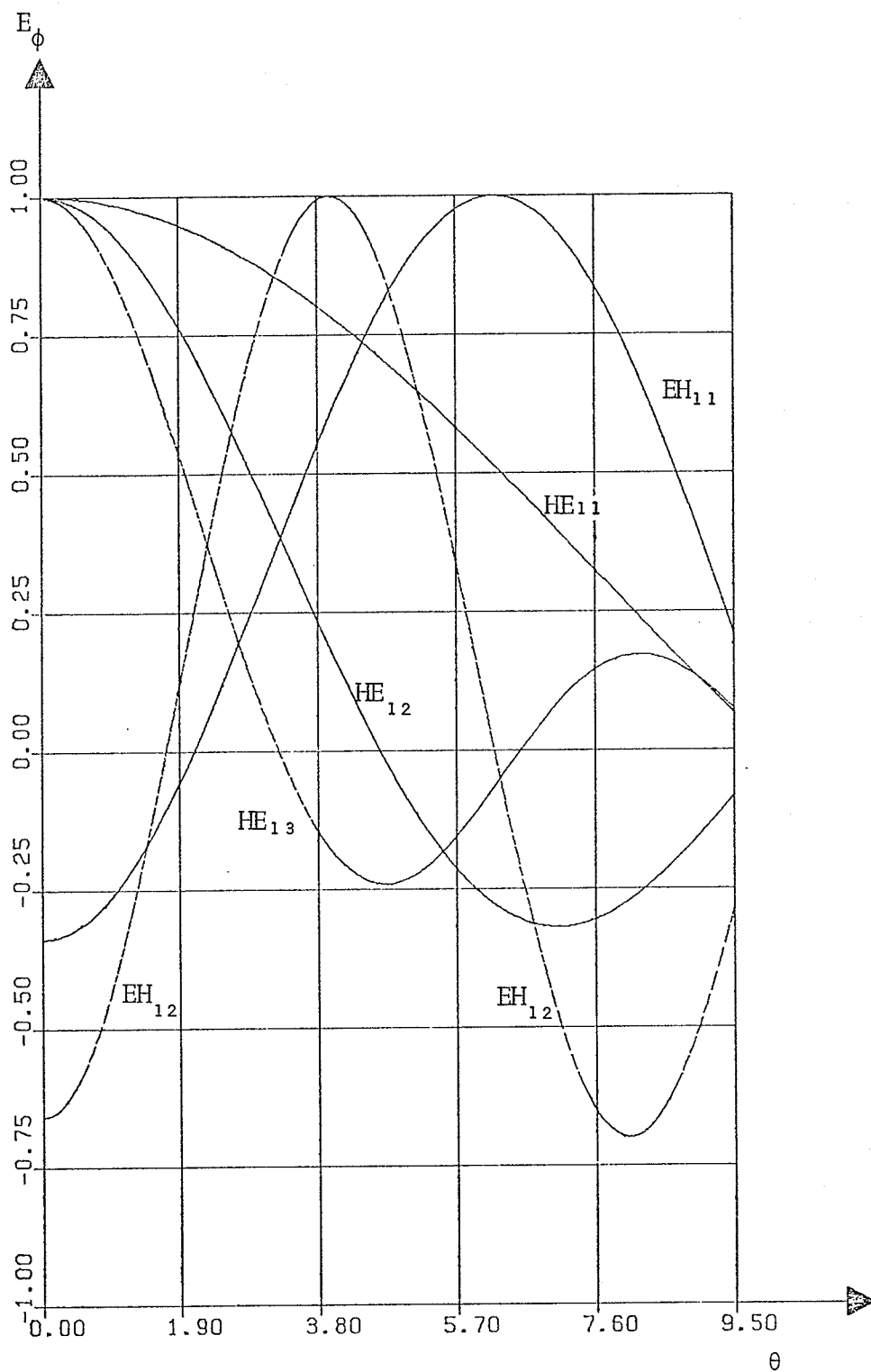


Fig. 3.12 Theoretical H-plane aperture amplitude distribution for first five modes of a dielectric cone with  $\theta_e = 9.5^\circ$ ,  $k_2 \ell = 97.2447$ ,  $\epsilon_r = 2.28$  and  $m = 1$ .

in the particular mode to the incident mode, can be determined by using the procedure described below. The mode matching procedure used below is similar to the one given by Clarricoats and Slim (1967).

Let the fields on the left side of the junction be given by  $\bar{E}_i, \bar{H}_i$  and those on the right side have the components  $\bar{E}_{m,n}, \bar{H}_{m,n}$ . Matching the tangential field components over the boundary gives

$$\bar{E}_i (1 + \Gamma_1) = \sum_n \bar{A}_{ms,n} \bar{E}_{m,n} \quad (3.98)$$

$$\bar{H}_i (1 - \Gamma_1) = \sum_n \bar{A}_{ms,n} \bar{H}_{m,n} \quad (3.99)$$

where  $\Gamma_1$  is the voltage reflection coefficient for the dominant mode in the conical horn. The above equations have been written under the assumption that the power in the incident field is carried only by one component having the azimuthal dependence  $m$ . Taking the cross product of the two equations by  $\bar{H}_{m,n}^*$  and  $\bar{E}_{m,n}^*$ , respectively and using the orthogonality of the modes leads to

$$\bar{a}_{m,n} = \frac{\bar{A}_{ms,n}}{1 + \Gamma_1} = \frac{\int_A (\bar{E}_i \times \bar{H}_{m,n}^*) \cdot \bar{n} \, da}{\int_A (\bar{E}_{m,n} \times \bar{H}_{m,n}^*) \cdot \bar{n} \, da} \quad (3.100)$$

and

$$\bar{b}_{m,n} = \frac{\bar{A}_{ms,n}}{1 - \Gamma_1} = \frac{\int_A (\bar{H}_i \times \bar{E}_{m,n}^*) \cdot \bar{n} \, da}{\int_A (\bar{H}_{m,n} \times \bar{E}_{m,n}^*) \cdot \bar{n} \, da} \quad (3.101)$$

where  $\bar{n}$  is the unit normal to the junction surface. From equations (3.100) and (3.101):

$$\bar{A}_{ms,n} = \frac{2 \bar{a}_{m,n} \bar{b}_{m,n}}{\bar{a}_{m,n} + \bar{b}_{m,n}} \quad (3.102)$$

and

$$\Gamma_1 = \frac{\bar{b}_{m,n} - \bar{a}_{m,n}}{\bar{a}_{m,n} + \bar{b}_{m,n}} \quad (3.103)$$

The excitation efficiency of the  $n^{\text{th}}$  mode is then given by

$$\eta_{m,n} = \bar{A}_{ms,n} \times \bar{A}_{ms,n}^* \frac{\int_A (\bar{E}_{m,n} \times \bar{H}_{m,n}^*) \cdot \bar{n} \, da}{\int_A (\bar{E}_1 \times \bar{H}_1^*) \cdot \bar{n} \, da} \quad (3.104)$$

with the value of the coefficient  $\bar{A}_{ms,n}$  obtained from Eq. (3.102).

Assuming that the power in the conical horn is carried only by  $TE_{11}$  mode, the constant  $\bar{A}_{ms,n}$  of the  $n^{\text{th}}$  mode with unity azimuthal dependence in the dielectric cone is given by

$$\bar{A}_{ms,n} = -2j \frac{h_v(k_1 a) h'_v(k_1 a)}{h_s(k_c a)} \frac{I_2 I_3}{I_1 [h_v(k_1 a) I_2 - j h'_v(k_1 a) I_3]} \quad (3.105)$$

where

$$k_1 = \omega \sqrt{\epsilon_1 \mu_1}$$

$$I_1 = \int_0^\theta e^{(E_{\theta c} H_{\phi c} - E_{\phi c} H_{\theta c}) \sin \theta} \, d\theta \quad (3.106)$$

$$I_2 = \int_0^\theta e \left[ -m \frac{P_v^m(\cos \theta)}{\sin \theta} H_{\phi c} - \frac{dP_v^m(\cos \theta)}{d\theta} H_{\theta c} \right] \sin \theta \, d\theta \quad (3.107)$$

$$I_3 = \int_0^\theta e \left[ -\frac{k_1}{\omega\mu} \frac{dP_v^m(\cos\theta)}{d\theta} E_{\phi c} + \frac{k_1 m}{\omega\mu} \frac{P_v^m(\cos\theta)}{\sin\theta} E_{\theta c} \right] \sin\theta \, d\theta \quad (3.108)$$

and  $a$  = length of the conical horn.

The above equations have been obtained by using equations (3.28) - (3.31) for the fields in the conical horn with a dielectric material and equations (3.90) - (3.93) for the fields in the dielectric cone.

The variation of the excitation efficiencies with dielectric constant for the first three dominant modes are indicated in Fig. 3.13. The excitation efficiencies of the first two modes decrease with an increase in the dielectric constant. For the third  $HE_{12}$  mode, there is an increase in the excitation efficiency with the dielectric constant. However, both the second and third order modes have constant excitation efficiencies for relative permittivity greater than 3.0.

The effect of changing the dielectric cone length on the excitation efficiency is shown in Fig. 3.14. The amount of change in excitation efficiency is small for a dielectric constant of 2.5 as compared to the change for a dielectric constant of 1.1. An increase in dielectric cone length results in a decrease in excitation efficiencies of the first two modes and an increase in the third mode. Although the minimum cone length indicated in Fig. 3.14 has the value  $k_2 \ell = 100$ , calculations have also been performed for lengths less than this value. Based on these calculations, the maximum efficiency of the dominant mode occurs around  $k_2 \ell = 70$ , for which value the validity of the approximations is questionable.

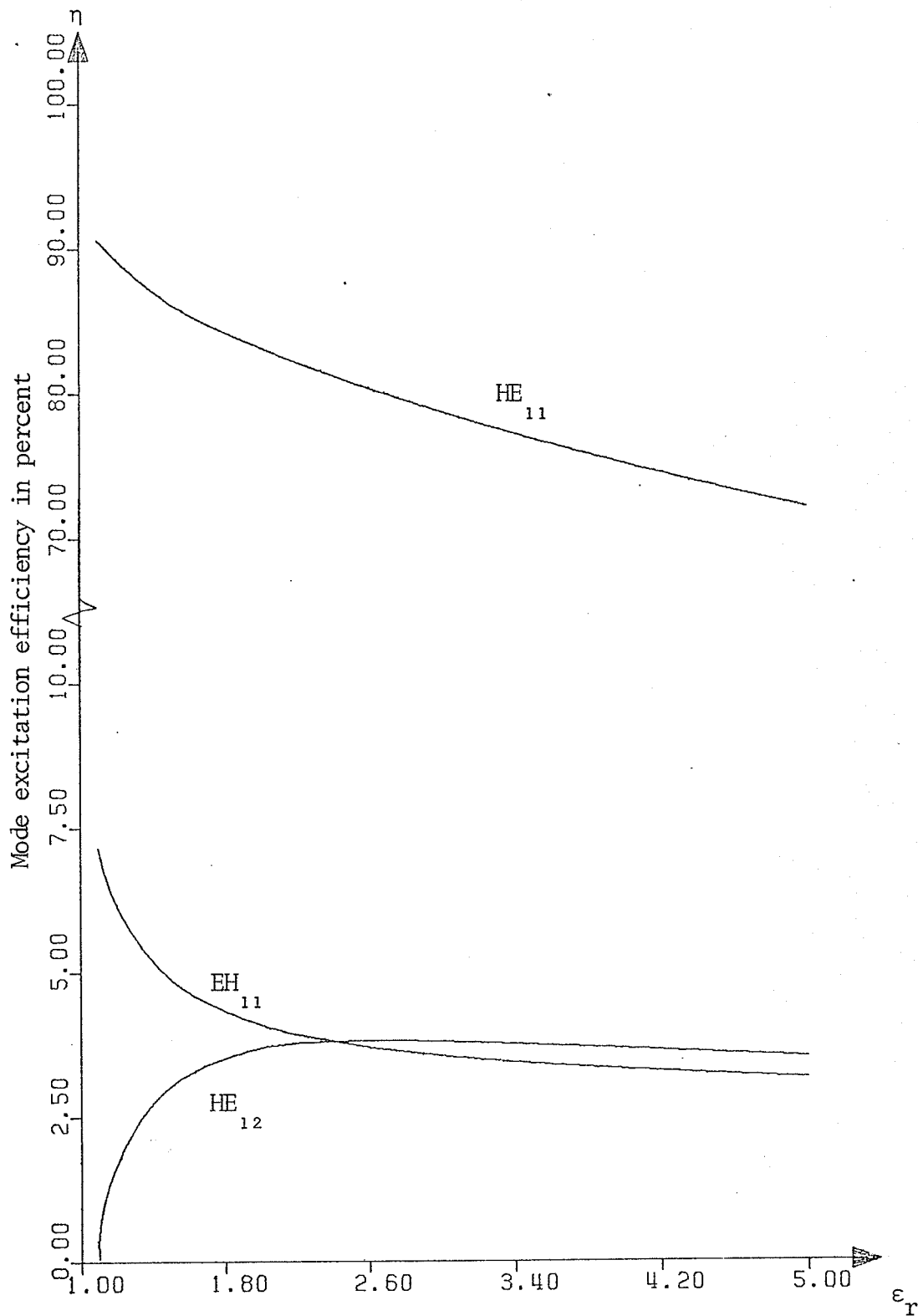


Fig. 3.13 Variation of mode excitation efficiencies with relative permittivity of the cone material for  $k_2 a = 100$ ,  $k_2 a = 35$  and  $\theta_e = 10^\circ$ .

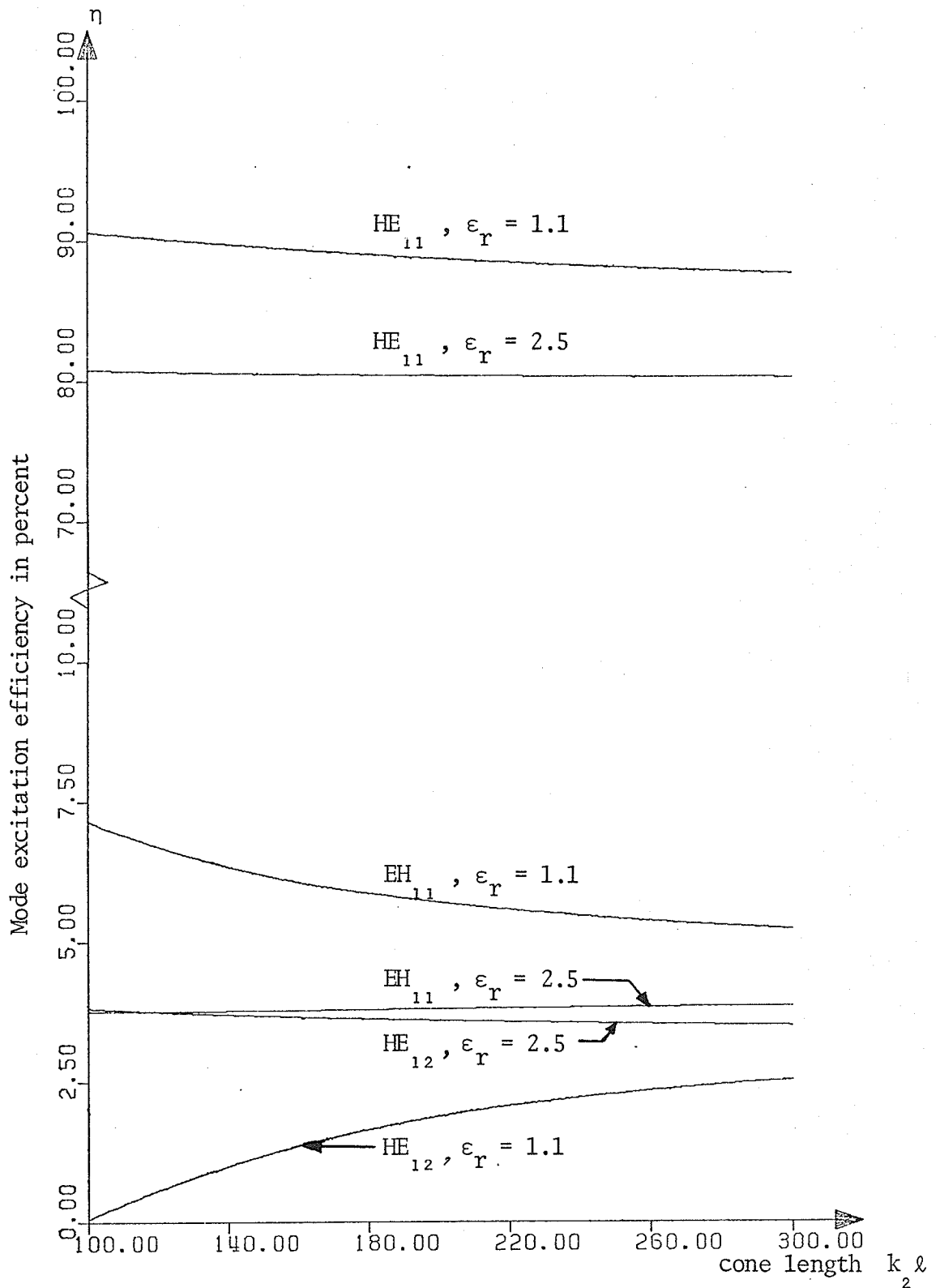


Fig. 3.14 Variation of mode excitation efficiencies with the cone length  $k_2 l$  of the dielectric material for  $k_2 a = 35.0$  and  $\theta_e = 10^\circ$ .

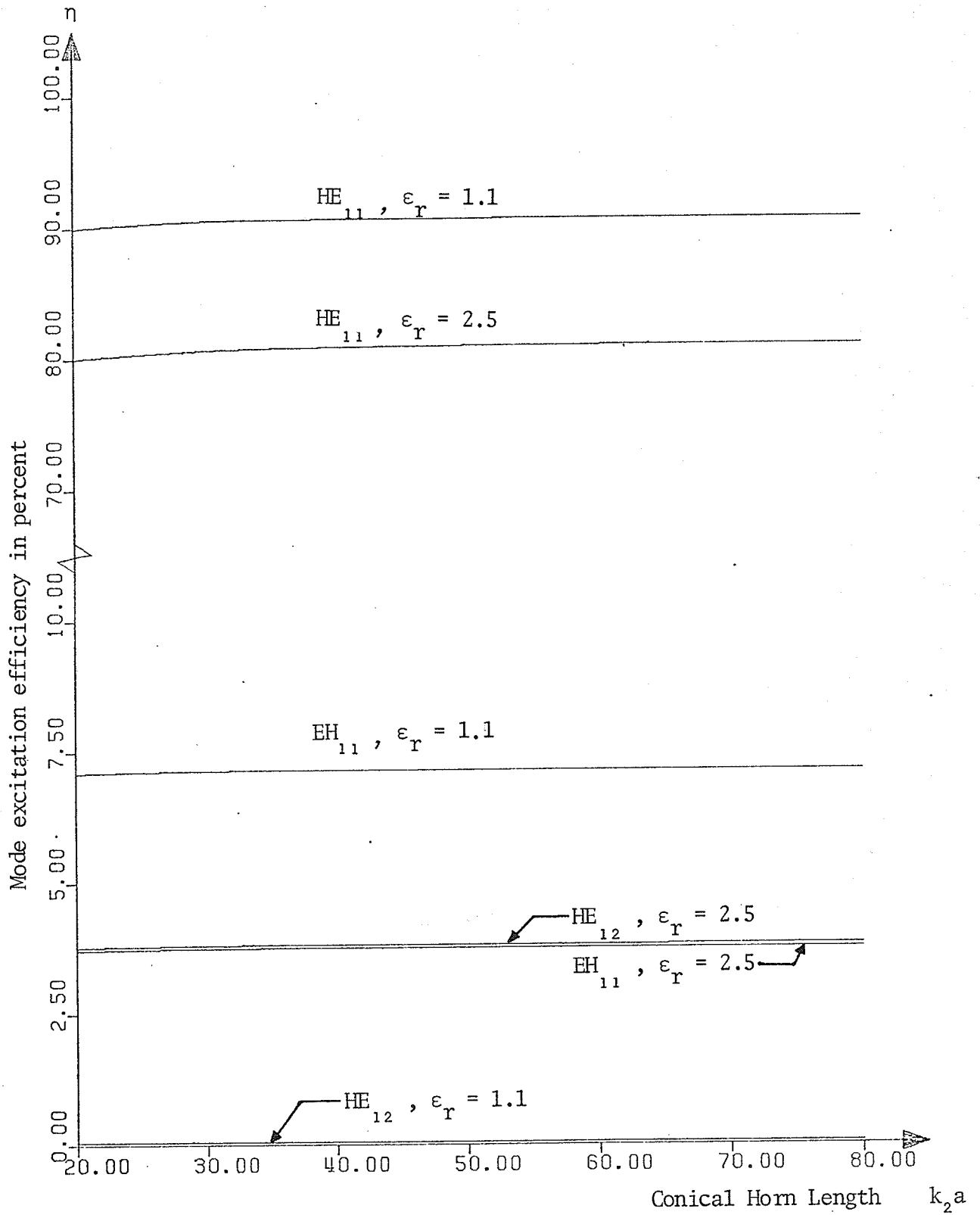


Fig. 3.15 Variation of mode excitation efficiencies with conical horn length for  $k_2 l = 100$  and  $\theta_e = 10^\circ$ .

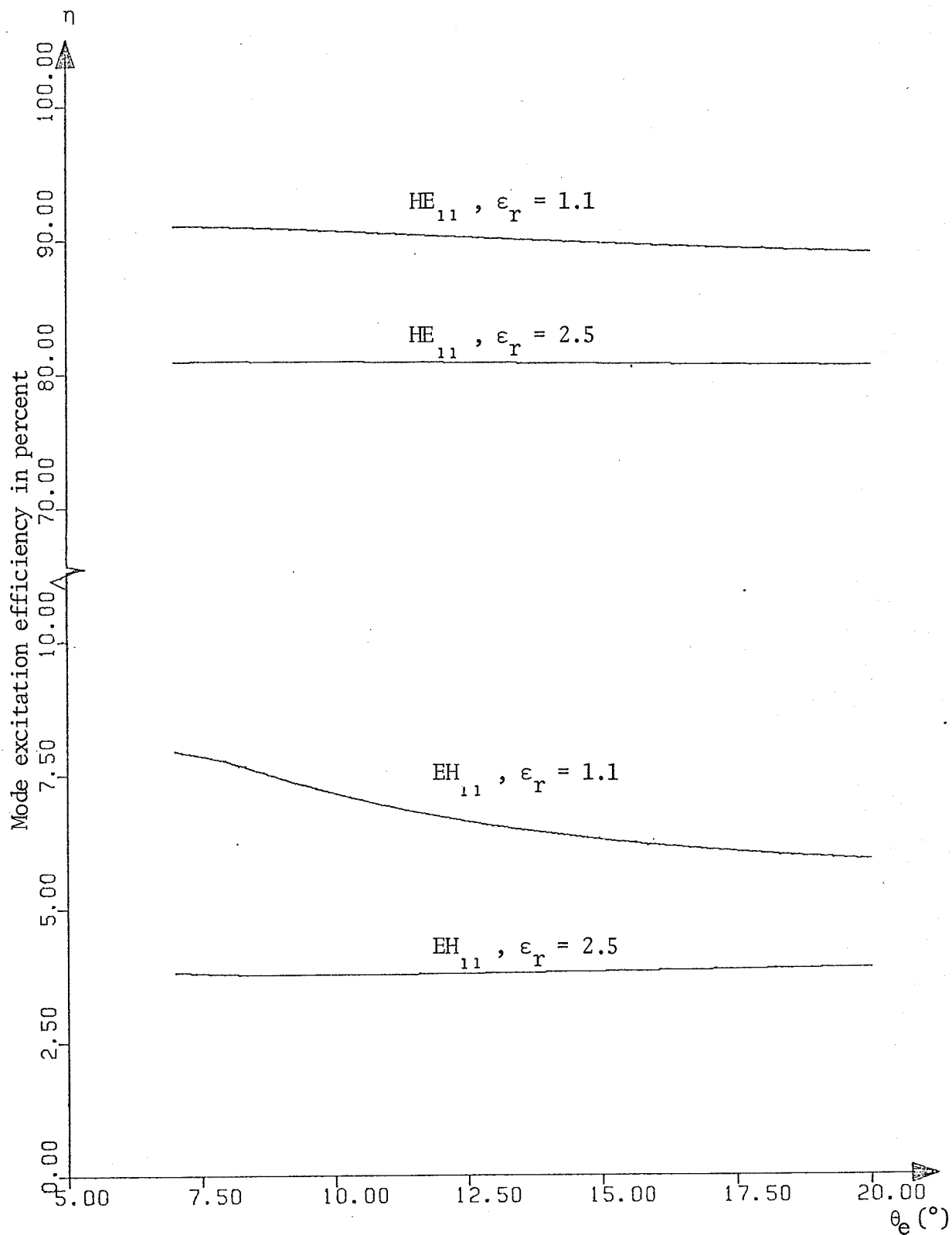


Fig. 3.16 Variation in mode excitation efficiencies with cone flare angle for  $k_2 l = 100$  and  $k_2 a = 40.0$ .

The effect of varying the conical horn length ( $k_2 a$ ) and the cone flare angle ( $\theta_e$ ) on the excitation efficiencies is small (Figures 3.15 and 3.16) as compared to the effect of cone length and the dielectric constant. The excitation efficiency increases with conical horn length up to a certain length and then virtually remains constant. An increase in cone flare angle results in a small decrease of the excitation efficiencies.

One common feature in all the three Figures 3.14 - 3.16, is that the amount of variation in excitation efficiency with cone length ( $k_2 l$ ), conical horn length ( $k_2 a$ ), and cone flare angle ( $\theta_e$ ) decreases with the dielectric constant. Further investigations are needed to understand and explain these observations.

### 3.3.4 Theoretical and Experimental Radiation Patterns

The aperture fields of the dielectric cone, equations (3.90) - (3.97), with the constant  $A_{ms}$  determined from Eq. (3.102) can be used in Eq. (3.32) to obtain the theoretical radiation patterns of the dielectric cone antenna. The surface of integration is chosen to be a plane normal to the z-axis, so as to correspond with the assembled dielectric cone (Fig. 3.17). The radiation field components at an observation point ( $r', \theta', \phi'$ ) for this choice of surface of integration are as follows:

$$\begin{aligned}
 E_{S\theta'}(\theta', \phi') = & -j^m \frac{k_2 l}{4r'} \exp(-jk_2 r') A_{ms} \cos(m\phi') \int_0^{\theta_e} e^{-\xi \cos\theta} [-E_{\theta C} \xi \cos\theta \\
 & + E_{\phi C} \delta - (\mu_2/\epsilon_2)^{1/2} H_{\theta C} \delta \cos\theta \cos\theta' - (\mu_2/\epsilon_2)^{1/2} \\
 & H_{\phi C} \xi \cos\theta'] \exp(j\alpha) h_s(k_2 l \cos\theta_e / \cos\theta) \sin\theta \, d\theta \quad (3.109)
 \end{aligned}$$

$$\begin{aligned}
E_{S\phi'}(\theta', \phi') = & -j^m \frac{k_2 \ell}{4r'} \exp(-jk_2 r') A_{ms} \text{Sin}(m\phi') \int_0^{\theta_e} [E_{\theta C} \delta \text{Cos}\theta \text{Cos}\theta' \\
& - E_{\phi C} \xi \text{Cos}\theta' + (\mu_2/\epsilon_2)^{1/2} H_{\theta C} \xi \text{Cos}\theta + (\mu_2/\epsilon_2)^{1/2} H_{\phi C} \delta] \\
& \exp(j\alpha) h_s(k_c \ell \text{Cos}\theta_e/\text{Cos}\theta) \text{Sin}\theta \, d\theta
\end{aligned} \tag{3.110}$$

where

$$\xi = J_{m-1}(\psi) - J_{m+1}(\psi) \tag{3.111}$$

$$\delta = J_{m-1}(\psi) + J_{m+1}(\psi) \tag{3.112}$$

$$\psi = k_2 \ell \text{Cos}\theta \text{Cos}\theta' \tag{3.113}$$

and

$$\alpha = k_2 \ell \text{Sin}\theta \text{Sin}\theta' \tag{3.114}$$

It should be noted that in writing the above equations the integration with respect to  $\phi$  has been performed in a closed form and the reflection from the aperture plane has been neglected. The reflection coefficients for field components at the aperture plane are derived in Appendix B. These reflection coefficients are found to be independent of the variable  $\phi$  and therefore the integration with respect to this variable can still be performed in a closed form. Taking the reflection into account modifies the radiation field components as:

$$\begin{aligned}
E_{S\theta'}(\theta', \phi') = & -j^m \frac{k_2 \ell}{4r'} \exp(-jk_2 r') A_{ms} \text{Cos}(m\phi') \int_0^{\theta_e} [-E_{\theta C} (1 - R_{11}) \\
& \xi \text{Cos}\theta + E_{\phi C} (1 + R_{\perp}) \delta - (\mu_2/\epsilon_2)^{1/2} H_{\theta C} (1 - R_{\perp}) \delta \text{Cos}\theta \text{Cos}\theta' \\
& - (\mu_2/\epsilon_2)^{1/2} H_{\phi C} (1 + R_{11}) \xi \text{Cos}\theta'] \exp(j\alpha) h_s(k_c \ell \text{Cos}\theta_e/\text{Cos}\theta) \\
& \text{Sin}\theta \, d\theta
\end{aligned} \tag{3.115}$$

$$\begin{aligned}
E_{S\phi'}(\theta', \phi') &= -j^m \frac{k \ell}{4r'} \exp(-jk_2 r') A_{ms} \sin(m\phi') \int_0^\theta [E_{\theta c} (1 - R_{11}) \\
&\quad \delta \cos\theta \cos\theta' - E_{\phi c} (1 + R_{\perp}) \xi \cos\theta' + (\mu_2/\epsilon_2)^{1/2} H_{\theta c} (1 - R_{\perp}) \\
&\quad \xi \cos\theta + (\mu_2/\epsilon_2)^{1/2} H_{\phi c} (1 + R_{11}) \xi \cos\theta'] \exp(j\alpha) \\
&\quad h_s(k_c \ell \cos\theta_e / \cos\theta) \sin\theta \, d\theta \tag{3.116}
\end{aligned}$$

where

$$R_{11} = \frac{\sqrt{\epsilon_2} \cos\theta - \sqrt{\epsilon_1} \cos\theta_t}{\sqrt{\epsilon_2} \cos\theta + \sqrt{\epsilon_1} \cos\theta_t} \tag{3.117}$$

$$R_{\perp} = \frac{\sqrt{\epsilon_1} \cos\theta - \sqrt{\epsilon_2} \cos\theta_t}{\sqrt{\epsilon_1} \cos\theta + \sqrt{\epsilon_2} \cos\theta_t} \tag{3.118}$$

and

$$\theta_t = \sin^{-1} (\sqrt{\epsilon_1} \sin\theta / \sqrt{\epsilon_2}) \tag{3.119}$$

Equations (3.115) and (3.116) have been used to obtain the theoretical radiation patterns of the assembled cone. The different parameters of the assembled dielectric cone antenna are shown in Fig. 3.17. The theoretical radiation patterns, using the aperture plane normal to the z-axis, are plotted in Fig. 3.18 along with the measured radiation patterns. The effect of adding higher order modes with the same azimuthal dependence is also indicated.

The theoretical E-plane pattern agrees closely with the measured one up to about 12°. However, the agreement in H-plane patterns is not

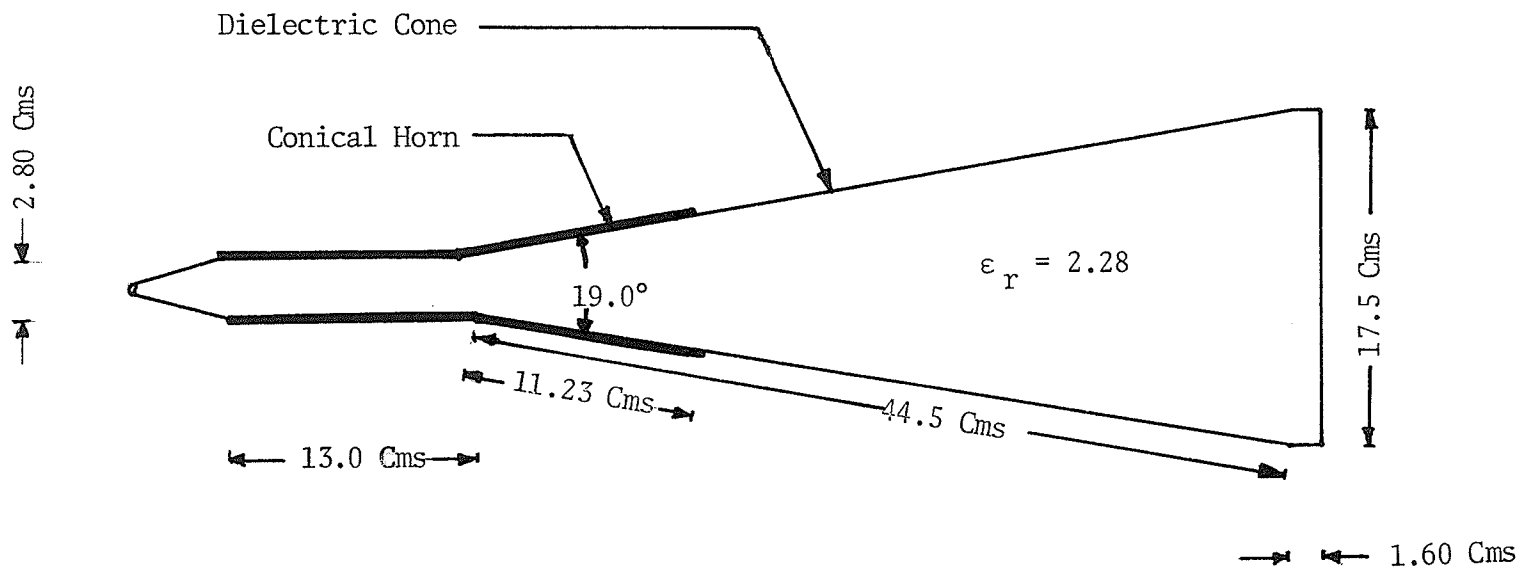


Fig. 3.17 Dimensions of the dielectric cone and the conical horn made for the experiment.

that good. The measured patterns indicate first side lobes around  $20^\circ$  while the theoretical patterns do not indicate any side lobe up to about  $30^\circ$ . The possible reasons for this difference in behaviour may be due to the assumptions given by equations (3.75), (3.76) and the excitation of higher order modes in the dielectric waveguide.

To observe the effect of the launcher and the surface waves, an absorbing material was wrapped around the dielectric cone up to a few inches from the main aperture. Figure 3.19 shows that the E-plane radiation patterns of the dielectric cone with and without absorbing material differ only in the side lobes beyond  $25^\circ$ . This indicates that the launcher and the surface waves (if excited) affect only the far out side lobes in the E-plane. However, the H-plane pattern was found to be not appreciably affected by the radiation from the launcher and the surface waves. Since there is no appreciable difference in the radiation patterns with and without absorbing material around  $10^\circ$ , this should indicate that the surface waves are either not excited at all or if excited have very small amplitudes. However, a further investigation of the discrepancies is warranted.

The experimental radiation patterns have also been observed at frequencies higher than  $8.5 \text{ GHz}$  and the best operating frequency, from the point of first side lobe level less than 20 dB, is  $10.2 \text{ GHz}$  (Fig. 3.20). This is probably due to the excitation of dual modes in the circular

waveguide with the dielectric material,

### 3.4 SUMMARY AND DISCUSSION

This chapter has presented a brief description of different types of feeds used for reflector antennas. Among the various possible feeds the horn antenna has enjoyed the most popularity mainly due to the ruggedness, simplicity of design and construction, low side lobe level and low cross-polarization component.

The conical horn antenna, in the present case, is being used as a launcher for the dielectric cone feeds to the main reflector. The analysis of the conical horn antenna shows a good agreement of the theoretical radiation patterns with the measured patterns. However, the agreement of the theoretical radiation patterns for the dielectric cone antenna with the measured patterns is not very good. This may be due to the approximation made in developing the characteristic equation as well as the excitation efficiencies determination. This requires a further investigation of the dielectric cone antenna.

The mode representation of the dielectric cone antenna is utilized in the next two chapters to evaluate the performance of the reflector antennas using dielectric cone feed.

CHAPTER IV

ANTENNAS WITH MODIFIED DIELECTRIC

CONE FEED

#### 4.1 INTRODUCTION

The use of low permittivity dielectric cone to reduce the spillover in a Cassegrain antenna, as shown in Fig. 4.1, was first proposed by Bartlett and Moseley (1966). In this proposal, the dielectric guiding structure (Dielguide) placed between the primary feed and the subreflector utilizes the phenomenon of total internal reflection to reduce the spillover. The use of dielectric cone in this manner not only reduces the spillover but also removes the support structure blockage which, as shown in Chapter II, can be a source of reduction in efficiency for the Cassegrain antenna. The interest in these "dielguides" has persisted since its announcement [Bartlett and Pietsch, 1968; Bartlett and Moseley, 1969; Bartlett, 1971]. The basic advantage of spillover reduction in the dielguides was only demonstrated on the basis of ray-optics concepts [Bartlett and Moseley, 1966]. In this paper it was demonstrated how some of the radiation from the feed horn which misses the metallic subreflector in the absence of the dielectric cone arrives there in its presence owing to the total internal reflection at the dielectric-air boundary (Fig. 4.1). No consideration was given to the field excitation and propagation in the dielectric cone. An approximate theory was later on proposed [Clarricoats and Salema, 1971] to explain the propagation and radiation characteristics of conical dielectric waveguides of narrow flare angles. In this study the dielectric cone antennas, employing conical horns, were shown to have the characteristics resembling closely those of the corrugated horns [Clarricoats and Salema, 1973].

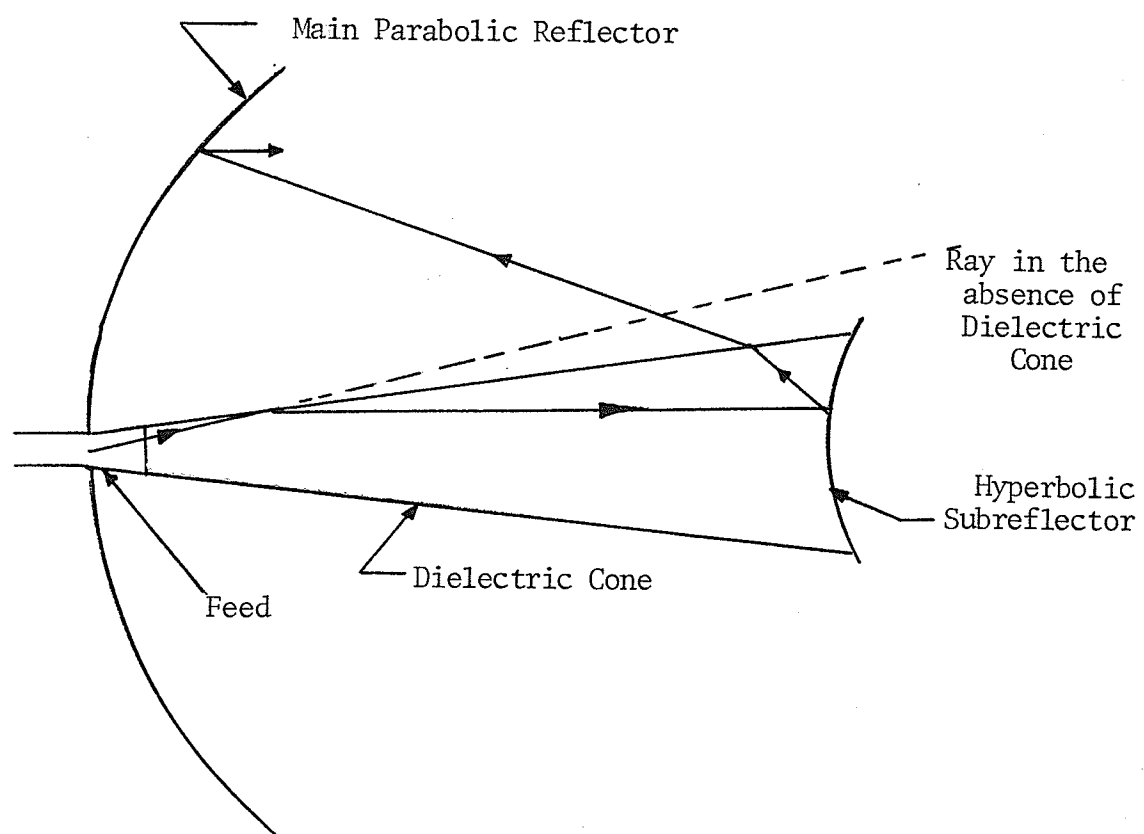


Fig. 4.1 Dielectric cone feed reflector antenna

In the Cassegrain antenna employing a dielectric cone feed, the dielectric cone is inserted between the subreflector and the launcher. Fixing the subreflector to the dielectric cone proved to be a difficult practical problem [Salema, 1972] in the initial stages. This was due to the weight of the machined subreflector, the requirements of accurate centering and the alignment of the dielectric cone and the subreflector axes [Salema, 1972]. These problems can theoretically be circumvented by replacing the subreflector with a shaped dielectric surface. The theoretical feasibility of replacing the subreflector has already been indicated [Chugh and Shafai, 1976; Shafai and Chugh, 1976].

The present chapter provides the design and analysis of the dielectric cone antenna in which the fabricated plastic foam subreflector is replaced with the shaped dielectric surface. The theoretical radiation patterns of the antennas employing a modified dielectric cone feed will also be presented.

#### 4.2 DESIGN OF THE SHAPED REFLECTING SURFACE

The design procedure for shaping the dielectric surface, instead of a polished or metallic subreflector, uses analytical expressions of geometrical optics principles. For the modified dielectric cone to act as a feed to a reflector, any ray incident on the shaped surface  $S$  from the launcher must be totally internally reflected at the surface  $S$  (Fig. 4.2). Thus, the angle of the incident ray with the surface normal  $\theta_{nic}$  should be greater than or equal to the critical angle [Born and Wolf, 1964]. From the Snell's law of reflection, the critical angle is

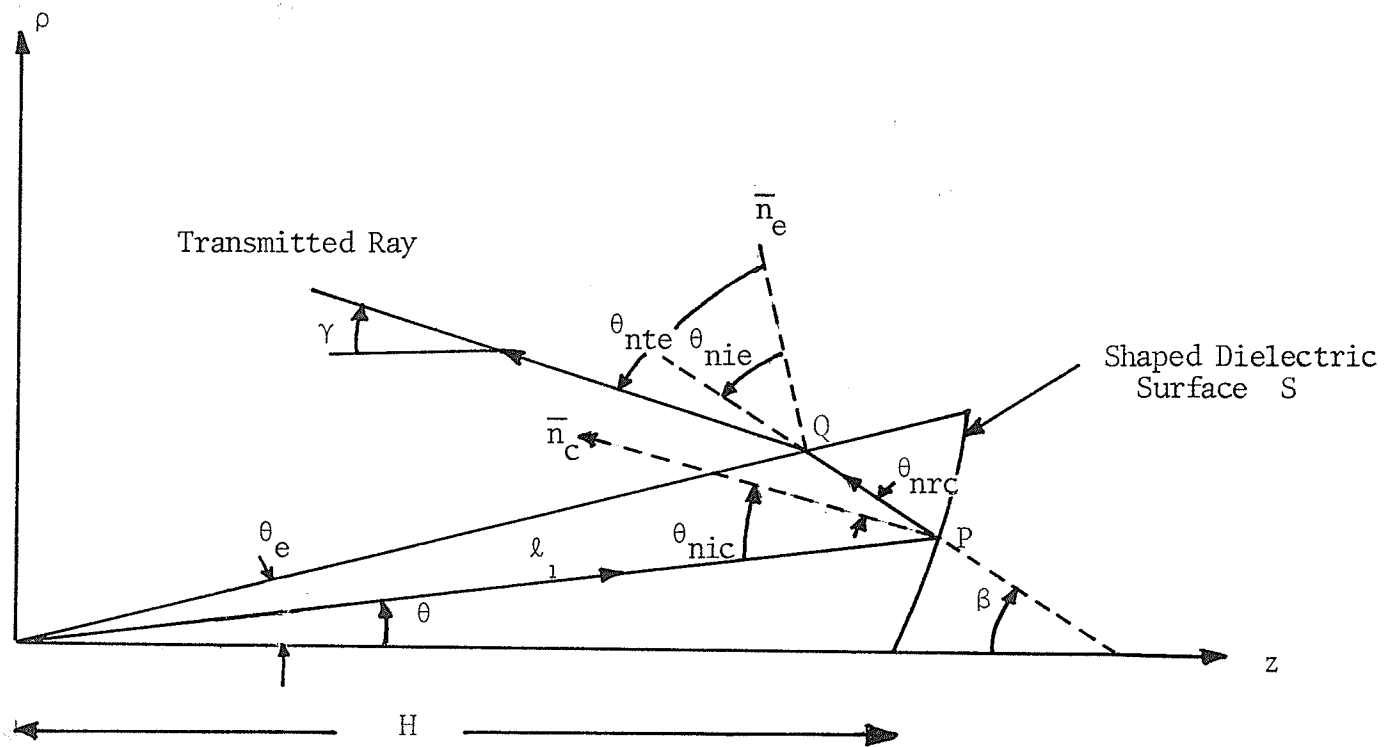


Fig. 4.2 Shaped surface geometry for the dielectric cone feed

a function of the dielectric constants of the two media at the interface. With one of the media being air and the incident wave passing from a medium of relative permittivity  $\epsilon_1$ , the critical angle  $\theta_c$  is given by

$$\theta_c = \text{Sin}^{-1}(1.0/\sqrt{\epsilon_1}) \quad (4.1)$$

Since the angle  $\theta_{\text{nic}}$  has to be greater than or equal to the critical angle, let angle  $\theta_{\text{nic}}$  be expressed as

$$\theta_{\text{nic}} = \theta_c + K\theta \quad (4.2)$$

where  $\theta$  is the angle of the incident ray at the phase centre and  $K$  is some positive constant.

Snell's law of reflection along with the geometry shown in Fig. 4.2 gives

$$\theta_{\text{nic}} = \theta_{\text{nrc}} = \left(\frac{\beta + \theta}{2}\right) \quad (4.3)$$

where  $\beta$  and  $\theta_{\text{nrc}}$  are the angles of the reflected ray with the horizontal axis and the surface normal, respectively. If  $\ell_1$  is the length of the ray from the phase centre to the point P on the surface, then using equation (4.2) and (4.3) the differential equation for the shaped surface S is given by

$$\begin{aligned} \frac{d\ell_1}{\ell_1 d\theta} &= \tan \left(\frac{\beta + \theta}{2}\right) \\ &= \tan (\theta_c + K\theta) \end{aligned} \quad (4.4)$$

or

$$\rho_1 = H \frac{\cos^{(1/K)} \theta_c}{\cos^{(1/K)} (\theta_c + K\theta)} \quad (4.5)$$

where  $H$  is the distance of the surface  $S$  from the phase centre for  $\theta = 0$ . It is observed from Eq. (4.5) that the surface curvature is a function of the relative permittivity of the cone medium as well as the constant  $K$ .

The suitability range for the constant  $K$  can be determined by imposing the restriction that the reflected ray from the shaped surface  $S$  when incident on the dielectric cone boundary is not totally internally reflected. This essentially means that the angle  $\theta_{nie}$  of the ray  $PQ$  with the edge normal should be less than  $\theta_c$ , the critical angle. From Fig. 4.2, this condition requires that

$$90^\circ - \theta_e - \theta_c \leq \beta \quad (4.6)$$

where  $\theta_e$  is the cone flare angle. The second condition which also needs to be satisfied is that the transmitted rays from the cone edge should be going in the backward direction for the structure to act as a feed to the main reflector. From Fig. 4.2, the angle of the transmitted ray with horizontal axis is given by

$$\gamma = 90^\circ - \theta_e - \sin^{-1}(\sqrt{\epsilon_1} \sin \theta_{nie}) \quad (4.7)$$

Assuming that the maximum value of the angle  $\gamma$  is along

the edge normal, the range for  $\beta$  is

$$90^\circ - \theta_e - \theta_c \leq \beta \leq 90^\circ - \theta_e \quad (4.8)$$

or

$$90^\circ - \theta_e - \theta_c \leq 2\theta_c + (2K-1)\theta \leq 90^\circ - \theta_e \quad (4.9)$$

The above equation when satisfied for angle  $\theta$  being equal to zero gives the maximum and minimum permissible values of the dielectric constant for a given cone angle. Some values for the range of permissible dielectric constants are presented in Table 4.1 for different cone angles.

Equation (4.9) when satisfied for  $\theta = \theta_e$  provides the permissible values for the constant  $K$ . However it should be noted that the minimum possible value for  $K$  is either zero or the one provided by Eq. (4.9) whichever is greater. Table 4.2 gives the permissible values of  $K$  for a cone flare angle of  $5^\circ$ .

The shape variations of the surface  $S$  with  $K$  for a constant value of relative permittivity are shown in Fig. 4.3. The shape is convex towards the  $y$ -axis for  $K$  less than one and for  $K = 1$  the slope is constant. For values greater than  $K = 1$ , the slope of the surface is convex towards the  $x$ -axis.

The surface curvature for  $K = 1$  is a straight line (Fig. 4.4) with a slope given by the cotangent of the critical angle. The  $x$ -axis (zero slope) corresponds to a relative permittivity of one and  $y$ -axis corresponds to an infinite relative permittivity. With the medium surround-

Table 4.1

Maximum and Minimum Permissible Values of  
Relative Permittivity

	$\theta_e$	$\epsilon_{\text{minimum}}$	$\epsilon_{\text{maximum}}$
1	5.00	2.19095	4.43960
2	10.00	2.42028	4.96473
3	15.00	2.69840	5.59891
4	20.00	3.03961	6.37433
5	25.00	3.46391	7.33605
6	30.00	4.00000	8.54863

Table 4.2

Permissible Values of K for Cone Flare Angle = 5°

	$\epsilon$	Calculated $K_{\text{min}}$	Permissible $K_{\text{min}}$	$K_{\text{max}}$
1	2.2	-3.71761	0.0	0.52159
2	2.5	-2.76946	0.0	1.15370
3	3.0	-1.57932	0.0	1.94712
4	3.5	-0.69346	0.0	2.53769
5	4.0	0.0	0.0	3.0000
6	4.4	0.45836	0.45836	3.3055

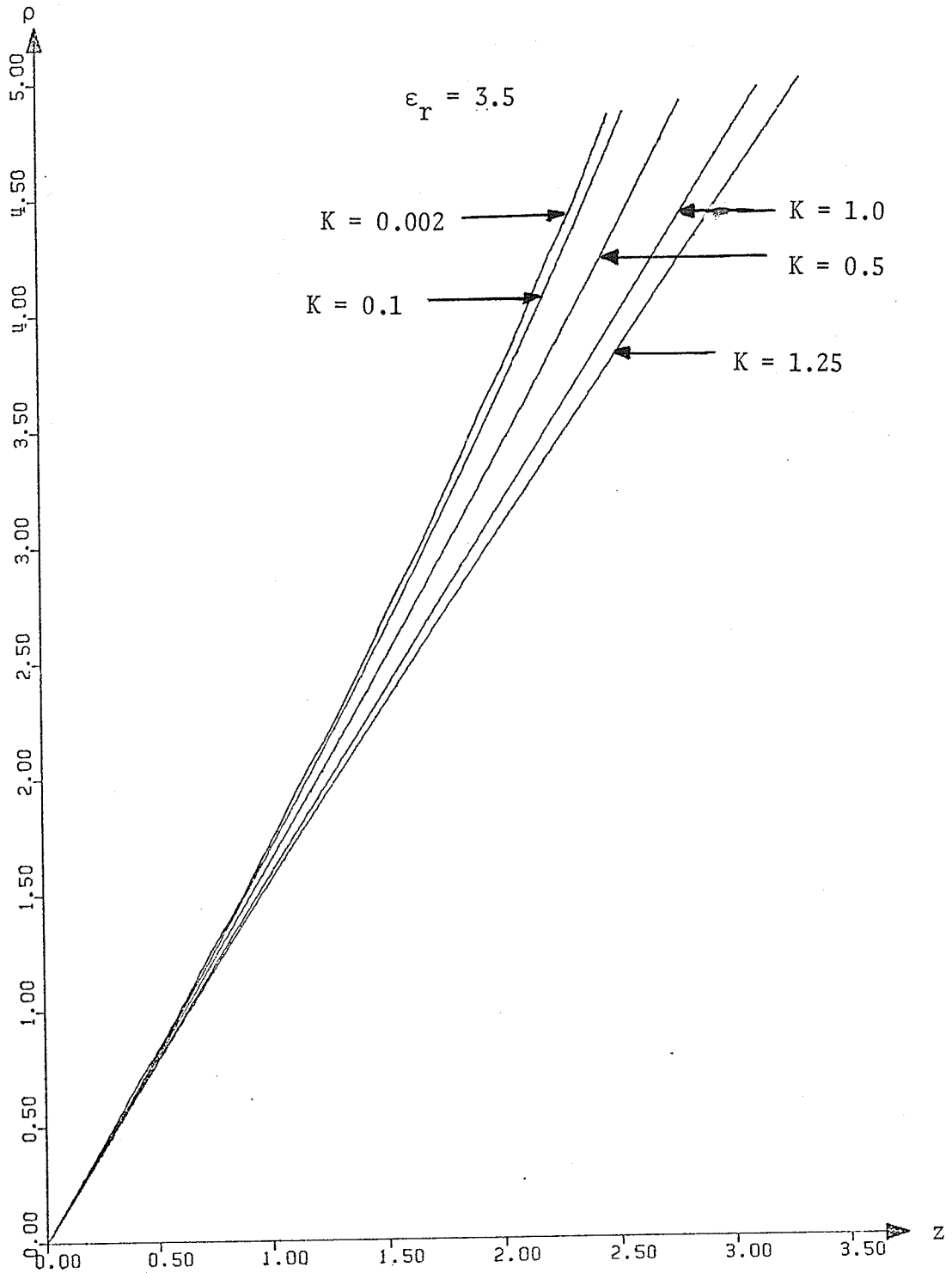


Fig. 4.3 Variation of surface curvature with  $K$ .  
The origin for these curvatures is shifted  
to  $z = H$ .

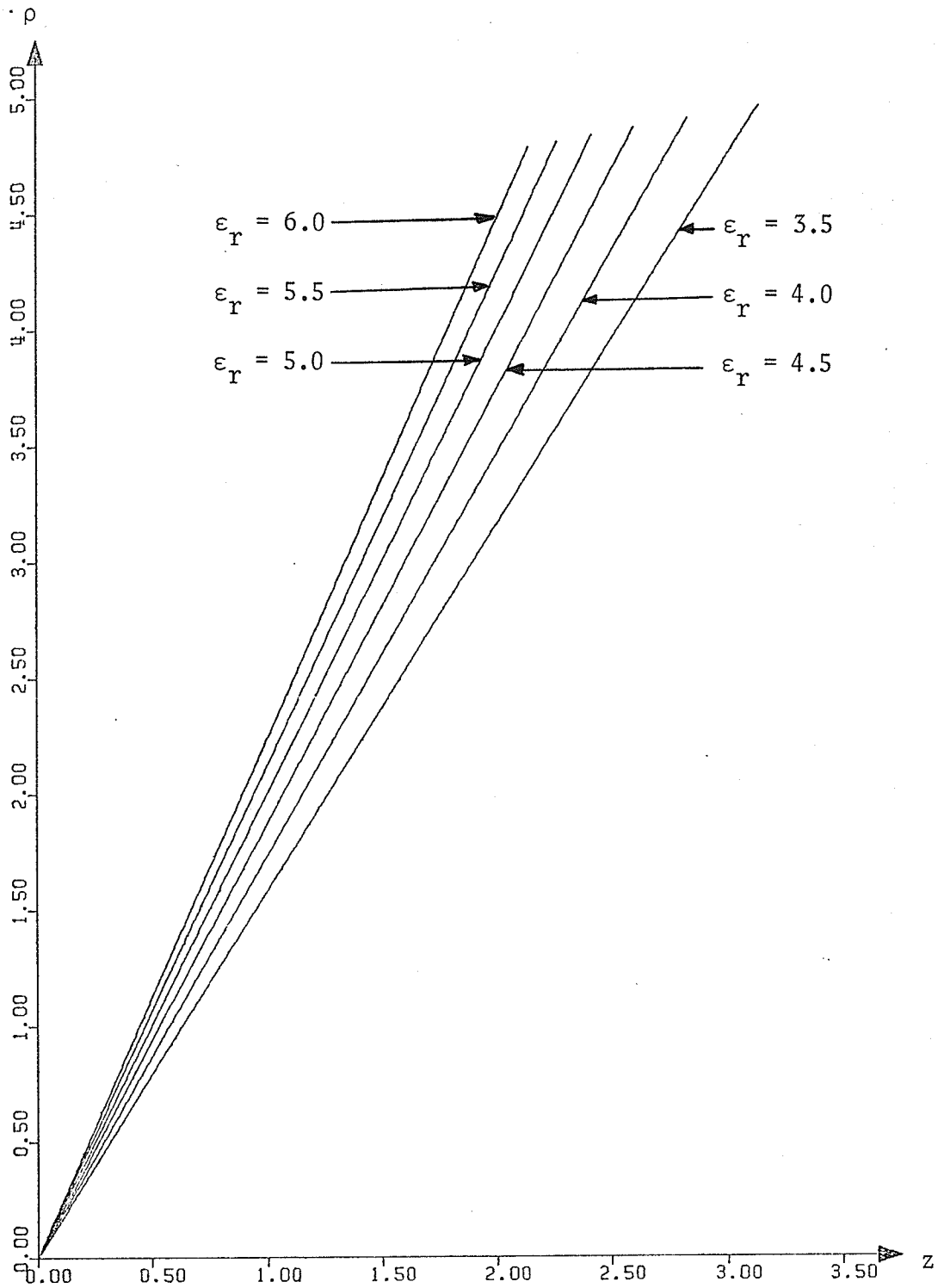


Fig. 4.4 Variation of surface curvature as a function of relative permittivity for  $K = 1$ . The origin for these curvatures is shifted to  $z = H$ .

ing the dielectric cone being air, the values of relative permittivity less than one are not allowed [Sommerfeld, 1964] due to the requirement of a denser incident medium for the total internal reflection.

The variation of the surface curvature with relative permittivity, for very small  $K$ , is shown in Fig. 4.5. The shaped surface has a behaviour of shifting towards the  $y$ -axis with an increase in relative permittivity, similar to the case for  $K = 1$ .

Among the permissible values of  $K$ , two values corresponding to  $K = 1.0$  and  $K = 0.5$  give simple shapes for the subreflector and main reflector, respectively. The subreflector for  $K = 1$  is a cone with flare angle given by  $90^\circ - \theta_c$ , where  $\theta_c$  is the critical angle. For  $K = 0.5$ , the angle  $\gamma$  of the transmitted rays from the cone edge is independent of the incident angle and all the transmitted rays are hence parallel to each other. Therefore the most appropriate choice for the main reflector corresponding to  $K = 0.5$  is the conical reflector. A conical main reflector with a shaped surface corresponding to  $K = 0.5$  gives a constant path length for all the rays from the phase centre to the aperture plane. The reflecting system consisting of conical main reflector is analyzed in the following section.

#### 4.3 ANALYSIS OF CONICAL REFLECTOR WITH MODIFIED DIELECTRIC CONE FEED

The radiation pattern analysis of a reflector antenna using the modified dielectric cone feed of the last section may be performed by using either the scalar diffraction theory of Kirchhoff and Helmholtz [Rusch

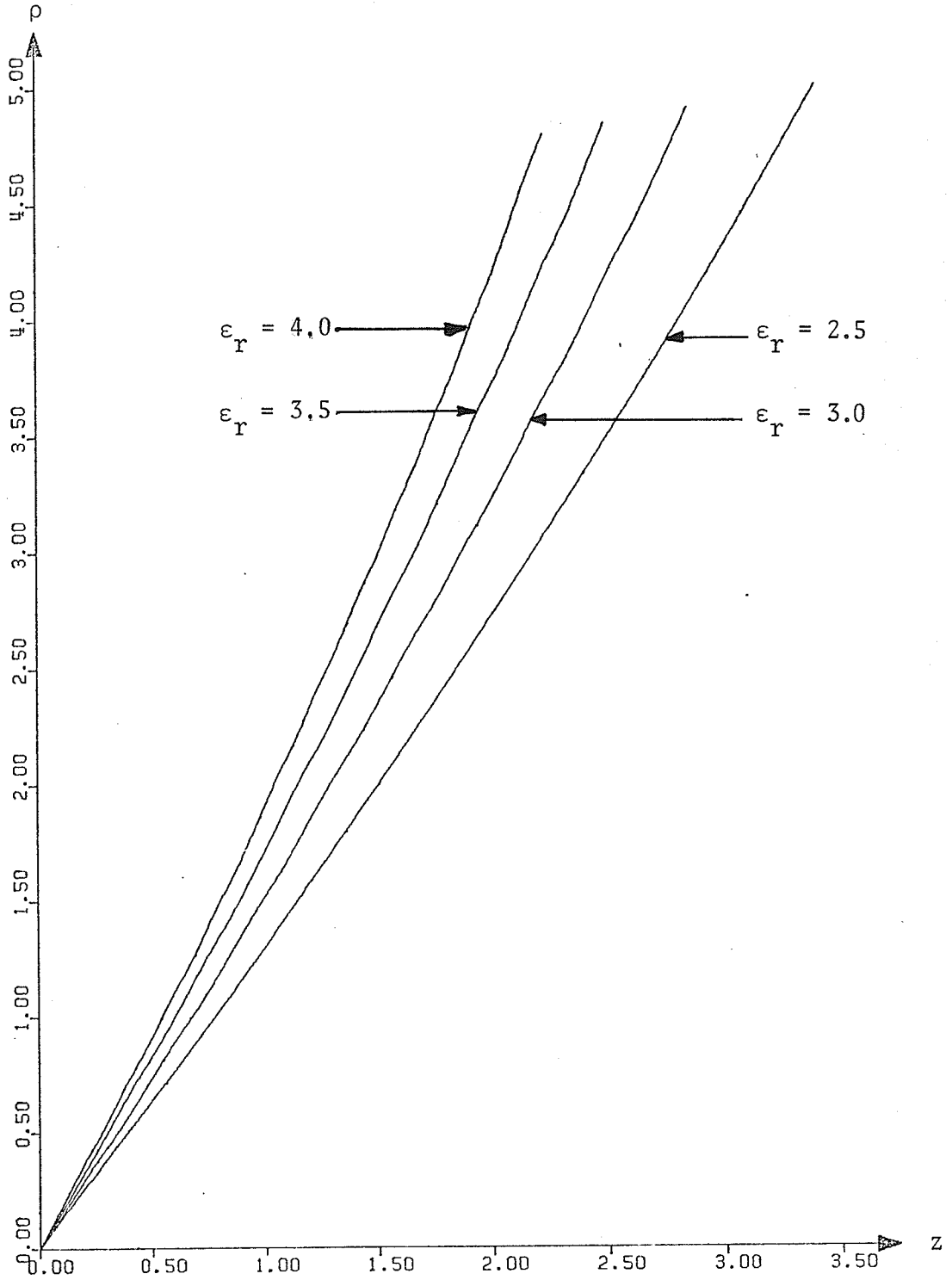


Fig. 4.5 Variation of surface curvature as a function of relative permittivity for  $K = 0.002$ . The origin for these curvatures is shifted to  $z = H$ .

and Potter, 1970] or the vector Kirchhoff diffraction integrals [Rusch and Potter, 1970]. The scalar diffraction theory gives good results in the near side lobes when the field over the aperture is linearly polarized [Silver, 1949], and the contribution of the edge effects can be neglected [Rusch and Potter, 1970]. However, for the modified dielectric cone feed, the total internal reflection at the shaped surface results in phase changes of the reflected field components [Born and Wolf, 1964]. These phase changes of the reflected field components are not equal for the components parallel and perpendicular to the plane of incidence. Therefore, an analysis of the reflector antennas with modified dielectric cone feed, based on scalar diffraction theory, may not provide much useful information. Based on these reasons, the radiation pattern analysis is performed in the following sections using vector Kirchhoff diffraction integrals.

The vector Kirchhoff diffraction integral formulation usage again has two possibilities of either using aperture fields or the current distributions on the reflector. However, for the reflector antennas, the physical-optics induced current method is more accurate than the aperture field method because it includes the effects of axially directed reflector currents [Rusch and Potter, 1970]. It should be noted, however, that both the approaches provide identical results near the reflector axis and the physical-optics method does not accurately represent the field in the backward directions. Since the attention in the present analysis is restricted to the forward direction radiation patterns, it is felt that the physical-optics method is a more appropriate choice.

The determination of the incident fields at the conical main reflector with modified dielectric cone feed may, for convenience, be divided into two parts, namely

- 1) the evaluation of the field components for the spherical hybrid modes propagating inside the dielectric cone,
- and 2) the determination of the fields at the main reflector using geometrical optics principles.

The spherical hybrid modes propagating inside the dielectric cone are evaluated by using the procedure given in Chapter III. The details for evaluating the fields incident on the conical reflector and the aperture fields, from the spherical hybrid modes, are presented in the first subsection. The fields thus evaluated are utilized in the vector Kirchhoff diffraction integral with physical-optics approximation to obtain the theoretical radiation patterns. The details for the radiation pattern calculations are presented in the second subsection.

#### 4.3.1 Aperture Field Distribution for a Conical Reflector

The approximate solution of Chapter III, for the modes in the dielectric cone, is used to determine the incident fields at the shaped reflecting surface. The eigenvalue for these incident fields is a function of the cone angle, relative permittivity of the cone material and the length of the dielectric cone. These parameters are fixed according to the considerations on the availability of the launcher, type of the dielectric material available and the diameter of the shaped surface. The length of the dielectric cone, to be used for the calculation of the

eigenvalue, can for simplicity be taken as the length corresponding to zero angle. The variation in the cone length at different cone angles should not result in any appreciable error due to the small variation in eigenvalues with the cone length (Fig. 3.10).

The incident field at the shaped surface, from equations (3.90) - (3.93) along with the far field approximation, has the field components given by

$$E_{\theta i} = \frac{A_{ms}}{\ell_1} j^{s+1} \exp(-j k_c \ell_1) E_{\theta c} \cos(m\phi) \quad (4.10)$$

$$E_{\phi i} = \frac{A_{ms}}{\ell_1} j^{s+1} \exp(-j k_c \ell_1) E_{\phi c} \sin(m\phi) \quad (4.11)$$

$$H_{\theta i} = \frac{A_{ms}}{\ell_1} j^{s+1} \exp(-j k_c \ell_1) H_{\theta c} \sin(m\phi) \quad (4.12)$$

$$H_{\phi i} = \frac{A_{ms}}{\ell_1} j^{s+1} \exp(-j k_c \ell_1) H_{\phi c} \cos(m\phi) \quad (4.13)$$

where  $\ell_1$  is the path length of the incident ray from the phase centre;  $E_{\theta c}$ ,  $E_{\phi c}$ ,  $H_{\theta c}$  and  $H_{\phi c}$  are the variables given by equations (3.94) - (3.97).

For the above fields, if attention is restricted only to the dominant mode, the factor  $A_{ms} j^{s+1}$  can be dropped. However, to add the contribution of higher order modes, the evaluation of the constant  $A_{ms}$ , using the procedure given in Section 3.3.3, requires a knowledge about the type and the length of the launcher. The analysis presented in the subsequent paragraphs has been restricted only to the dominant mode in the dielectric cone. The main reason for this is to draw some qualitative

conclusions on the general performance of the overall antenna system.

The incident field at the shaped surface undergoes a total internal reflection. The magnitude of the reflection coefficients for the field components, parallel and perpendicular to the plane of incidence is unity. However, the total internal reflection results in different phase changes for the components parallel and perpendicular to the plane of incidence [Born and Wolf, 1964], thus providing a relative phase difference between the two components. The calculation of the phase change on electric and magnetic field components can be simplified by assuming the constant  $k_c$  to be approximately equal to the constant  $k_1$ . With this approximation the incident field components, dropping the constant  $A_{ms} j^{s+1}$ , are given as

$$E_{\theta i} = \frac{1}{\ell_1} \exp(-j k_1 \ell_1) E_{\theta c} \cos(m\phi) \quad (4.14)$$

$$E_{\phi i} = \frac{1}{\ell_1} \exp(-j k_1 \ell_1) E_{\phi c} \sin(m\phi) \quad (4.15)$$

$$H_{\theta i} = - (\epsilon_1 / \mu_1)^{1/2} E_{\phi i} \quad (4.16)$$

$$H_{\phi i} = (\epsilon_1 / \mu_1)^{1/2} E_{\theta i} \quad (4.17)$$

where  $E_{\theta c}$  and  $E_{\phi c}$  are given by equations (3.94) and (3.95), respectively. By making the above approximation, the hybrid modes behave like spherical waves which, for distances far from origin, are plane waves.

As shown in Appendix B,  $E_\theta$  and  $E_\phi$  components of the electric

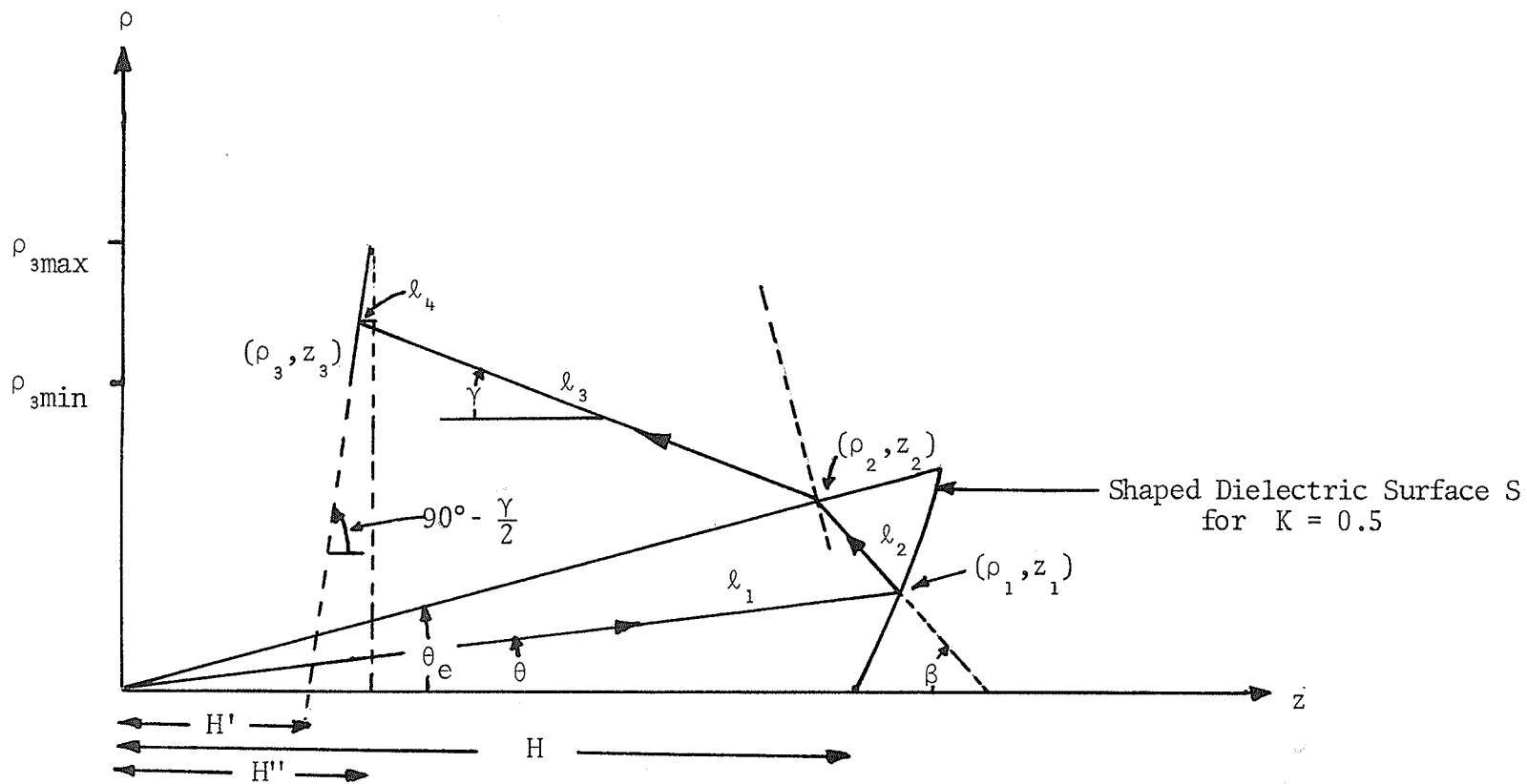


Fig. 4.6 Geometry of an antenna using dielectric cone feed with a shaped reflecting surface

field undergo changes corresponding to the parallel and perpendicular formulae, respectively. Therefore, the reflected field from the shaped surface has the electric field components given by

$$E_{\theta r} = E_{\theta i} \exp(-j \delta_{11}) \quad (4.18)$$

$$E_{\phi r} = E_{\phi i} \exp(-j \delta_{\perp}) \quad (4.19)$$

where from Born and Wolf (1964),

$$\delta_{11} = 2 \tan^{-1} \left[ \frac{\sqrt{(\sin^2 \theta_{nic} - \epsilon_2 / \epsilon_1)}}{(\epsilon_2 / \epsilon_1) \cos \theta_{nic}} \right] \quad (4.20)$$

$$\delta_{\perp} = 2 \tan^{-1} \left[ \frac{\sqrt{(\sin^2 \theta_{nic} - (\epsilon_2 / \epsilon_1))}}{\cos \theta_{nic}} \right] \quad (4.21)$$

with  $\theta_{nic}$  = Angle of the incident ray with normal to the shaped surface =  $(\theta_c + \theta/2.0)$

$\epsilon_1$  and  $\epsilon_2$  = the dielectric constants of the cone medium and surrounding medium respectively.

The reflected ray from the shaped surface, corresponding to  $K = 0.5$ , at the point with coordinates (Fig. 4.6)

$$\rho_1 = H \cos^2 \theta_c \sin \theta \sec^2 (\theta_c + \theta/2) \quad (4.22)$$

and

$$z_1 = H \cos^2 \theta_c \cos \theta \sec^2 (\theta_c + \theta/2) \quad (4.23)$$

is incident on the cone edge at the point with coordinates

$$\rho_2 = 2H \sin\theta_e \operatorname{Cosec}(2\theta_c + \theta_e) \cos^2\theta_c \tan(\theta_c + \theta/2) \quad (4.24)$$

and

$$z_2 = 2H \cos\theta_e \operatorname{Cosec}(2\theta_c + \theta_e) \cos^2\theta_c \tan(\theta_c + \theta/2) \quad (4.25)$$

where

$H =$  cone length at  $\theta = 0^\circ$  ,

$\theta_e =$  cone flare angle,

and  $\theta_c =$  critical angle for the dielectric material of dielectric constant  $\epsilon_1$  surrounded by a medium of dielectric constant  $\epsilon_2$  .

Therefore, the incident field at the cone edge is given as

$$E_{\theta ie} = E_{\theta r} \exp(-j k_1 \ell_2) \quad (4.26)$$

$$E_{\phi ie} = E_{\phi r} \exp(-j k_1 \ell_2) \quad (4.27)$$

where from equations (4.22) - (4.25) ,

$$\ell_2 = H \cos^2\theta_c \operatorname{Sec}^2(\theta_c + \theta/2) \sin(\theta_e - \theta) \operatorname{Cosec}(2\theta_c + \theta_e) \quad (4.28)$$

The transmitted field from the cone edge has the form

$$E_{\theta te} = E_{\theta ie} T_{11} \quad (4.29)$$

$$E_{\phi te} = E_{\phi ie} T_{\perp} \quad (4.30)$$

where from equations (B.45) and (B.46)

$$T_{11} = \frac{2 \sqrt{\epsilon_1} \cos \theta_{nie}}{\sqrt{\epsilon_1} \cos \theta_{nte} + \sqrt{\epsilon_2} \cos \theta_{nie}} \quad (4.31)$$

$$T_{\perp} = \frac{2 \sqrt{\epsilon_1} \cos \theta_{nie}}{\sqrt{\epsilon_1} \cos \theta_{nie} + \sqrt{\epsilon_2} \cos \theta_{nte}} \quad (4.32)$$

with

$$\theta_{nie} = 90^\circ - \theta_e - 2\theta_c \quad (4.33)$$

and

$$\theta_{nte} = \sin^{-1} \left[ \left( \frac{\sqrt{\epsilon_1}}{\sqrt{\epsilon_2}} \right) \sin(\theta_{nie}) \right] \quad (4.34)$$

It should be noted from Eq. (4.33) that all the transmitted rays from the cone edge for different angles of incidence are parallel to each other. The transmitted field from the cone edge is incident on the main conical reflector at the point with coordinates (Fig. 4.6)

$$\rho_3 = C_1 \tan(\theta_c + \theta/2) + C_2 \quad (4.35)$$

and

$$z_3 = \rho_3 \tan(\gamma/2) + H' \quad (4.36)$$

where

$$C_1 = 2H \cos^2 \theta_c \sin(\theta_e + \gamma) \operatorname{cosec}(2\theta_c + \theta_e) \quad (4.37)$$

$$C_2 = -H' \sin \gamma \quad (4.38)$$

$H'$  = distance of the conical reflector from the origin along  
z-axis

and  $\gamma = 90^\circ - \theta_e - \theta_{nte} \quad (4.39)$

Therefore, the incident field at the main conical reflector is given as

$$E_{\theta im} = E_{\theta ie} T_{11} \exp(-j k_2 \ell_3) \quad (4.40)$$

$$E_{\phi im} = E_{\phi ie} T_{\perp} \exp(-j k_2 \ell_3) \quad (4.41)$$

where from equations (4.24), (4.25), (4.35) and (4.36)

$$\begin{aligned} \ell_3 = 2H \cos^2 \theta_c \cos(\theta_e + \gamma/2) \sec(\gamma/2) \operatorname{Cosec}(2\theta_c + \theta_e) \\ \tan(\theta_c + \theta/2) - H' \end{aligned} \quad (4.42)$$

Substituting for  $E_{\theta ie}$  and  $E_{\phi ie}$  in terms of incident field at the shaped surface, the incident fields at the main reflector are written as

$$\begin{aligned} E_{\theta im} = \frac{1}{\ell_1} E_{\theta c} T_{11} \exp[-j(\delta_{11} + k_1 \ell_1 + k_1 \ell_2 + k_2 \ell_3)] \\ \cos(m\phi) \end{aligned} \quad (4.43)$$

$$\begin{aligned} E_{\phi im} = \frac{1}{\ell_1} E_{\phi c} T_{\perp} \exp[-j(\delta_{\perp} + k_1 \ell_1 + k_1 \ell_2 + k_2 \ell_3)] \\ \sin(m\phi) \end{aligned} \quad (4.44)$$

and the fields at the main aperture are given by

$$\begin{aligned} E_{\theta A} = \frac{1}{\ell_1} E_{\theta c} T_{11} \exp[-j(\delta_{11} + k_1 \ell_1 + k_1 \ell_2 + k_2 \ell_3 + k_2 \ell_4)] \\ \cos(m\phi) \end{aligned} \quad (4.45)$$

$$E_{\phi A} = -\frac{1}{\ell_1} E_{\phi C} T_{\perp} \exp[-j(\delta_{\perp} + k_1 \ell_1 + k_1 \ell_2 + k_2 \ell_3 + k_2 \ell_4)] \sin(m\phi) \quad (4.46)$$

where from Fig. 4.6

$$\ell_4 = H'' - H' \cos \gamma - 2H \cos^2 \theta_c \sin(\theta_e + \gamma) \tan(\gamma/2) \operatorname{Cosec}(2\theta_c + \theta_e) \tan(\theta_c + \theta/2) \quad (4.47)$$

with  $H''$  being the distance of the aperture plane from the origin along the  $z$ -axis. It should be noted that in writing equations (4.45) and (4.46) use has been made of the reflection coefficients from the perfectly conducting surface for the parallel and perpendicular components. After some simple trigonometric manipulations, it is found that the path length terms in the exponentials of equations (4.45) and (4.46) are independent of the angle of incidence on the shaped surface, i.e.,

$$\begin{aligned} & \exp[-j(k_1 \ell_1 + k_1 \ell_2 + k_2 \ell_3 + k_2 \ell_4)] \\ &= \exp[-j k_2 (2H \cos^2 \theta_c / \sin \theta_c \\ & \quad + H'' - 2H' \cos^2 \gamma / 2)] \end{aligned} \quad (4.48)$$

Therefore, the aperture of the main reflector has a phase variation which is not equal for the  $E_{\theta}$  and  $E_{\phi}$  components, due to the phase change introduced by the total internal reflection at the shaped dielectric surface.

The normalized E-plane aperture distributions for conical reflectors with modified dielectric cone feeds corresponding to cone flare angles of  $5^\circ$ ,  $10^\circ$  and  $15^\circ$  are shown in Fig. 4.7. The conical reflectors have their corners coincident with the dielectric cone apex and the relative permittivity of the cone material in all cases is 3.0. The corresponding H-plane distributions are shown in Fig. 4.8. It is evident from these figures that the taper level at the cone edge increases with an increase in the cone angle, thus indicating a reduction in spillover loss with an increase in cone flare angle. The other observation which can be made from these figures is that the phase variation for the  $E_\theta$  component is, in general, greater than that for the  $E_\phi$  component.

The effect of changing the dielectric constant of the cone material, for a fixed cone flare angle, is indicated in Figures 4.9 and 4.10 for the E-plane and the H-plane distributions, respectively. An increase in dielectric constant increases the taper level thus reducing the spillover loss.

#### 4.3.2 Theoretical Radiation Patterns of a Conical Reflector With Modified Dielectric Cone Feed

Consider a conical reflector fed by a dielectric cone with a shaped reflecting surface corresponding to  $K = 0.5$ . The transmitted rays from the cone edge of this feed are parallel to each other and make an angle  $\gamma$ , given by Eq. (4.39), with the z-axis. A conical reflector placed in the path of these rays at angle  $90^\circ - \gamma/2$  will result in the reflected rays parallel to the z-axis. The apex of this conical reflector

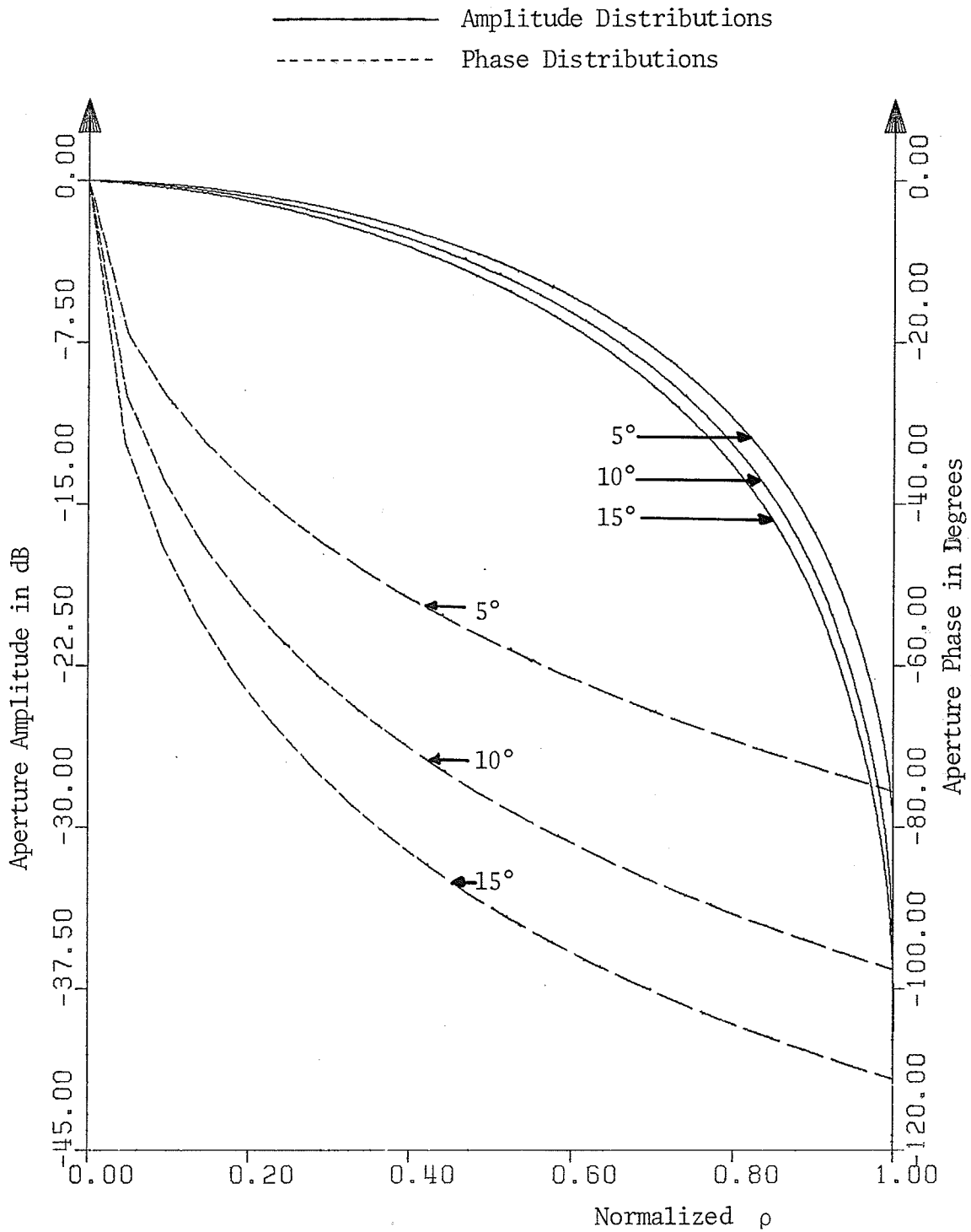


Fig. 4.7 Theoretical E-plane aperture distributions as a function of cone flare angle  $\theta_e$  for conical reflector antennas with modified dielectric cone feed

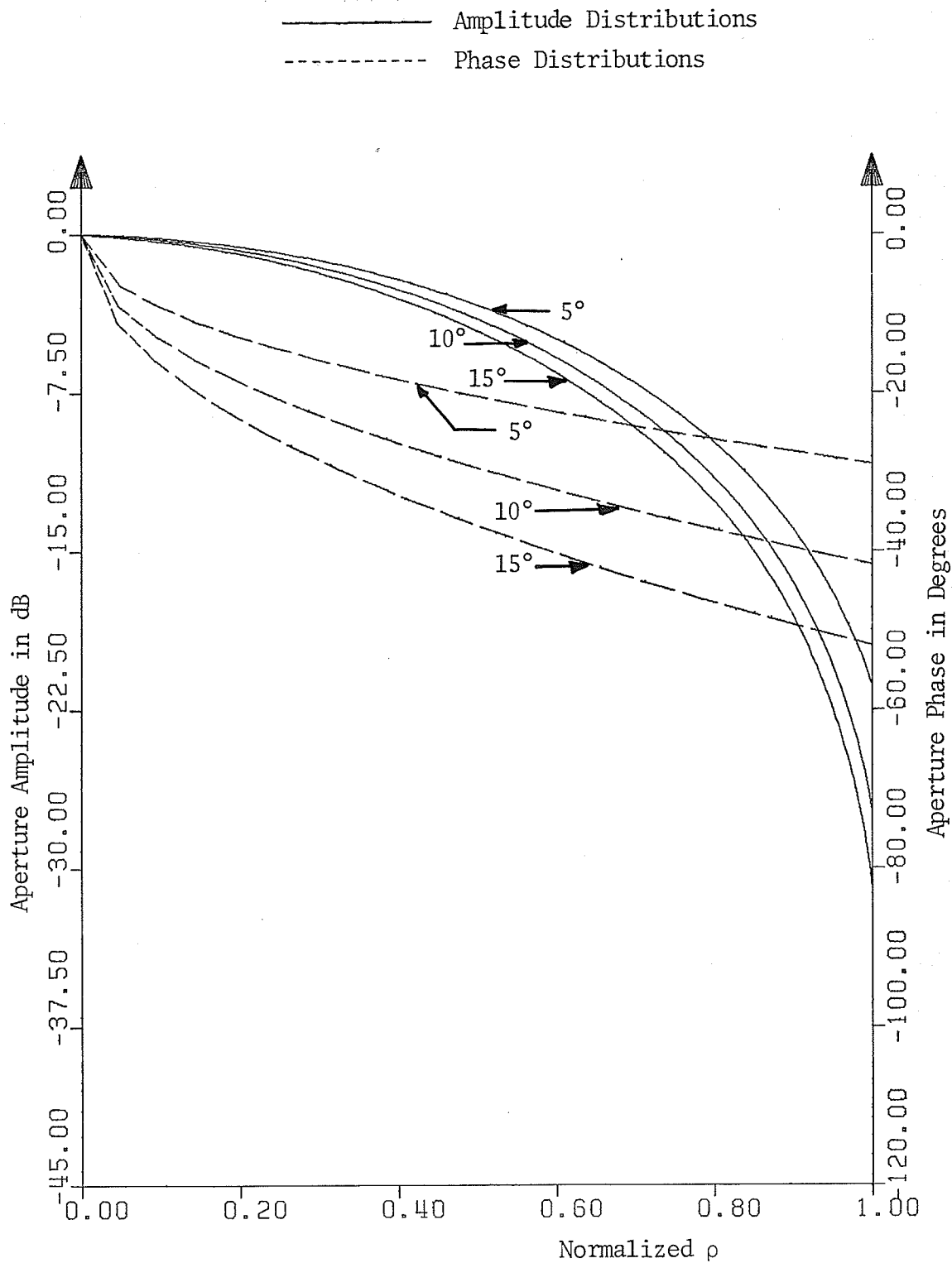


Fig. 4.8 Theoretical H-plane aperture distributions as a function of cone flare angle  $\theta_0$  for conical reflector antennas with a modified dielectric cone feed

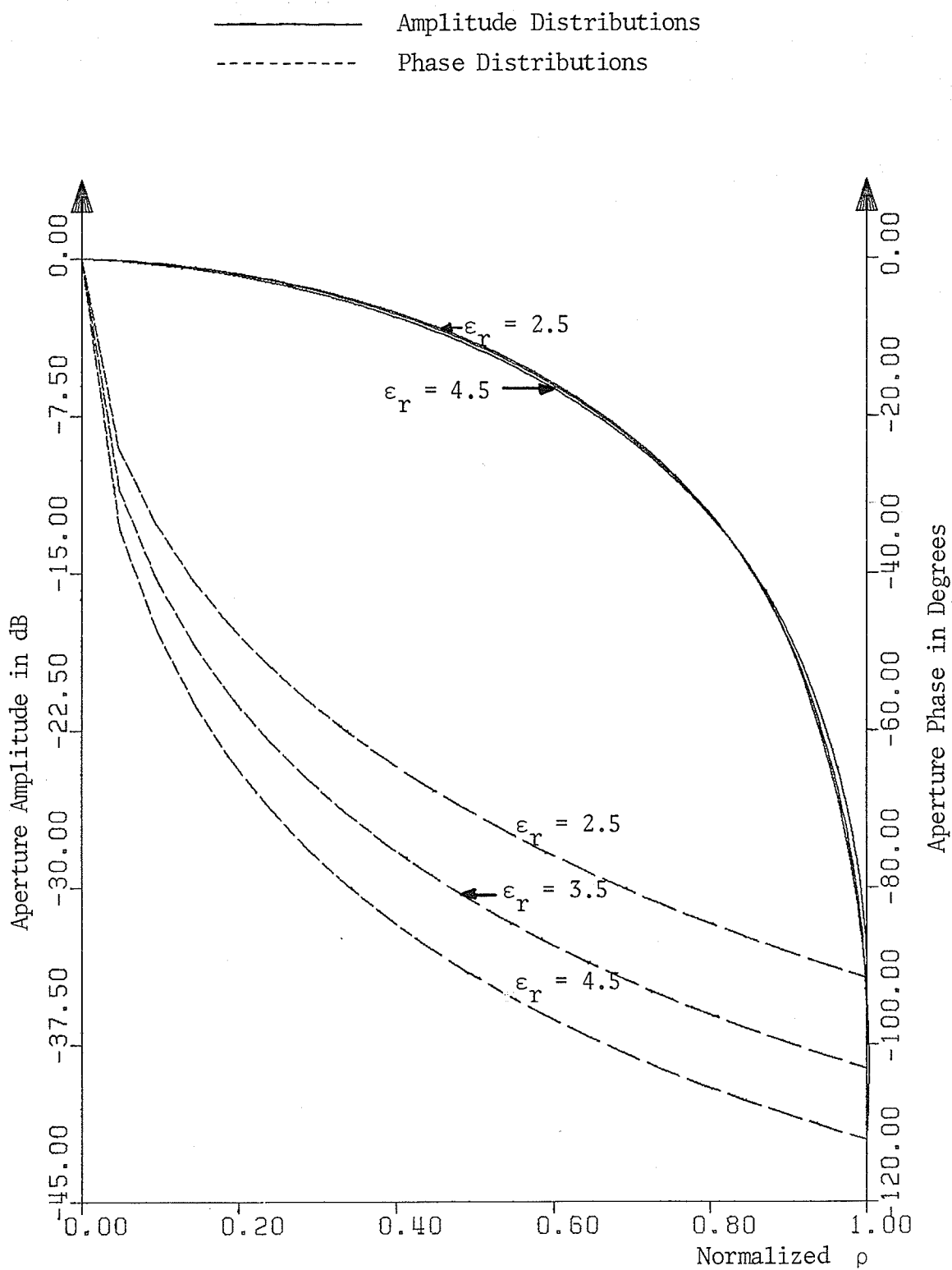


Fig. 4.9 Theoretical E-plane aperture distributions as a function of relative permittivity for conical reflector antennas with modified dielectric cone feed for  $\theta_e = 10^\circ$

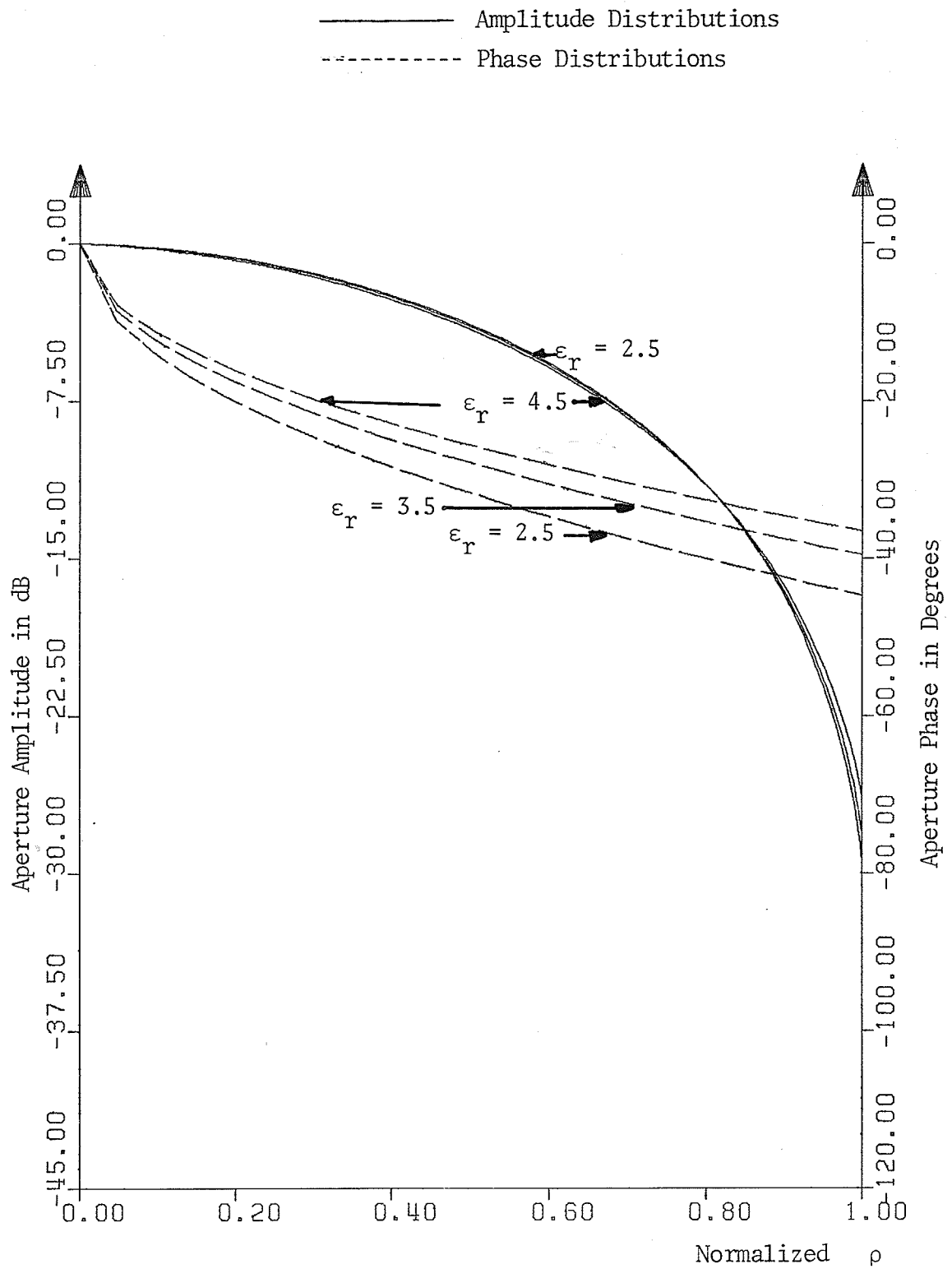


Fig. 4.10 Theoretical H-plane aperture distributions is a function of relative permittivity for conical reflector antennas with modified dielectric cone feed for  $\theta_e = 10^\circ$

for simplicity, will be taken to be coincident with the apex of the dielectric cone. The normal vector to this conical reflector is then given as

$$\bar{n} = -\sin(\gamma/2) \cos\phi \bar{a}_x - \sin(\gamma/2) \sin\phi \bar{a}_y + \cos(\gamma/2) \bar{a}_z \quad (4.49)$$

The incident magnetic field on the conical main reflector in the rectangular coordinates is given as [Spiegel, 1959]

$$\begin{aligned} \bar{H}_{im} = & - [H_{\theta im} \cos\gamma \cos\phi + H_{\phi im} \sin\phi] \bar{a}_x \\ & - [H_{\theta im} \cos\gamma \sin\phi - H_{\phi im} \cos\phi] \bar{a}_y \\ & - H_{\theta im} \sin\gamma \bar{a}_z \end{aligned} \quad (4.50)$$

where

$$H_{\theta im} = -(\epsilon_2/\mu_2)^{1/2} E_{\phi im} \quad (4.51)$$

$$H_{\phi im} = (\epsilon_2/\mu_2)^{1/2} E_{\theta im} \quad (4.52)$$

with  $\epsilon_2, \mu_2$  being the material parameters of the surrounding medium; and  $E_{\theta im}, E_{\phi im}$  being the incident field components given by equations (4.43) and (4.44), respectively. Using equations (4.49) and (4.50), the induced current on the conical reflector is given by

$$\begin{aligned} \bar{J}_s = & 2[H_{\theta im} \sin\phi - H_{\phi im} \cos\phi] \cos(\gamma/2) \bar{a}_x \\ & -2[H_{\theta im} \cos\phi + H_{\phi im} \sin\phi] \cos(\gamma/2) \bar{a}_y \\ & -2 H_{\phi im} \sin(\gamma/2) \bar{a}_z \end{aligned} \quad (4.53)$$

which when substituted in the vector diffraction integral [Rusch and Potter, 1970]

$$\begin{aligned} \bar{E}_S(\theta', \phi') = & \frac{-j\omega\mu}{4\pi r'} e^{-jk_2 r'} \int_S [\bar{J}_S - (\bar{J}_S \cdot \bar{a}_{r'}) \bar{a}_{r'}] \\ & \times \exp(j k_2 \bar{\rho} \cdot \bar{a}_{r'}) dS \end{aligned} \quad (4.54)$$

gives

$$\begin{aligned} E_{S\theta'}(\theta', \phi') = & -\frac{j\omega\mu}{2\pi r'} e^{-jk_2 r'} \int_{\rho_{3\min}}^{\rho_{3\max}} \int_0^{2\pi} [H_{\theta im} \cos\theta' \sin(\phi-\phi') \\ & - H_{\phi im} \cos\theta' \cos(\phi-\phi') - H_{\phi im} \sin\theta' \tan(\gamma/2)] \\ & \times \exp[j\alpha + j\psi \cos(\phi-\phi')] \rho_3 d\rho_3 d\phi \end{aligned} \quad (4.55)$$

$$\begin{aligned} E_{S\phi'}(\theta', \phi') = & -\frac{j\omega\mu}{2\pi r'} e^{-jk_2 r'} \int_{\rho_{3\min}}^{\rho_{3\max}} \int_0^{2\pi} [-H_{\theta im} \cos(\phi-\phi') \\ & - H_{\phi im} \sin(\phi-\phi')] \exp[j\alpha + j\psi \cos(\phi-\phi')] \\ & \rho_3 d\rho_3 d\phi \end{aligned} \quad (4.56)$$

where  $\alpha = k_2 r \cos\theta \cos\theta' = k_2 z_3 \cos\theta'$

$\psi = k_2 r \sin\theta \sin\theta' = k_2 \rho_3 \sin\theta'$

$(r', \theta', \phi')$  = spherical coordinates for the observation point, and  
 $(\rho_3, \phi, z_3)$  = cylindrical coordinates for the point on the conical reflector. The numerical evaluation of the above integrals can be simplified by substituting the closed form expressions for the integration with

respect to  $\phi$  variable. Performing the integration with respect to  $\phi$  after substituting for  $H_{\theta_{im}}$  and  $H_{\phi_{im}}$  from equations (4.51), (4.52) (4.43) and (4.44) results in the radiation field components given as

$$E_{S\theta'}(\theta', \phi') = C \int_0^{\theta} e^{-j\delta} [-E_{\phi C} T_{\perp} \exp(-j\delta_{\perp}) \cos\theta' \delta - E_{\theta C} T_{11} \exp(-j\delta_{11}) \cos\theta' \xi - 2j E_{\theta C} T_{11} \exp(-j\delta_{11}) \sin\theta' \tan(\gamma/2) J_m(\psi)] \exp[j(\alpha - k_{11} \ell_1 - k_{12} \ell_2 - k_{23} \ell_3)] \tan(\theta_c + \theta/2) d\theta \quad (4.57)$$

$$E_{S\phi'}(\theta', \phi') = C \int_0^{\theta} e^{-j\delta} [+E_{\phi C} T_{\perp} \exp(-j\delta_{\perp}) \xi + E_{\theta C} T_{11} \exp(-j\delta_{11}) \delta] \exp[j(\alpha - k_{11} \ell_1 - k_{12} \ell_2 - k_{23} \ell_3)] \tan(\theta_c + \theta/2) d\theta \quad (4.58)$$

where  $C = -j^m k_2 H \cos^2 \theta_c \sin^2(\theta_e + \gamma) \operatorname{Cosec}^2(2\theta_c + \theta_e) \exp(-j k_2 r')/r'$

$$\delta = J_{m-1}(\psi) + J_{m+1}(\psi)$$

and  $\xi = J_{m-1}(\psi) - J_{m+1}(\psi)$  .

It should be noted that in writing the above equations, the parameters  $\rho_3$  and  $\ell_1$  have been substituted from equations (4.35), (4.22) and (4.23).

The above equations are used to calculate the radiation patterns for the conical reflectors with modified dielectric cone feed. The radiation patterns shown in Figures 4.11 - 4.14 correspond to the cases whose

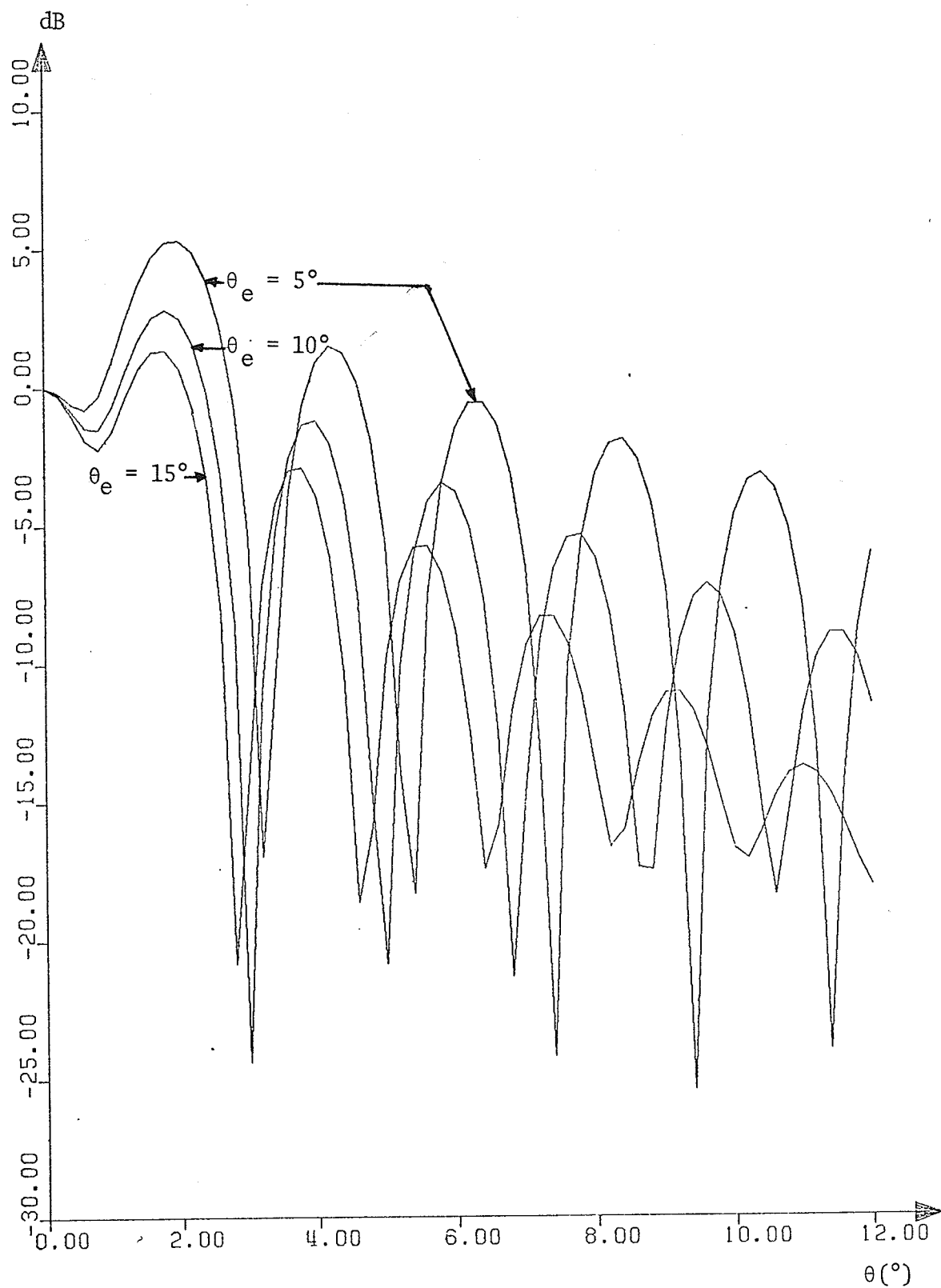


Fig. 4.11 E-plane theoretical radiation patterns of conical reflector antennas with modified dielectric cone feed as a function of cone flare angle  $\theta_e$ .

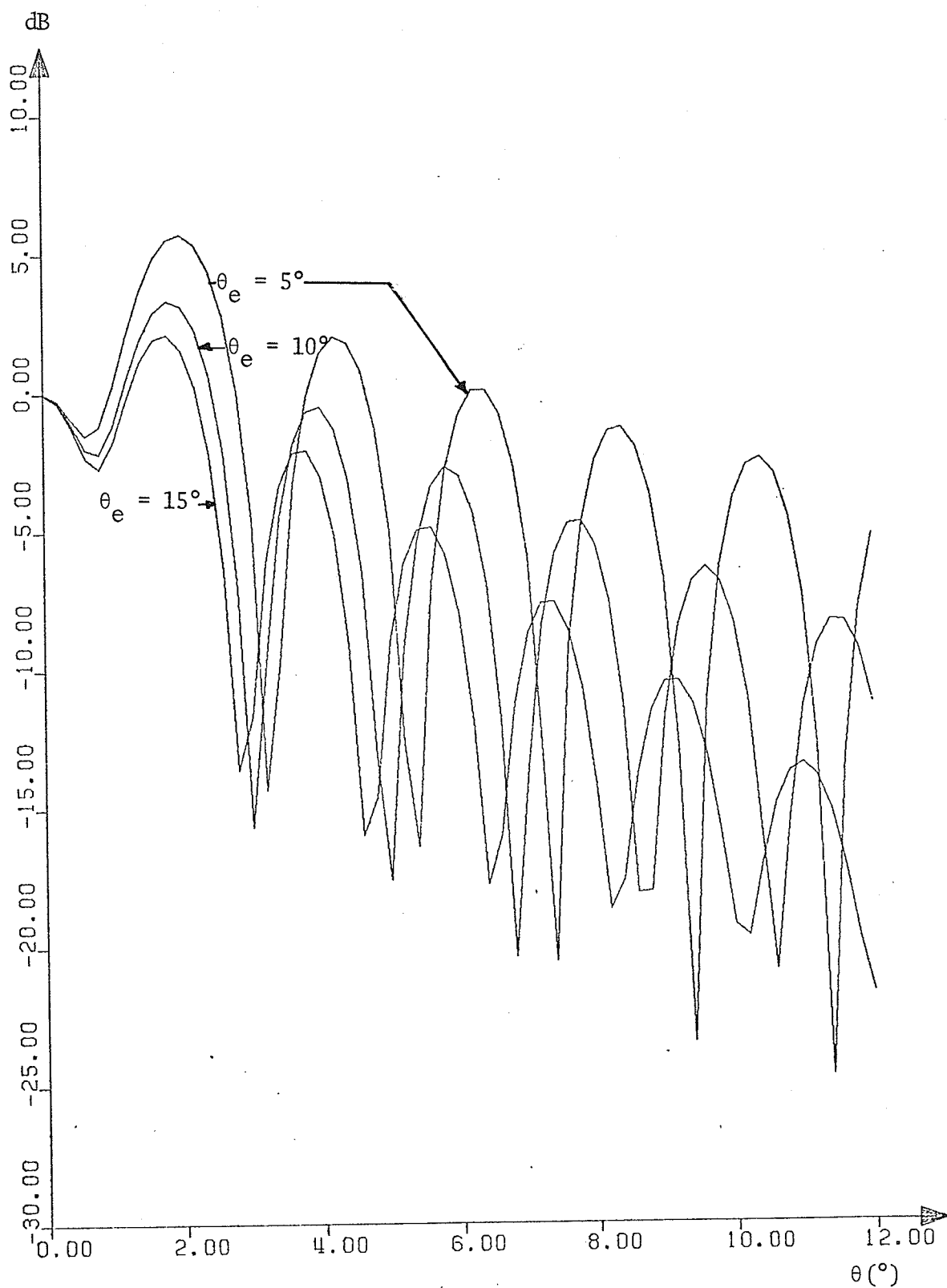


Fig. 4.12 H-plane theoretical radiation patterns of conical reflector antennas with a modified dielectric cone feed as a function of cone flare angle  $\theta_e$

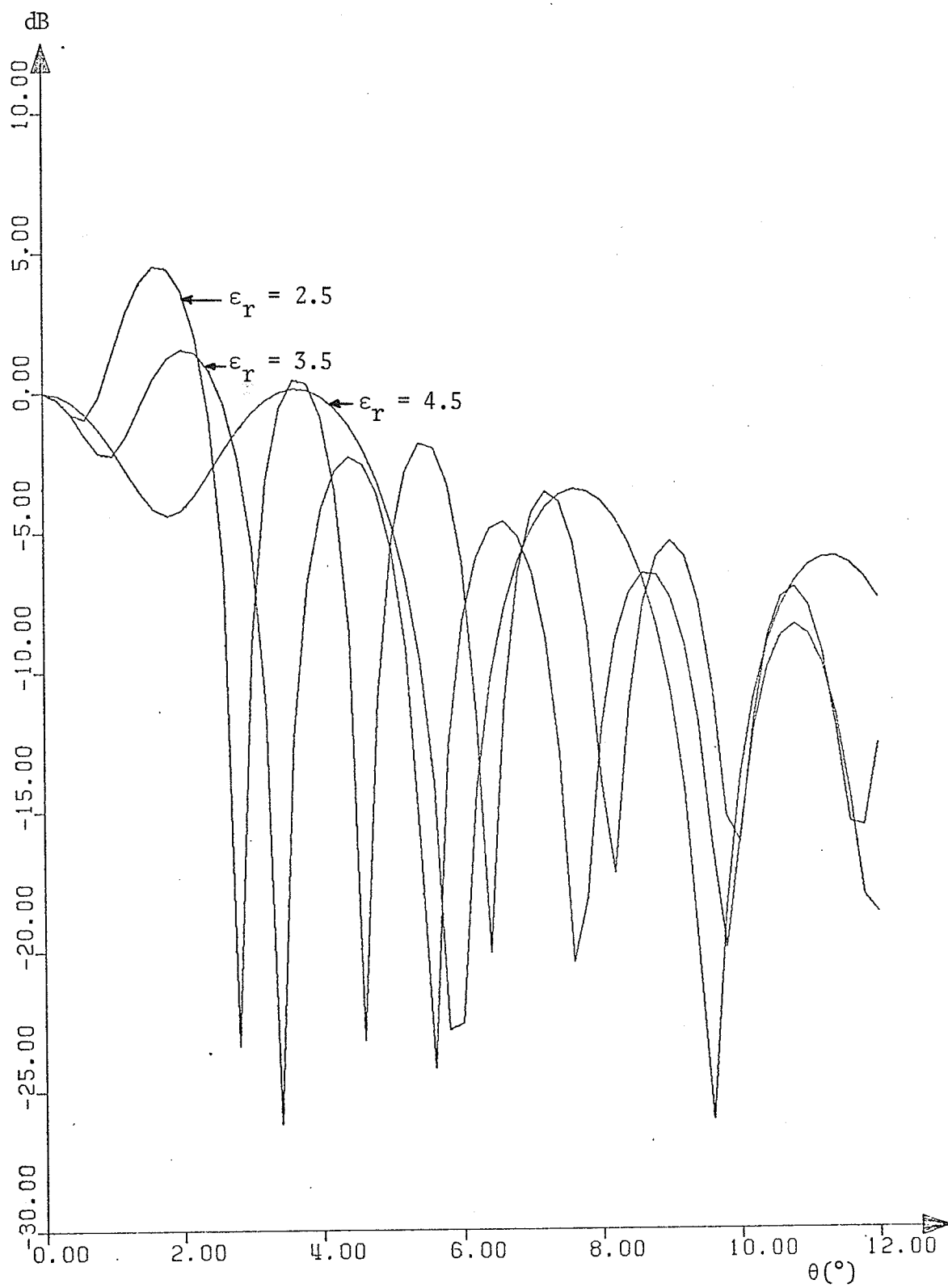


Fig. 4.13 E-plane theoretical radiation patterns for conical reflector antennas with modified dielectric cone feed as a function of relative permittivity of the cone material

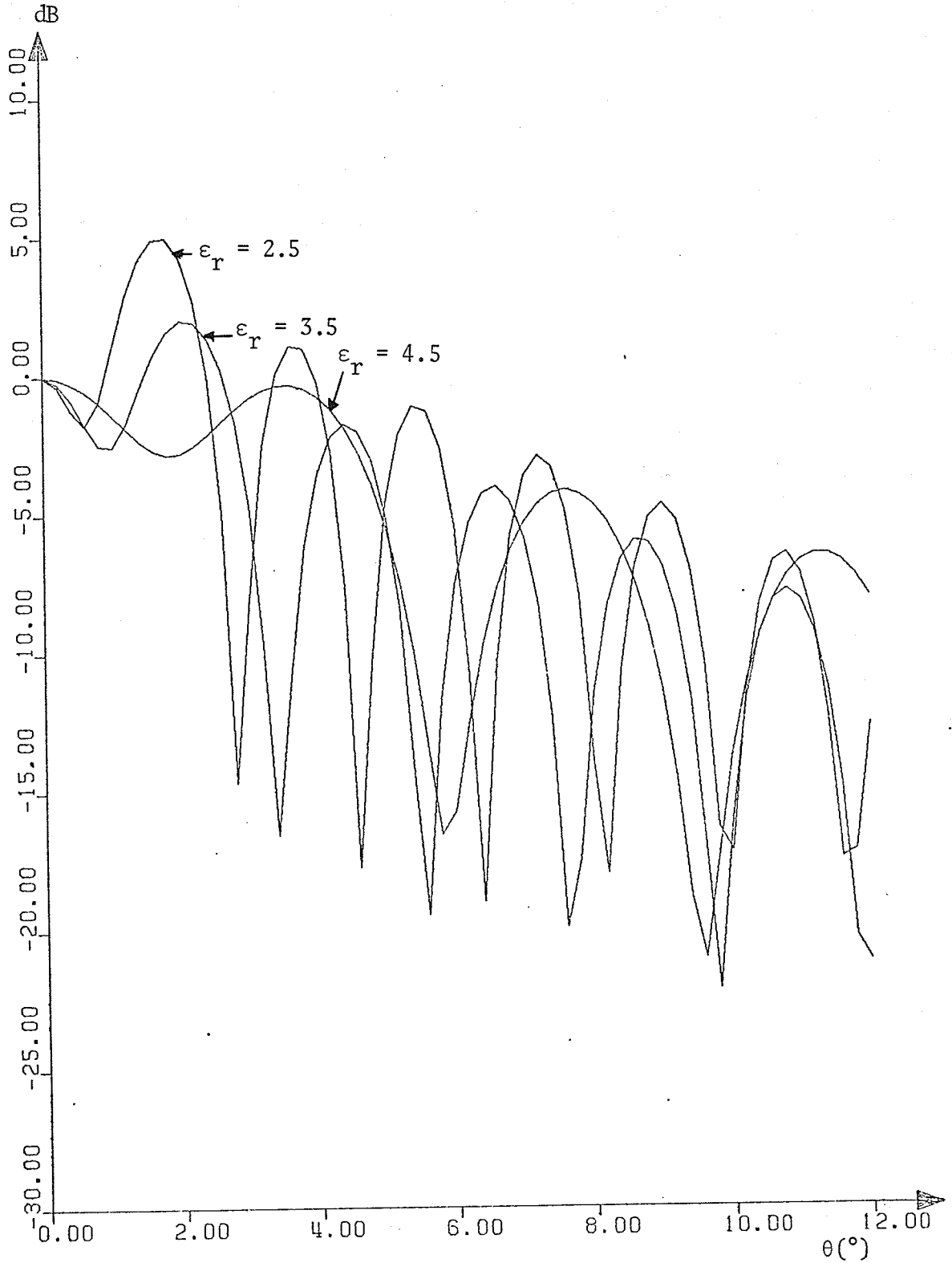


Fig. 4.14 H-plane theoretical radiation patterns for conical reflector antennas with modified dielectric cone feed as a function of relative permittivity of the cone material

aperture distributions are shown in Figures 4.7 - 4.10. The radiation patterns have been checked by using aperture field method and the difference in the values was found to be not very significant.

These radiation patterns, in general, as shown in Figures 4.11 - 4.14 do not have the maximum for  $\theta = 0$ . This has been found to be resulting from the phase differences in the two components of the magnetic field. This behaviour disappears i.e., the maximum shifts to the main axis, by making any one of the magnetic field components go to zero. This may possibly be achieved by exciting a number of modes in the dielectric cone. However, it should be noted that this requires a further investigation about the behaviour of different modes and the ways to control these modes to make one of the components equal to zero.

As shown in Figures 4.11 - 4.14, the first maximum may be reduced by either increasing the cone angle or increasing the dielectric constant of the cone material. However, it should be noted that increasing the dielectric constant of the cone material results in a decrease of the dominant mode excitation efficiency and an increase in the loss at the cone edge due to reflection. Further details for this loss due to reflection are given in Chapter V.

One common feature in all the radiation patterns is a higher level of the second and third side lobes. This seems to be due to the phase errors in the aperture plane and a higher value of the ratio  $\rho_{3\min}/\rho_{3\max}$ . Based on the uniform amplitude and phase distribution in a circular aperture, it is shown by Silver (1949) that an increase in the ratio  $\rho_{3\min}/\rho_{3\max}$  results in higher side lobe levels.

#### 4.4 SUMMARY AND CONCLUSIONS

The design of the shaped reflecting surface of the dielectric cone has been obtained by assuming the angle of the incident ray with the surface normal to be a linear function of the incident angle. The reason for selecting the constant part of the normal angle equal to the critical angle is to have a total internal reflection at the shaped surface, so that the modified dielectric cone acts as a feed to the reflector antenna. Among the different values of the slope, for the shaped surface, two values were found to be of particular interest. The slope of unity gives a conical shaped surface and a slope of 0.5 gives all the internally reflected rays parallel to each other.

The analysis of the shaped surface corresponding to a slope of 0.5 and conical main reflector has been presented in some detail. Some of the conclusions drawn from this investigation are as follows:

- 1) The total internal reflection at the shaped surface results in nonlinear differential phase errors between orthogonal E components of the internally reflected fields, thus providing a relative phase difference between the two orthogonal components in the aperture plane.
- 2) Although the path length of the incident rays at different angles of incidence is constant up to the aperture of the conical reflector, the phase differences introduced due to total internal reflection result in phase errors of the aperture fields.
- 3) The radiation patterns of the conical reflector with a modified dielectric cone feed, in general, do not have the maximum at

$\theta = 0$ . The level of this first maximum may be decreased by increasing the cone angle, increasing the dielectric constant of the cone material, or making one of the components of the incident field go to zero. In general, for excellent radiation characteristics an alternative launcher may be designed, so that it compensates for the resulting phase variations.

4) The radiation patterns of the conical reflector indicate a higher level for the second and third side lobes. The higher levels of the side lobes may be due to the phase errors in the aperture plane and a higher value of the ratio  $\rho_{3\min}/\rho_{3\max}$  (Fig. 4.6).

5) A large value of the ratio  $\rho_{3\min}/\rho_{3\max}$  results in a larger portion of the conical reflector not being used. Making the shaped surface diameter equal to the minimum diameter of the main reflector results in a wide beam antenna. The possibility of putting many conical reflectors to decrease this ratio gives path length errors in the aperture plane and leads to the complexity of feed shaping.

From the above discussion it is clear that with assumed dielectric cone feeds the resulting phase errors and higher side lobes make the antenna system an impractical solution. It seems that a useful antenna system with acceptable aperture phase distribution can only be obtained by alternative launcher systems with a matched phase and amplitude distributions to compensate for the resulting phase errors. No attempt is made in this thesis to study the design of such feed systems. Instead attention is changed from assuming a specific relation for the angle of the incident ray with the shaped surface normal to the possibility of designing for any arbitrary amplitude and phase distributions. The details of this design are presented in the next chapter.

CHAPTER V

DESIGN OF DIELECTRIC CONE FEED ANTENNAS

FOR ARBITRARY APERTURE DISTRIBUTION